Optical Spray Patternation of Gasoline Fuel Injectors

by

Ryan M. Rudnitzki

A thesis submitted in partial fulfillment

of the requirements for a degree of

Master of Science

(Mechanical Engineering)

at the

University of Wisconsin – Madison

2005

Abstract

Planar Mie scattering images were acquired for 21 injectors to investigate the feasibility of a predictive method of injector performance in an engine. A testing apparatus was constructed, which allowed optical access for spray illumination and visualization at pressures up to 650 kPa. The injectors were tested by taking images of a thin cross section of a fuel spray, illuminated with counter-propagating in-plane laser sheets. Data were collected at atmospheric pressure, using capture delay times of 2.5 and 2.7 ms, and at 377 kPa absolute, at 3.1, 3.6, and 4.1 ms. Tests were also run to assess the impact of secondary scattering in the spray images. The results of these tests revealed some signal attenuation and blurring of the images, as well as laser sheet attenuation.

Visual analysis of the injector images was only capable of identifying the known good injectors (R1-R6) and the known worst injector (#6). Statistical analysis of spray using the Insight 3G pattern factor tool produced better results. Identification of the good and bad injectors was possible using a capture delay time of 4.1 ms, a vessel pressure of 377 kPa, and a fuel-air delay of 0.952 ms. Similar results were found using the same parameters, but with a capture delay time of 3.6 ms. Of the blind injectors, #2, #8, and #13 were thought to be good, and #4, #10, and #14 were considered. The pattern factor results were sensitive to changes in input parameters. Because of this sensitivity, the ranking of the injectors with APFs near the data set mean could not be determined.

Acknowledgements

Professor Jaal Ghandhi deserves most of the credit for this project going anywhere. His experimental skills, lab saavy, and wealth of engineering knowledge have been invaluable in my growth as an engineering student. Thanks for all the time and effort that went into this project. I would also like to thank Professors Klein and Nellis, who encouraged me to go to graduate school, and lied about my intelligence to get me a research position.

I am also indebted to Ralph Braun for all of the help and guidance he provided, as I learned the ropes of machining and fabrication. Thanks to Josh Leach for bailing me out of some fun computer issues more than a few times. Jon Erb and the electrical staff should be recognized for wiring the circuitry for my laser, and for fixing the thermostat in our office so I could spend my summer hours in the office at a comfortable temperature. Suzie Strzelec and Deanna Duerst also deserve gratitude for helping with the credit card bills.

When I started in the Engine Research Center almost two years ago, I had very little practical engineering experience. Much of my improvement can be attributed to my colleagues, who provided an abundance of assistance and knowledge. Randy Herold, Brian Albert, Andy Bright, and Bob Iverson were all especially helpful in all aspects of my research. Lonny Peet and Chris Behrendt should also be thanked for building my test apparatus. Much love goes out to my colleagues and friends Mark Schrewe, Sean Younger, Nate Haugle, Rinaldo Augusta, Paul Loeper, Matt Borden, Jon Filipa, Adam Myers, Victor Salazar, Angelo Chialva, Brandon Lachner, Tim Pfeifer, and Ben Petersen for the help and companionship. Thanks to past ERC students, Dr. Joseph Shakal and Dr. Tyson Strand of TSI for all of the Insight 3G support and troubleshooting assistance.

My parents deserve thanks for providing guidance and support through the emotional hurdles, as well as Theresa for keeping me well-grounded with her nightmarish work stories and providing love and laughs whenever they were needed.

Last but not least, thanks much to Chuck Eichinger and Mercury Marine, for funding my project through the Brunswick Fellowship. Thanks for finding a home for me.

Table of Contents

ABSTRACT ..... **I**

ACKNOWLEDGEMENTS ..... **II**

TABLE OF CONTENTS ..... **IV**

LIST OF FIGURES ..... **VI**

LIST OF TABLES ..... **VIII**

1.0. INTRODUCTION **1**

2.0. BACKGROUND **4**

2.1. PATTERNATION METHODS 4
2.1.1. Phase Doppler Anemometry *4*
2.1.2. Mechanical Patternators *4*
2.1.3. Laser Sheet Dropsizing *5*
2.2. MIE SCATTERING 7
2.2.1. Mie Scattering Theory *7*
2.2.2. Mie-scattering Setup *7*
2.3. MULTIPLE SCATTERING ISSUES 9
2.3.1. Laser extinction *9*
2.3.2. Signal attenuation and Out of Plane Illumination *9*
2.4. OTHER MIE-SCATTERING SHORTCOMINGS 12
2.5. VIRTUES OF MIE-SCATTERING 14

3.0. EXPERIMENTAL SETUP **15**

3.1. FUEL SYSTEM 15
3.1.1. Air-Assist Injector *15*
3.1.2. Fuel Pressurization System *16*
3.1.3. Fuel Control System *16*
3.2. FUEL INJECTOR TEST VESSEL 18
3.2.1. Optical Components *19*
3.2.2. Air Circulation System *20*
3.3. OPTICAL SYSTEM 25
3.3.1. Laser Source *25*
3.3.2. Optical Setup *25*
3.3.3. Camera *27*
3.3.4. Component Triggering *28*
3.3.5. Image Processing *28*

4.0. CALIBRATION OF TESTING CONDITIONS **29**

4.1. AIR FLOW CALIBRATION 29
4.1.1. Porous Metal Disc Selection *29*
4.1.2. Flow Measurements *33*
4.1.3. Variable Flow *35*
4.2. SECONDARY SCATTERING EFFECTS 37
4.2.1 Laser Sheet Extinction *37*
4.2.2. Out-of-Plane Illumination *39*
4.2.3. Blur Measurements *40*
4.3. TEST CONDITION SELECTION 42

4.3.1. Idle Data *42*
4.3.2. Capture Delay Testing. *44*
4.3.3. Signal Attenuation Test *45*
4.3.4. Flat Field Correction *48*
4.3.5. Strobe Profile Test *49*

5.0. RESULTS **51**

5.1. OVERVIEW OF TESTING AND IMAGE PROCESSING 51
5.1.1. Testing Procedure *51*
5.1.2. Image Capture Technique *51*
5.1.3 Image Processing Method *52*
5.2. VISUAL ANALYSIS OF INJECTOR DATA 55
5.2.1. Comparison of an Injector Subset *55*
5.2.2. Comparison of Reference Injectors *57*
5.2.3. Shot-to-Shot Variability *59*
5.3. STATISTICAL ANALYSIS 62
5.3.1. Pattern Factor Results *62*
5.3.2. Pattern Factor Analysis Issues *66*
5.4. FUEL AIR DELAY SETTINGS 70

6.0. CONCLUSIONS AND RECOMMENDATIONS **77**

6.1. CONCLUSIONS *77*
6.2. RECOMMENDATIONS 79

REFERENCES **81**

APPENDIX A - LIST OF EQUIPMENT **83**

APPENDIX B - ENGINEERING DRAWINGS OF VESSEL COMPONENTS **84**

APPENDIX C - CAMERA SETTING OPTIMIZATION **89**

APPENDIX D - FUEL RAIL PRESSURE DATA **90**

APPENDIX E - IMAGE PROCESSING PROCEDURE **94**

APPENDIX F - AVERAGED PICTURES OF INJ **97**

APPENDIX G - RESULTS OF MEAN PATTERN FACTOR ANALYSIS **99**

APPENDIX H - DATA COMPILED USING 10 RINGS (NOT 12 WEDGES) **100**

List of Figures

FIGURE 2.1. THE RELATIONSHIP BETWEEN FLUORESCENT CONCENTRATION AND LIF SIGNAL RESPONSE. AT N = 3, LIF SIGNALS ARE ASSUMED TO BE PROPORTIONAL TO DROPLET VOLUME. REPRINTED FROM [4]. 6
FIGURE 2.2. ACTUAL MIE SCATTERING SIGNAL COMPARED TO A THEORETICAL SIGNAL BASED ON DROPLET VOLUME. REPRINTED FROM [3]. 12
FIGURE 2.3. MEAN LIF AND MIE SCATTERED IMAGES OF A FUEL INJECTOR SPRAY. REPRINTED FROM [4]. 14
FIGURE 3.1. PRODUCTION OPTIMAX FUEL RAIL. REPRINTED FROM [14]. 17
FIGURE 3.2. PRODUCTION OPTIMAX FUEL PUMP. REPRINTED FROM [14]. 17
FIGURE 3.3. AERIAL VIEW OF TEST VESSEL. 18
FIGURE 3.4. VIEW OF CAMERA OPTICAL ACCESS WINDOW. 20
FIGURE 3.5. THE TWO POROUS METAL DISCS, COAXIALLY ALIGNED IN SERIES ON THE INJECTOR HOUSING. 21
FIGURE 3.6. BACKSIDE OF "CROSS HAIR" HOUSING. THIS HOUSING MATES WITH THE INJECTOR HOLDER IN FIGURE 3.5 TO ALIGN AND SECURE THE INJECTOR AND POROUS METAL. 22
FIGURE 3.7. A VIEW FROM INSIDE THE VESSEL OF THE INJECTOR AND POROUS METAL HOLDER ASSEMBLED. 22
FIGURE 3.8. OPTICAL SETUP. 26
FIGURE 4.1. MANUFACTURER SPECIFIED AIR FLOW CHARACTERISTICS OF MOTT POROUS METAL SHEETS. REPRINTED FROM [17]. 30
FIGURE 4.2. SIMPLE POROUS METAL FLOW VERIFICATION TEST SETUP. REPRINTED FROM [18]. 31
FIGURE 4.3. DIAGRAM OF POROUS METAL ARRANGEMENT IN TEST VESSEL. 32
FIGURE 4.4. SPRAY IMAGES WITH VARYING VESSEL AIR FLOWS. PRESSURES ARE MEASURED AT THE INLET OF THE VESSEL. PIXEL RANGES ARE GIVEN IN PARENTHESIS FROM THE MAXIM MEDIUM AUTOSCALE SETTING. ALL PRESSURES ARE ATMOSPHERIC. 35
FIGURE 4.5. RESULTS OF LASER SHEET EXTINCTION TEST. FUELING RATE IS SET AT 5.2 MG/CYCLE. 38
FIGURE 4.6. RESULTS OF LASER SHEET EXTINCTION TEST. FUELING RATE IS SET AT 15.6 MG/CYCLE. 38
FIGURE 4.7. OVERHEAD VIEW OF IDEAL LASER SHEET. 39
FIGURE 4.8. OVERHEAD VIEW OF LASER SHEET SCATTERED BY FUEL SPRAY 39
FIGURE 4.9. A COMPARISON OF LASER SHEET THICKNESS PROFILE PASSING THROUGH A CUVETTE AND A FUEL SPRAY. THE DIFFERENCE TRACE SHOWS THE AMOUNT OF SCATTERING IN THE FUEL SPRAY. 40
FIGURE 4.10. LASER SHEET AND SPRAY IMAGES WITH THE BOTTOM HALF OF THE LASER SHEET BLOCKED, SHOWING THE AMOUNT OF SCATTERING THAT OCCURRED IN THE IMAGING PLANE. THE DIFFERENCE BETWEEN THE SHEET PROFILE AND THE SPRAY PROFILES ARE SHOWN IN THE FAR RIGHT COLUMN. 41
FIGURE 4.11. UNPRESSURIZED SPRAY IMAGES OF REFERENCE INJECTOR #5 AT DIFFERENT CAPTURE DELAY TIMES. 44
FIGURE 4.12. PRESSURIZED SPRAY IMAGES OF REFERENCE INJECTOR #5 AT DIFFERENT CAPTURE DELAY TIMES. 45
FIGURE 4.13. AVERAGED IMAGE OF ATTENUATION TEST AT A 3.1 MS DELAY. NAIL LOCATION IS IN THE CENTER OF THE BLACK BOX. 47
FIGURE 4.14. LASER SHEET PROFILE, CAPTURED BY PASSING THE SHEET THROUGH A DYE-FILLED CUVETTE. 48
FIGURE 4.15. A DEMONSTRATION OF THE NEGATIVE EFFECTS OF FLAT FIELD CORRECTION. 49
FIGURE 4.16. STROBE ILLUMINATED SPRAY PROFILES AT DIFFERENT CAMERA DELAY TIMES. 50
FIGURE 5.1. VISUAL REPRESENTATION OF INSIGHT PATTERN FACTOR ANALYSIS TOOL. 53
FIGURE 5.2. AVERAGED IMAGE COMPARISON OF A REPRESENTATIVE SET OF FUEL INJECTORS. 56
FIGURE 5.3. INNER STRUCTURE OF AIR-ASSISTED INJECTOR. TWO OF THE FOUR HOLES ARE VISIBLE. 57
FIGURE 5.4. COMPARISON OF THE AVERAGED IMAGES OF THE 6 REFERENCE INJECTORS. 58
FIGURE 5.5. SHOT-TO-SHOT VARIABILITY OF INJECTOR R5 AT 4.1 MS CAPTURE DELAY. 60
FIGURE 5.6. SHOT-TO-SHOT VARIABILITY OF INJECTOR #1 AT 4.1 MS CAPTURE DELAY. 60
FIGURE 5.7. SHOT-TO-SHOT VARIABILITY OF INJECTOR #6 AT 4.1 MS CAPTURE DELAY. 60
FIGURE 5.8. IMAGES OF THE STANDARD DEVIATION OF EACH PIXEL FOR 10 INJECTOR RUNS. THE STANDARD DEVIATION WAS CALCULATED USING 100 BACKGROUND-SUBTRACTED, CENTERED IMAGES TAKEN AT A CAPTURE DELAY TIME OF 4.1 MS AND A PRESSURE OF 377 KPA ABSOLUTE. 61
FIGURE 5.9. PATTERN FACTOR RESULTS AT THE FIVE DIFFERENT CAPTURE DELAY TIMES AND TWO DIFFERENT PRESSURES: A) 4.1 MS, 377 KPA; B) 3.6 MS, 377 KPA; C) 3.1 MS, 377 KPA; D) 2.7 MS, 101.4 KPA; E) 2.5 MS, 101.4 KPA. ALL PRESSURES ARE ABSOLUTE. 12 WEDGES, 1500 BT 64
FIGURE 5.10. SPARK PLUG ANGLES IN A) ENGINE AND B) IMAGES. 65

FIGURE 5.11. A COMPARISON OF APF VALUES WITH DIFFERENT FAD. Y AXIS FAD = 4 MS. X AXIS FAD = 0.952 MS. DATA WERE COLLECTED AT 4.1 MS AND 377 KPA ABSOLUTE PRESSURE.....71
FIGURE 5.12. IMPACT OF FAD ON SPRAY PHASING. IMAGES OF INJECTOR R5 AT DIFFERENT CAPTURE DELAY TIMES AT ATMOSPHERIC PRESSURE WITH FAD OF 0.952 MS AND 4 MS. 73
FIGURE 5.13. IMPACT OF FAD ON SPRAY PHASING. IMAGES OF INJECTOR R5 AT DIFFERENT CAPTURE DELAY TIMES AT 377 KPA ABSOLUTE WITH FAD OF 0.952 MS AND 4 MS. 74
FIGURE 5.14. COMPARISON OF A GOOD INJECTOR (R5) TO A BAD INJECTOR (#1) WITH A FAD OF 4 MS AND VARYING CAPTURE DELAY TIMES AT ATMOSPHERIC PRESSURE. 75
FIGURE 5.15. COMPARISON OF A GOOD INJECTOR (R5) TO A BAD INJECTOR (#1) WITH A FAD OF 4 MS AND VARYING CAPTURE DELAY TIMES AT 377 KPA ABSOLUTE PRESSURE. 76

List of Tables

TABLE 3.1. CAMERA SETTINGS. 28
TABLE 4.1. RESULTS OF SIMPLE POROUS METAL FLOW VERIFICATION TEST. 31
TABLE 4.2. FLOW DATA FROM POROUS METAL ARRANGEMENT IN TEST VESSEL. 33
TABLE 4.3. RESULTS OF APPARATUS FLOW MEASUREMENTS. 34
TABLE 4.4. INJECTOR PARAMETERS AT IDLE. 42
TABLE 4.5. EXPERIMENTAL INJECTOR PARAMETERS. 43
TABLE 4.6. RESULTS OF SIGNAL ATTENUATION TEST. 47
TABLE 5.1. THE EFFECT OF PARAMETER CHANGE ON (APF) VALUES. THE PARAMETERS CHANGED WERE THE METHOD FOR FINDING THE APF, THE BACKGROUND THRESHOLD SETTINGS, AND THE NUMBER OF WEDGES USED. DATA WERE COLLECTED AT 4.1 MS CAPTURE DELAY AND 377 KPA ABSOLUTE PRESSURE. **BOLD TYPEFACE** IN THE **HEADINGS** HIGHLIGHTS PARAMETER CHANGES. **BOLD TYPEFACE** IN THE **TABLE** IS USED WHEN THE CHANGE IN APF VALUE EXCEEDED UNCERTAINTY LIMITS. 68
TABLE 5.2. THE EFFECT OF PARAMETER CHANGE ON INJECTOR ORDER. INJECTORS IN ASCENDING ORDER BASED ON AVERAGE APF VALUES. 69

1.0. Introduction

When designing an engine for consumer use, many elements are necessary in order to make a desirable final product. In general, an engine must be robust, powerful, lightweight, and inexpensive to manufacture in order to succeed in today's competitive market. While these factors are important, the prerequisite characteristic of an engine is its ability to meet the stringent emissions requirements set by the government.

Countries around the world have responded to the possible link between fossil fuel combustion and environmental degradation by enacting stringent emissions regulations. These standards have triggered an increased desire to understand the intricacies of combustion inside the cylinder. Preliminary research has stressed the importance of creating a well controlled fuel-air mixture within the cylinder in order to control combustion and thus reduce the amount of pollutants released into the atmosphere [1].

Limiting emissions is particularly difficult in two stroke engines, where short-circuiting can occur. Short-circuiting refers to fuel directly exiting the cylinder via the open exhaust port before scavenging is complete. This occurs in two stroke engines because the intake and exhaust ports are open simultaneously for a significant period of time during each engine stroke. The ports must be open at the same time because the piston is used to regulate the flow.

Direct fuel injection technology has been introduced to help reduce the amount of short-circuiting that occurs in two stroke engines. In previous two stroke engine designs, the fuel was introduced into the crankcase, either with a carburetor or a fuel injector, giving it ample time to create a homogeneous air/fuel mixture. During scavenging, where the intake

charge is used to push out exhaust gases, some raw fuel will exit the cylinder without combusting. If the intake charge is comprised solely of air, and the fuel is injected in-cylinder, this short-circuiting can be reduced.

The main challenge of direct injection technology is creating an appropriate air/fuel distribution in the cylinder in a very short period of time. Mercury Marine is an engine manufacturer currently using direct injection technology in their two stroke outboard engines. They chose to address this problem by using air-assisted fuel injectors. The fuel is introduced into a pressurized air source which is the driving force for injection. As a result, the injected fuel droplets are broken up into finer particles, encouraging quicker fuel evaporation and good mixing.

Air-assisted injectors are difficult to manufacture, so accurate testing procedures are required to ensure a properly performing product. Currently, Mercury Marine's supplier uses a back-illuminated two-dimensional spray profile test in order to predict injector operation. This spray profile test has been effective, but needs improvement as a significant amount of injectors are passed but produce misfires once they are installed into an engine. This is an expensive problem since it necessitates testing every engine and possibly uninstalling the bad injectors and reinstalling good injectors.

A major issue with the current testing procedure is that there is no information about the symmetry of the spray cone, which is an important performance parameter. It was hypothesized that an asymmetrical spray did not get close enough to the spark plug for the fuel to ignite. In order to measure the spray symmetry, it was necessary to take images of the spray firing towards the camera, rather than imaging the spray from the side.

Another problem with the test procedure involves the light source that illuminates the

spray. Currently a strobe light is used to back-illuminate the spray. The problem with this method is that there is no three dimensional information of the spray. In order to prove the hypothesis, it would be advantageous to illuminate only a thin sheet of the spray, at a specified location within the spray. To investigate fuel symmetry near the spark plug location, a laser sheet was passed through the spray at a position equal to the distance from the injector tip to the spark plug. Using a laser was desirable since it provided a concentrated light source, which was easily manipulated.

Creating a test vessel to satisfy the aforementioned parameters required a few basic features. In order to test the injectors, it was desirable to create an environment that was similar to engine conditions. Since engine pressures reach relatively high levels during fuel injection, it was necessary to create a test vessel that withstood such pressures. The vessel also had to provide optical access to both illuminate and image the spray, while providing a mechanism to prevent fuel from fouling these windows. In addition to satisfying these requirements, the vessel allowed easy access to windows for cleaning, while minimizing the time and effort required to change injectors.

The following research was conducted in an attempt to fulfill the following objectives. The main objective was to determine if more modern optical methods could accurately predict injector performance. Upon completion of that goal, testing procedures needed to be developed in order to allow for in-house testing at the manufacturing plant.

2.0. Background

2.1. Patternation Methods

Sprays have been studied in depth in hopes of improving the performance of many common items including fuel injectors, medicinal atomizers, and paint applicators. A number of methods have been employed to measure the performance of such items. The following literature review briefly describes some of these commonly utilized tools.

2.1.1. Phase Doppler Anemometry

Phase Doppler methods have been widely used as reference tools to verify the accuracy of other developing patternation methods [2-7]. In these methods, two laser beams are crossed in an area of interest, creating a probe volume sized to study individual droplets. The crossed beams create an interference pattern dependant on the wavelength of light and the angle between the beams. An array of detectors capture light scattered from the particles that pass through the probe volume. Particle size can then be determined from the phase shift of the frequency signals received by the different detectors [8]. Since the Doppler methods only measure a small amount of volume over a long period of time, such methods are not practical for rapid, full-scale spray characterization [4]. In addition, the accuracy of these methods can also be compromised in dense sprays where multiple droplets can simultaneously occupy the probe volume or if the signal becomes scattered by particles outside of the probe volume [2].

2.1.2. Mechanical Patternators

Before the development of more sophisticated methods, mechanical patternators were widely used for spray characterization. Early patternators typically consisted of an array of

tubes or a container divided into radial sections, while more sophisticated designs allowed for transient measurements to be taken [9]. The spray is characterized by measuring the amount of fluid collected in each section. While this method was useful in the past, a number of factors have lead to the decline of its use. In general, mechanical patternation is a slow and labor intensive process, which provides limited spatial resolution, and can disturb the natural flow field of an injector due to its intrusive collection process [10]. In addition, mechanical patternation is not well suited for testing at elevated pressures.

2.1.3. Laser Sheet Dropsizing

Laser sheet dropsizing (LSD), is a much less intrusive method of rapidly characterizing spray performance. In this method, a laser sheet passes through a spray, and light is collected at a 90 degree angle to the sheet from both Mie and laser-induced fluorescence (LIF) phenomena. The scattering and fluorescence signals occur at different wavelengths, which are separated through the use of optical filters [4]. This method depends on the assumption that LIF signals are proportional to the volume of a spherical droplet, and Mie signals are proportional to the square of droplet diameter. This assumption allows drop size information, in the form of Sauter Mean Diameter (SMD), to be extracted from the data by dividing the LIF signal by the Mie signal. Much research has been dedicated to proving the validity of this method [2,4-6,11].

While LSD is a novel method, there are a number of factors that can detract from its accuracy. While studies have correlated LIF signal to drop volume and Mie scattering to the square of drop diameter, it is common knowledge that both relationships can deviate due to a number of factors. One major factor that can affect the LIF signal is the concentration of fluorescent species in the liquid spray. Figure 2.1 shows that variations in the distribution of

fluorescing species in the fuel can greatly alter the relationship between LIF and droplet volume. In order for the cubic relationship to be maintained, the y-value of the graph should be as close to 3 as possible. Variations in the relationship between Mie scattered signals and the square of drop diameter are discussed in further detail in Section 2.4.

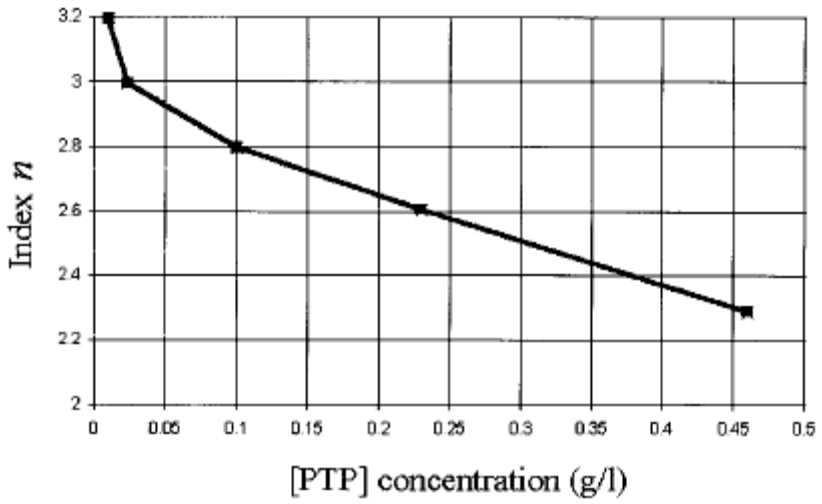

Figure 2.1. The relationship between fluorescent concentration and LIF signal response. At n = 3, LIF signals are assumed to be proportional to droplet volume. Reprinted from [4].

Using the LSD technique also requires the use of a number of components to achieve desirable results. For instance, most fuels do not contain species that fluoresce at common laser wavelengths, requiring the addition of a fluorescent dopant to the fuel. In large scale quality control applications, such doping is undesirable [5]. Achieving necessary spatial resolution can also be prohibitively expensive, since a large CCD array is required if LIF and Mie images are to be captured side by side on a single camera. The other alternative would be to use two cameras to capture each signal separately, which could be equally expensive [4].

2.2. Mie Scattering

Considering the goals of this experiment and comparing the characteristics of patternation methods, the decision was made to use the Mie-scattering technique to assess fuel injector performance. The following section describes the principles of Mie-scattering, and provides a brief explanation of a typical Mie-scattering experiment, followed by an in-depth analysis of some of the advantages and disadvantages of using this technique.

2.2.1. Mie Scattering Theory

The patternation method used in this experiment is based on elastic light scattering principles; meaning light is redirected by particles at the same wavelength as its excitation source. When light interacts with a particle, the particle can alter the direction of the photons due to mechanisms including reflection, refraction, diffraction, absorption and radiation. Early in the 20^{th} century, Gustav Mie and Ludvig Lorenz independently developed a theory that took into account these mechanisms to predict how light would scatter in different situations. According to Lorenz-Mie theory, the intensity of this scattered light depends on the diameter and refractive index of the particle, the angle between the illumination plane and the observation plane (scattering angle), and the wavelength and polarization of the illumination source, as well as other parameters [5-6]. Some research has shown a relationship between scattered signal and the square of particle diameter, when some of these parameters are kept constant [11].

2.2.2. Mie-scattering Setup

A typical Mie-scattering experiment is set up in the following way. Sheet forming optics create a thin, two-dimensional laser sheet which passes through a spray. This sheet is either oriented normal to the injector axis if cross sectional spray information is desired, or it

is aligned with the injector axis if spray profiles are to be studied. When spray droplets pass though the laser sheet, some light scatters out of the illumination plane. The amount of light scattered to a certain area can be quantified with an imaging device. The spray can be frozen in time though the use of a pulsed laser source, short camera exposure times, or a combination of both.

2.3. Multiple Scattering Issues

Much time and effort has been devoted to the goal of extracting droplet-size distribution data from Mie-scattered images. However, this goal has not yet been realized due to a number of fundamental problems that are caused by the secondary scattering of the Mie signal. The three major issues caused by secondary scattering are unknown laser extinction, signal attenuation, and out-of-plane illumination [3,7].

2.3.1. Laser extinction

Laser sheet extinction and Mie-scattering are fundamentally linked to each other. As light is scattered by the droplets in the plane of the laser sheet, the intensity of the laser sheet itself is reduced. Some photons are scattered more than once, so it is extremely difficult to predict the rate of laser sheet extinction as it passes through the spray. Because signal intensity is assumed to be proportional to spray density, an unknown laser sheet intensity distribution could cause sprays to be falsely characterized. For example, if a laser enters the left side of a symmetric spray with 100% of its initial energy, and exits the right side with only 50%, a researcher could falsely claim that the left side of the spray has more fuel. This issue has been rectified with the use of bidirectional illumination techniques [3,12]. This method illuminates a spray with two laser sheets, aligned in the same plane, but propagating in opposite directions. Sick found that this method is effective in providing a uniform light source if the spray being studied attenuates a single sheet by less than 80%, and if the two laser sheets have very similar initial intensities [12].

2.3.2. Signal attenuation and Out of Plane Illumination

Signal attenuation due to multiple scattering has been cited as a significant source of error in many spray patternation experiments [2-3,6-7,12]. Errors occur when the light

scattered by particles in the illuminated plane interact with spray droplets outside of the plane, altering the original path of light. Depending on how altered the path is, the photon could end up on a different pixel in the camera array, or miss the camera entirely, thus going undetected. This causes blurring and attenuation of the original signal. Scattered photons can also illuminate droplets outside of the plane, an occurrence referred to as out-of-plane illumination. This compromises the integrity of the data set, since the researcher cannot differentiate between the in-plane particles of interest and the unintentionally illuminated out-of-plane particles.

Many attempts have been made to correct for secondary scattering errors. Mathematical methods have been researched; however, even if the most basic scattering laws are employed, the complexity of the math involved makes quantification extremely difficult [6]. To avoid such difficulties, Talley proposed an experimental approach to minimize the effects of secondary scattering. Rather than using a full sheet, Talley used a beam that was swept through the region of interest, with the idea that the lower net intensity of the illumination source would yield less signal attenuation and out of plane illumination [7].

Due to the complexity of multiple scattering issues, no attempts were made in this project to correct for its effect on signal attenuation and out-of-plane illumination. A scattering simulation study done by Jermy justifies the ability to neglect such effects. They found that despite the fact that 50% of their hollow cone spray was multiply scattered, most photons struck the pixel that was its original target. They explained that the scattering was forward dominant, so alterations in the path of the photon were very minor. One finding of their research was that attenuation was somewhat significant in particularly dense regions where multiple scattering was more prevalent [13]. Because the goal of this project was to

differentiate between injectors rather than fully characterize them, such errors factor into all images, therefore no attempts were made to correct for them.

2.4. Other Mie-Scattering Shortcomings

A couple of fundamental factors prevent drop sizing information to be extracted from Mie-scattered images. These issues are demonstrated in Figure 2.2, which plots the relative Mie-scattered intensity as a function of droplet diameter. The first issue is that a number of droplet sizes can produce the same signal intensity, shown by the fluctuations in the Mie trace. The other issue is that at small diameters, (<50 μm) the Mie trace has a greater amplitude than the D^3 trace, meaning that Mie-scattering images will overestimate the actual amount of small particles in the spray. It should be noted that Mie signals are usually compared to the square of the diameter, but similar trends would be shown if the D^3 trace were replaced with a D^2 trace.

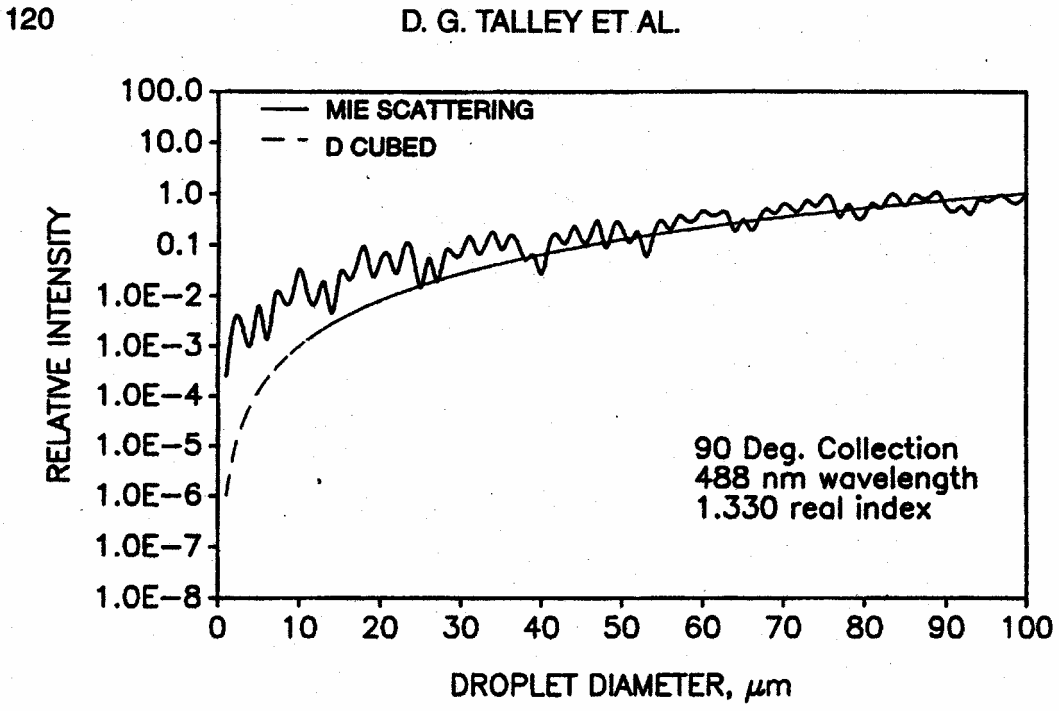

Figure 2.2. Actual Mie scattering signal compared to a theoretical signal based on droplet volume. Reprinted from [3].

Present experimental methods also make drop-sizing difficult. Because camera pixel size is significantly larger than the photons scattered from the laser/spray interaction, each pixel contains information from a number of scattered droplets [5]. As a result, it is impossible to gain information about the level of contribution each droplet makes to a pixel. Also, it is common practice to characterize an injector by averaging a number of images. Doing so reduces the effect of camera noise as well as reducing the effect of injector variability. A consequence of this practice is that averaged images generally are an indication of an average spray distribution. With all of these factors in mind, no attempts at drop sizing were made in this experiment. Instead, Mie images were only used as a general indicator of injector performance.

2.5. Virtues of Mie-scattering

Most of the advantages of using a Mie-scattering technique center around its ability to characterize an injector quickly and relatively easily. As shown in Figure 2.3, Mie-scattering produces images that look very similar to LIF images, without requiring the additional spectral filters, optics, cameras and dopant. Because it is a planar optical method, the method is both unintrusive, and essentially takes a large number of simultaneous point measurements at once, giving it an advantage over mechanical patternators and PDA. Since the research conducted did not require quantified data, Mie-scattering was the best available option.

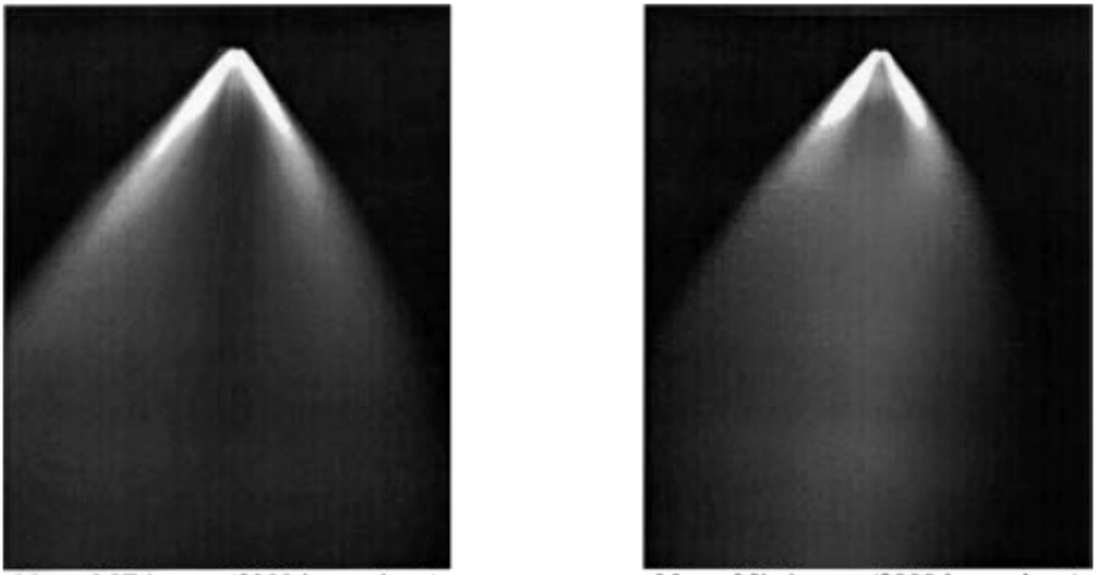

Figure 2.3. Mean LIF and Mie scattered images of a fuel injector spray. Reprinted from [4].

3.0. Experimental Setup

To analyze and compare the air-assist injectors, a relatively simple apparatus was developed. The apparatus consisted of three main components: a fuel delivery system, a test vessel, and a data acquisition system. This setup allowed images to be captured at various vessel pressures and injector conditions. The list of equipment is located in Appendix A.

3.1. Fuel System

The fuel system used for this project was taken directly from a production two-stroke direct injection engine constructed by Mercury Marine. The major components of the fuel system are a modified injector rail, a two stage fuel pump, and a software-controlled electronic control unit.

3.1.1. Air-Assist Injector

The injection system was virtually identical to the Optimax system in production, with the exception being that it had been cut down to a third of its original size. A diagram of the production fuel rail is shown in Figure 3.1. The rail held one fuel injector and one air injector, and had supply and return lines for both fuel and air. The fuel injector injected a specified amount of fuel (5.2 mg) into a chamber inside the air injector, where it was given a user-specified amount of time (0.952 or 4 ms) to mix with a small amount of air, which entered from the air supply line on the fuel rail. The air fuel mixture was then injected into the cylinder through the air injector, which was kept open for a user specified amount of time (3.8 ms). A differential pressure regulator inside of the rail kept the fuel pressure 70 kPa higher than the inlet air pressure, which was kept at 650 kPa atmospheric. The fuel return

line sent unused fuel back to the pump system while excess air was sent to the building exhaust system via the air return line.

3.1.2. Fuel Pressurization System

Fuel was delivered to the rail with a fuel pump system containing a lift pump, a medium pressure pump, and a high-pressure pump. The three pump system was advantageous for a number of reasons. The most applicable advantage utilized in this experiment was that the fuel return line was fed directly into the high pressure pump, bypassing the lift and pressure pumps. A diagram of the fuel pump system used is shown in Figure 3.2. Power for the pumps came from an Astron DC power supply. The fuel used in this experiment was EEE, made by Halterman Products. This research fuel had qualities similar to typical pump gas, but its chemical composition was more tightly controlled.

3.1.3. Fuel Control System

The entire fuel system was controlled by a production engine control system. The engine control unit (ECU), a PCM-0312M designed by Motorola for Mercury Marine, allowed for continuous adjustment of system parameters during operation. Changes could be made to the ECU from a personal computer equipped with the Mototune software produced by Mototron. Few of the ECU's features were used in this project, as it was only responsible for controlling fuel and air injector timing, in addition to producing a signal that was used to trigger the camera and the laser.

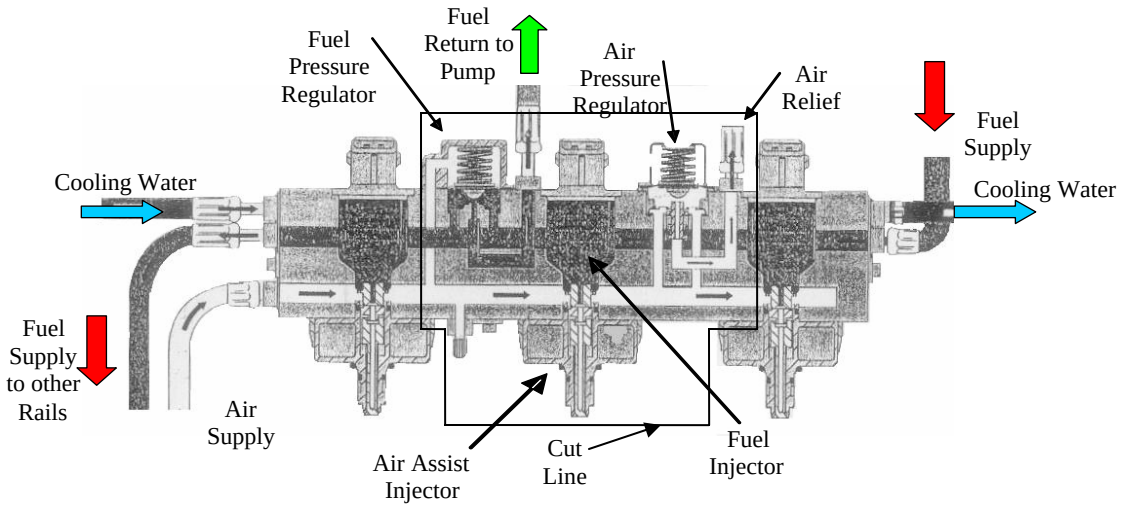

Figure 3.1. Production Optimax Fuel Rail. Reprinted from [14].

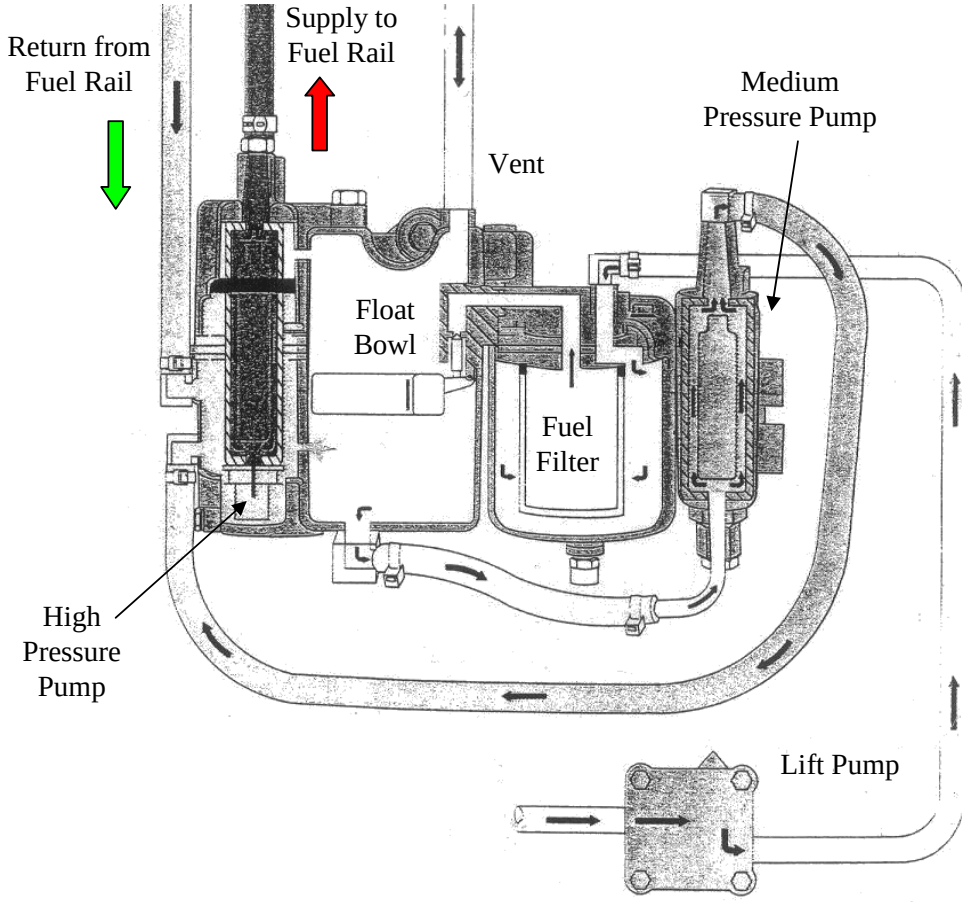

Figure 3.2. Production Optimax Fuel Pump. Reprinted from [14].

3.2. Fuel Injector Test Vessel

In order to characterize the injectors in a controlled environment, a test vessel was constructed. This vessel was designed by Lonny Peet and Chris Behrendt under the supervision of Prof. Jaal Ghandhi as a project for the Engine Research Center Undergraduate Research Fellowship program, and was constructed by Mercury Marine. A picture of the vessel and its features is shown in Figure 3.3. The vessel was designed with a few basic principles in mind. An essential feature of the vessel was to have two points of optical access: one that allowed for spray illumination, and another that allowed for image capture of the spray. In addition to these features, a system needed to be created to keep the windows clean while preventing fuel from pooling in the vessel. The vessel needed to be robust enough to withstand moderate pressurization (650 kPa atmospheric), while having a modular design that would allow for easy modification. Appendix B contains engineering drawings of the fabricated vessel components.

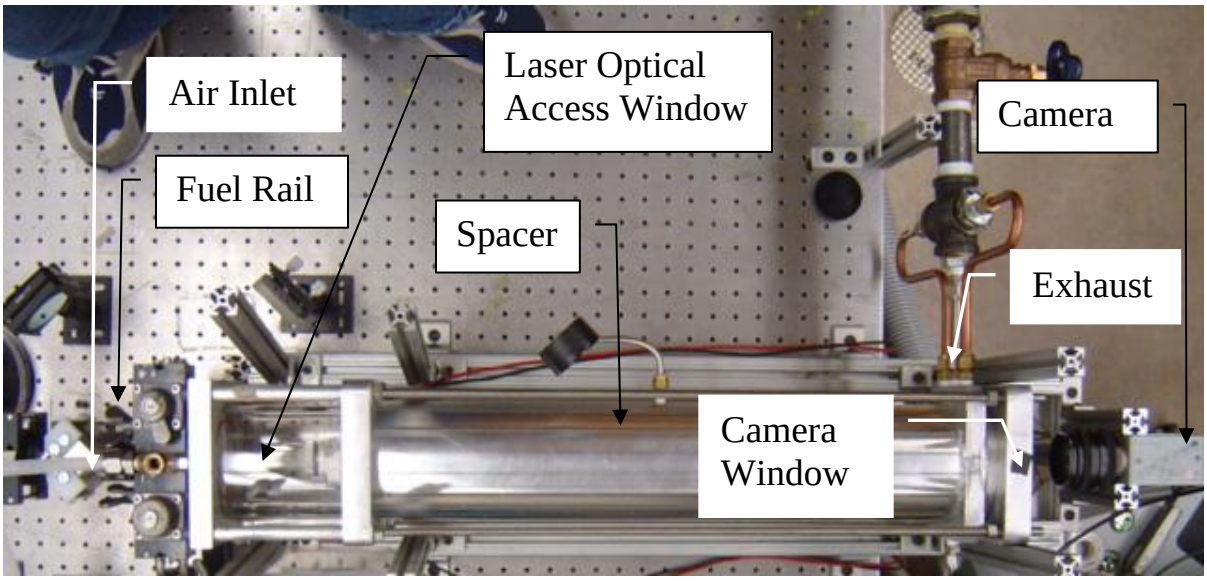

Figure 3.3. Aerial view of test vessel.

3.2.1. Optical Components

Optical access was achieved through the use of two pieces of borosilicate glass, sized to withstand the pressure requirements of the vessel. To gain optical access for spray illumination, a borosilicate glass cylinder was placed coaxially with the axis of the air injector, with one end of the cylinder aligned with the tip of the air injector. The cylinder dimensions (9.5 cm ID, 10.8 cm OD, 12.7 cm long) allowed for the laser to be positioned at a wide variety of distances from the injector tip, enabling full spray characterization. A flat, circular piece of borosilicate glass (7.6 cm OD, 9.5 mm thick), located at the end of the vessel, permitted the camera to take images at an angle directly perpendicular to the direction of the spray. Figure 3.4 shows a picture of the camera and sight glass orientation. The sight glass was sized using [15],

$$P = \frac{S * M * t^2}{k * A} \qquad (3.1)$$

where P is the burst pressure, S is the shape factor (3.48 if window is rectangular, 3.12 if circular), M is the tensile strength of the material, t is the thickness, k is the safety factor, and A is the unsupported area. It is important to note that due to the brittle characteristics of glass, this equation was used as a rough guide for sizing, but was not relied on for disaster prevention. Imperfections in the glass can cause stress concentrations that can rapidly propagate throughout the piece, leading to catastrophic failure.

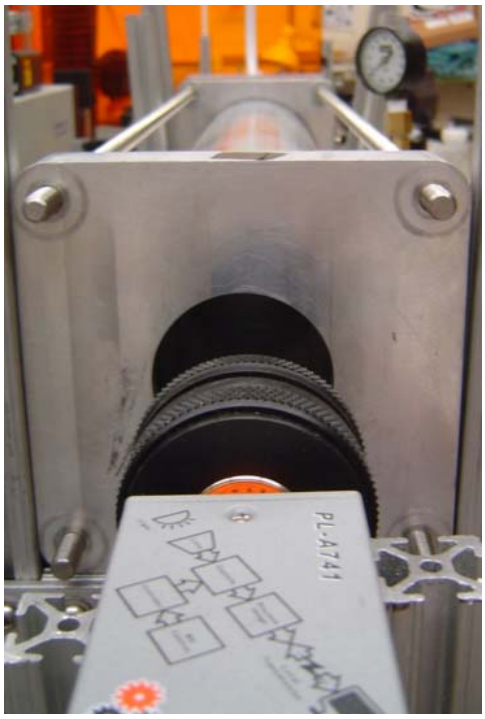

Figure 3.4. View of camera optical access window.

3.2.2. Air Circulation System

In order to keep these windows free of fuel, while flushing fuel out of the exhaust, a continuous flow of air needed to be circulated through the vessel. However, it was important that this flow of air did not interfere with the fuel spray. In order to satisfy these requirements, an original design was implemented that created a flowfield in the cylinder that developed higher velocities near the walls of the glass cylinder and lower velocities near the fuel spray.

To generate this velocity profile, two sintered metal discs, manufactured by Mott Corporation, were installed between the air inlet and the test vessel. Sintered metal parts are often used for filter applications, since they have a uniform porosity that allows air to pass through, while blocking particles larger than a specified size. In this experiment, a 5 μm

porosity, 1.57 mm thick sheet, was machined to create a disc with a 6.985 cm OD and a 1.295 cm ID. A second disc, with 10 μm porosity and the same thickness, was fabricated to have a 9.398 cm OD and a 1.295 cm ID. These discs, shown in Figure 3.5, were coaxially aligned in series, so that air near the cylinder wall only passed through the less restrictive 10 μm disc, whereas air closer to the center took the more restrictive path through both the 10 μm and the 5 μm discs. The less restrictive path promoted high velocities in the outer region, creating a buffer between the fuel and glass window.

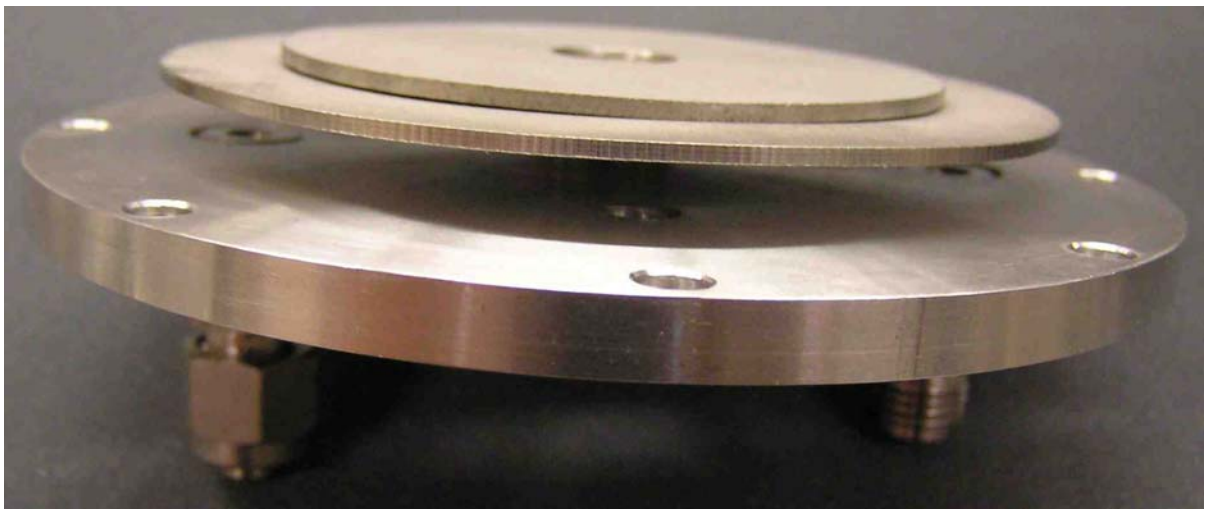

Figure 3.5. The two porous metal discs, coaxially aligned in series on the injector housing.

In order to hold these discs, an elaborately machined aluminum piece, resembling the cross-hairs of a gun sight, was designed and fabricated. The “cross-hair” mounting system, shown in Figures 3.6 and 3.7, was also responsible for housing the air injector and aligning and sealing the porous discs. Silicone sealant was used to create a seal between the porous material and the aluminum housing.

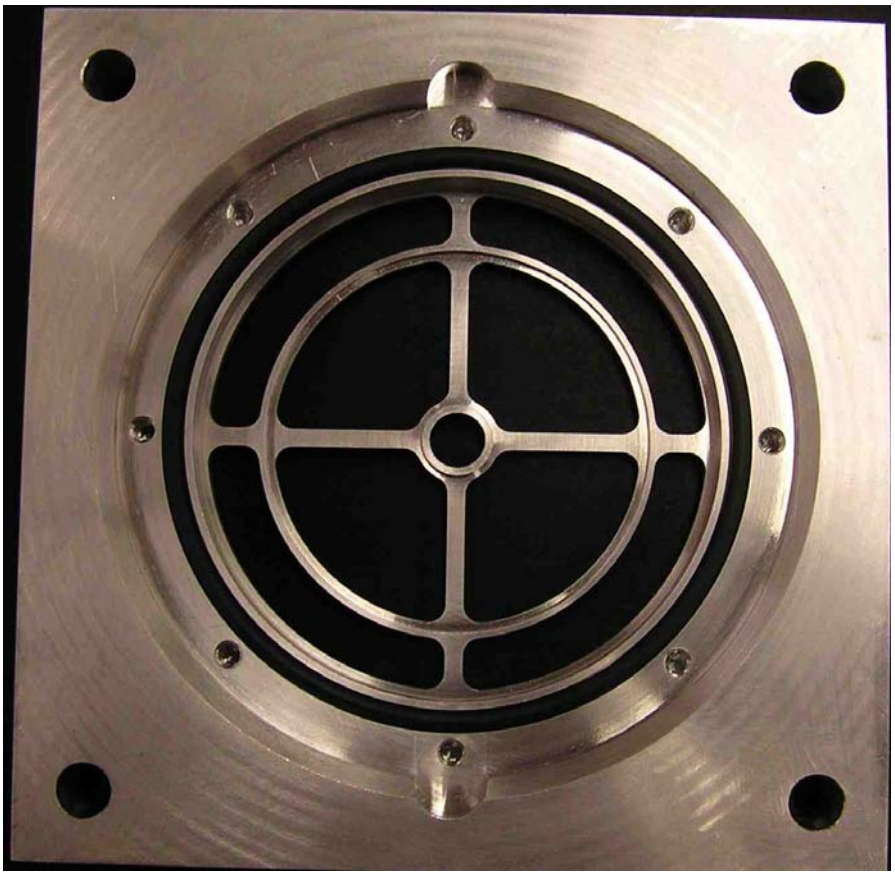

Figure 3.6. Backside of "cross hair" housing. This housing mates with the injector holder in Figure 3.5 to align and secure the injector and porous metal.

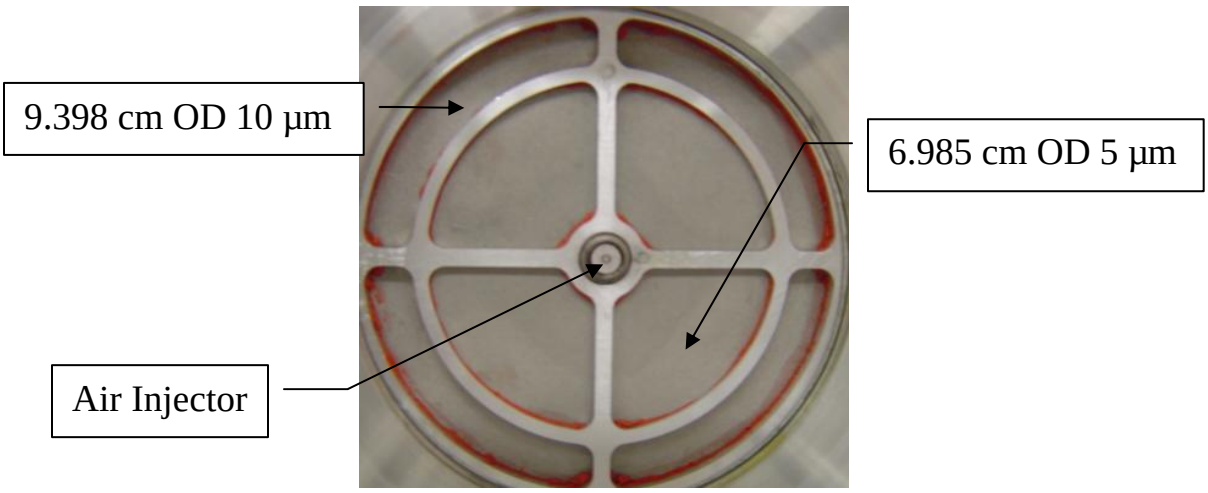

Figure 3.7. A view from inside the vessel of the injector and porous metal holder assembled.

The air supplied to the inlet of the test vessel came from the building compressed air system. The maximum line pressure was about 650 kPa atmospheric, but it varied slightly with time. The distance between the vessel inlet and the house air valve was significant enough to necessitate the use of a 7.6 m long nylon tube. Because the fuel rail was placed in the same area as the air inlet to the vessel, space constraints limited the inner diameter of the tube and fitting to 9.40 mm. The relatively long length of the line, coupled with its small diameter led to significant pressure drop due to friction, but for the testing conditions chosen, this did not restrict flow enough to cause significant window fouling.

In order to keep the optical access window for the camera clean, it was necessary to distance the window from the fuel spray. For example, if the window was placed 20 cm away from the fuel spray, it would be very difficult to keep the fuel from impinging on the window. With that in mind, a long cylindrical metal spacer (61 cm long, 10.2 cm ID, 11.4 cm OD) was installed between the laser access window and the camera access window. Four threaded rods (66 cm long, 3/8”-16 thread) were used to clamp the spacer between the camera and laser access window housings. The spacer is made of 6061 aluminum, and the threaded rod is made of 18-8 stainless steel. In addition to providing space between the injector and the camera window, the spacer was tapped to allow the installation of a pressure gauge, an exhaust line, and an additional air inlet line.

The contents of the vessel exited out of the side of the apparatus, adjacent to the camera window. This configuration was adopted in order to allow the camera to be directly normal to the laser sheet that illuminates the fuel. The initial design of the vessel allowed for a second air inlet to be attached in order to provide a stream of air that would help keep the

camera window clean. However, testing the setup without the second line attached showed that the window remained reasonably clean on its own.

It is important to note that the flange that was welded on the end of the vessel where the exhaust is connected was designed in error. The 1.9 cm thick plate was intended to be much larger to accommodate an exhaust pipe of 2.5 cm or larger. In order to minimize the flow restriction, three 6.99 mm ID fittings were attached to the flange and elaborately connected to a 2.5 cm ID pipe. While this setup was adequate for our tests, higher flow rates could be realized in the vessel if a less restrictive exhaust was fabricated.

3.3. Optical System

Spray illumination and visualization was achieved using the Mie scattering technique. The sheet that illuminated the spray was created using a laser, whose beam was manipulated using a number of optical components. The illuminated spray image was captured using a software-controlled camera that was connected to a computer which stored and processed the images.

3.3.1. Laser Source

The light source used for this experiment was a Lexel (Model 95) argon ion laser. This laser was a continuous wave type, and was operated in multiline mode, producing light primarily at 488 and 514 nm. In normal operating conditions, the laser received 25 amps of current from its 208 VAC voltage source, with the power source set to current control mode. Constant adjustment was required in order to reduce the amount of variability in the laser sheet intensity. Laser power was measured before and after each set of data by a Newport 815 digital power meter. The placement of the meter in the optical setup is shown in Figure 3.8.

3.3.2. Optical Setup

The optical setup is shown in Figure 3.8. A Bragg cell (Intraaction AOM 405) was used to convert the continuous beam into a pulsed source, which was triggered when an image is captured. A beam stop was placed downstream of the Bragg cell, and allowed only the first mode to pass through, while blocking all other modes. The mode that was allowed to pass was at a slight angle to the original beam, so when the Bragg cell was not activated, the single beam was blocked by the beam stop.

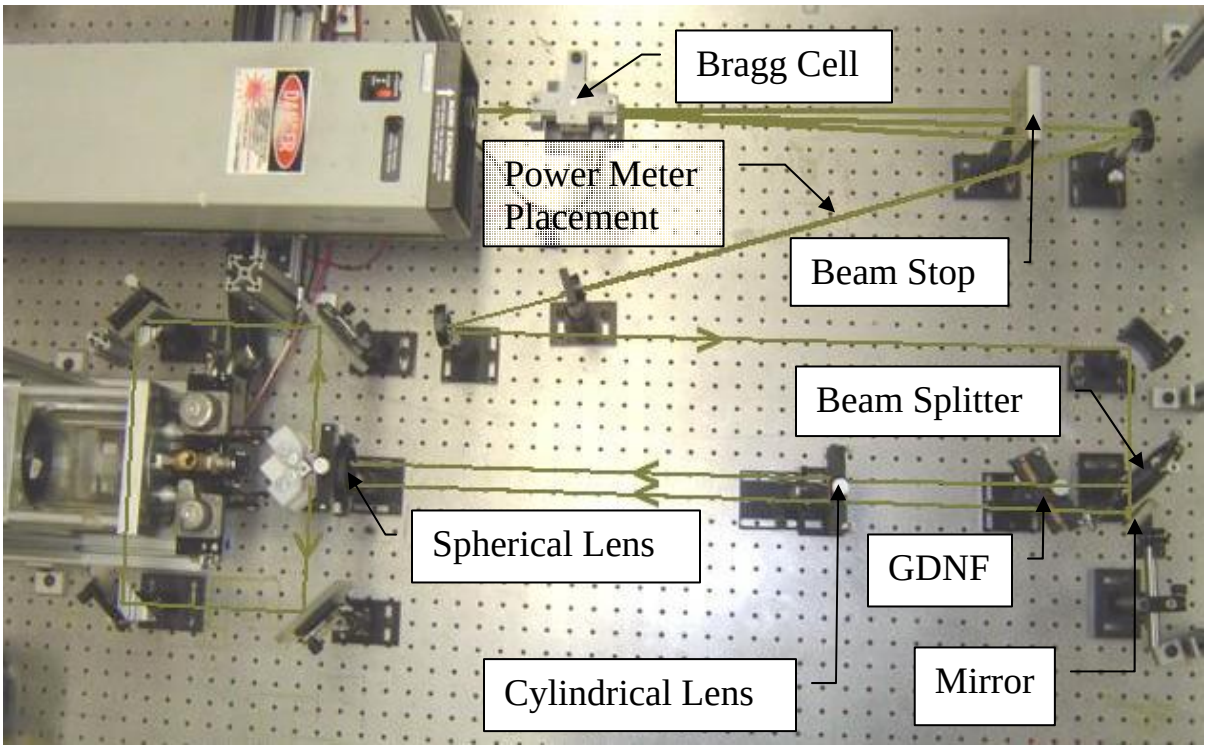

Figure 3.8. Optical Setup.

After the beam passed through that initial set of optics, it was split into two beams of equal intensity. To allow both beams to pass through a single set of sheet-forming optics, a mirror was placed directly adjacent to the beam splitter, which positioned the transmitted beam parallel to the reflected beam, with about 2 cm of space between the two beams. Since the beam splitter did not produce two perfectly equal beams, a graded neutral density filter (GNDF) was used to balance the power. The GNDF was a flat, rectangular sheet of glass that had steps of shades that varied from almost black on one end to fully transparent on the other.

Once the two beams had approximately equal intensities, they passed though a set of sheet-forming optics. The beams first passed through a cylindrical lens, which expanded them in the vertical direction. To protect the researcher from scattered light, an iris was positioned just past the cylindrical lens to block unused light. Because a sheet with a fixed

height was desired, a spherical lens was placed in the laser path at a distance where its focal point was aligned with the focal point of the cylindrical lens. At this distance, the spherical and cylindrical lenses combined to create sheets with constant height, which was the desired geometry for spray illumination. The combination of the cylindrical and spherical lens also created a waist at the focal length of the spherical lens, where the sheet had a minimum thickness. The focal length of the spherical lens was positioned at the center of the test chamber, minimizing sheet thickness in the spray imaging plane.

A set of mirrors is then used to orient the sheets so that they pass through the laser access window in the same plane, but in opposite directions. This method is known as bidirectional illumination, which is used to counteract signal attenuation that occurs as a sheet passes through the spray.

3.3.3. Camera

Images were captured with a Pixelink A-741 CMOS camera. This camera was selected because it has a moderate frame rate and was reasonably priced. The camera was connected to a computer via a firewire (IEEE 1394) interface, and was controlled with Pixelink Capture OEM software. Table 3.1 shows the values of the user-adjustable features used during this research; all other features were left in the default setting. The brightness level was matched with the gain to ensure the signal would not be clipped, as is explained in Appendix C. It should be noted that the flat field correction program was run for this camera before taking data, since the default flat field was calibrated at a gain level of 0 dB.

The lens used for this camera was a 50 mm JML f/1.3 model, which required two spacers whose thicknesses summed to 1.5 mm. These spacers allowed the camera to focus on the plane of interest; previously, the plane of interest was inside the minimum focal range.

Exposure Time	.3 ms
Gain	13.2 dB
Brightness	3%
Pixel Size	360x360 (centered)
Pixel Format	MONO16
Trigger Mode	0
Trigger Type	Hardware
Trigger Polarity	Positive
Trigger Delay	0 s
Time Lapse Capture	Every 175 ms

Table 3.1. Camera Settings.

3.3.4. Component Triggering

The camera and laser were synchronized with the air injector through the use of a Quantum Composers pulse generator. Set to gate mode, the pulse generator received an input signal from the Mototron spark output, which was set to trigger at the same time that the air injector opens. Two of the four available outputs of the pulse generator were used for the camera and laser trigger signals. These signals were delayed from the rising edge of the input signal at different intervals, depending on which stage of injection was to be observed.

3.3.5. Image Processing

Captured images were processed using both Matlab and TSI Insight 3G software. In order for the images to be background subtracted and averaged in the Insight 3G software, the file names needed to be changed in Matlab to match the filenames that Insight assigns to its captured images. For example, a data image captured with the Pixelink software would be named “data1.tif.” To work with the Insight software, this name had to be changed to “data1Cap000001.T000.D000.P000.H000.plif.tif.” Insight was a valuable tool because it could divide an image radially (into pie pieces) or concentrically (coaxial rings) for statistical analysis.

4.0. Calibration of Testing Conditions

The following chapter details the development of the apparatus for testing and the proper testing conditions. The individual tests are grouped into three main topics: air flow calibration, secondary scattering studies, and test condition selection.

4.1. Air Flow Calibration

The test apparatus in its original form needed significant modification in order to generate sufficient airflow to keep the optical windows clean. Aside from increasing the diameter of the inlet and exhaust lines, less-restrictive porous metal discs were required. This section discusses the method of selecting the porosity of the discs, shows the results of apparatus flow measurements, and presents the effects of air flow on fuel spray geometry.

4.1.1. Porous Metal Disc Selection

In order to increase the flow of air inside the apparatus, less-restrictive porous metal discs were installed. Since Mott Corporation makes sintered-metal sheets with six different porosities, selecting the correct size for each disc required research, modeling, and testing.

The permeability chart supplied by Mott Corporation, shown in Figure 4.1, was the major tool used in the material selection process. The graph shows the relationship between the air flow rate and pressure drop for the six different porosities. The air flow through the sheet is defined as the volumetric flow per unit sheet area. It should be noted that the permeability chart is only valid if the pressure downstream of the sheet is atmospheric. The chart is constructed using the following equation [16]:

$$\Delta P = (K_g)(F)(\mu)(t) \qquad (4.1)$$

where ΔP is the pressure drop across the sheet (psid), K_g is the permeability coefficient, F is the flux through the sheet (acfm/ft^2), μ is the viscosity of the fluid (cp), and t is the thickness of the sheet (in). The chart intuitively shows that more porous metals allow more flow for a given pressure drop, and higher pressure drops are linked to higher flow rates.

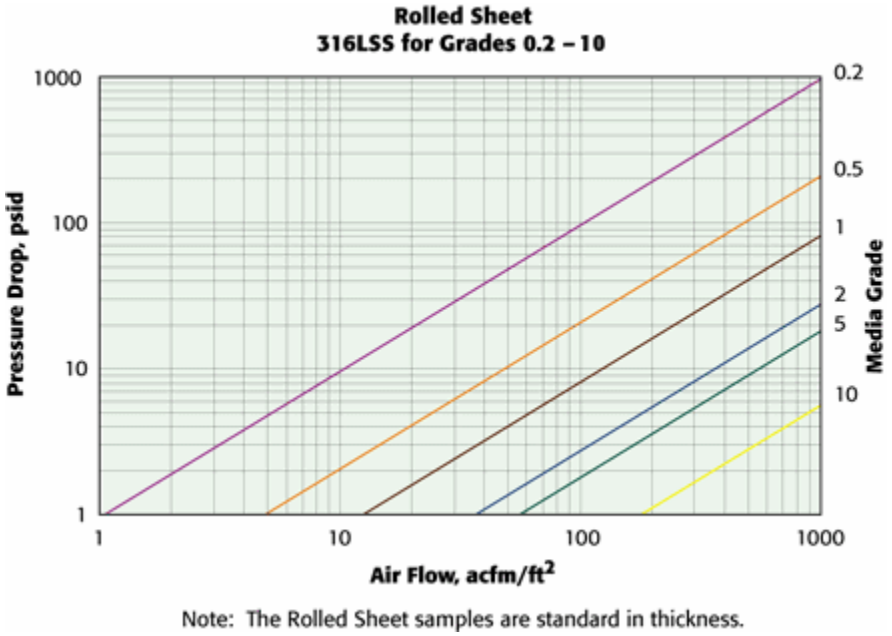

Figure 4.1. Manufacturer specified air flow characteristics of Mott porous metal sheets. Reprinted from [17].

To verify the results of Figure 4.1, a simple test was conducted as shown in Figure 4.2. A 0.2 µm porous metal disc with a 1.15" (2.92 cm) diameter was installed into a pipe union, which was used to connect two 1" (2.5 cm) pipes. Upstream pressure was monitored with a pressure gauge tapped into the 1" (2.5 cm) pipe, and flow was measured using a stopwatch and bellows meter. Flow rates were measured at upstream pressures of 20, 40, and 60 psig (239, 377, and 515 kPa). The measured flow rates were then inserted into Equation (4.1) to solve for the expected pressure drop. The results of the test are shown in Table 4.1.

While there was a significant difference between the expected and measured pressure drop for the three different flow rates, the two sets are in close proximity and show similar trends.

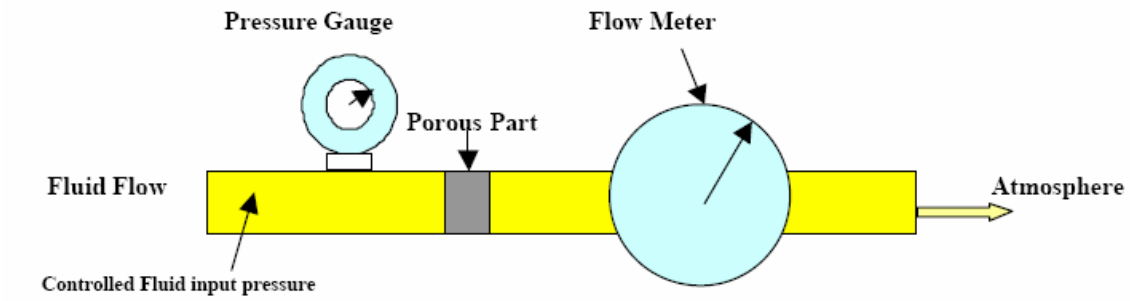

Figure 4.2. Simple porous metal flow verification test setup. Reprinted from [18].

Flux (acfm/ft^2)	Actual Pressure Drop (psi)	Theoretical Pressure Drop (psi)	Flux ((m^3/s)/m^2)	Actual Pressure Drop (kPa)	Theoretical Pressure Drop (kPa)
25.3	20	25.3	0.129	138	174
40.9	40	40.9	0.208	276	282
56.5	60	56.5	0.287	414	390

Table 4.1. Results of simple porous metal flow verification test.

After verifying the permeability data for a single disc, the model shown in Figure 4.3 was formulated to predict the flow characteristics of the porous metal configuration used in the test apparatus. The model assumed that air passing through the vessel could take only two paths. It could either pass through the more-restrictive inner region, where it must flow through both discs, or pass through the less restrictive outer region, flowing through only the outer disc. It was also assumed that the pressure drop across the inner region was equal to the pressure drop of the outer region. Using these assumptions and Equation (4.1) this set of four equations was formulated:

$$\Delta P_i = (F_i)(\mu)(K_{g_i} t_i + K_{g_o} t_o) \qquad (4.2)$$

$$\Delta P_o = (F_o)(\mu)(K_{g_o})(t_o) \qquad (4.3)$$

$$\Delta P_i = \Delta P_o \qquad (4.4)$$

$$V = (F_i)(A_i) + (F_o)(A_o) \qquad (4.5)$$

Viscosity μ is found from ambient temperature readings, permeability coefficients K_{g_i} and K_{g_o} are properties provided on the Mott Corporation permeability chart, and t_i and t_o are the thicknesses of the inner and outer metal discs. When initially choosing the discs, a desired pressure drop was specified, so the set of equations were used to solve for the fluxes F_i and F_o and volumetric flow V.

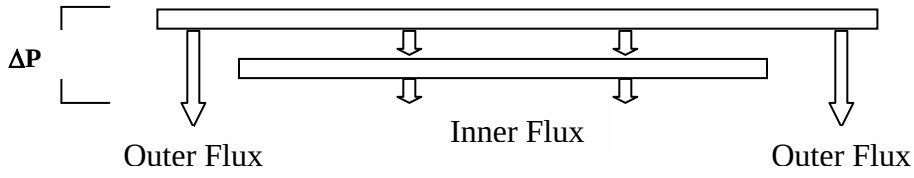

Figure 4.3. Diagram of porous metal arrangement in test vessel.

It was desired to increase flow as much as possible, so the 10 µm disc was chosen for the large disc size. For the inner disc, the 5 µm was selected, based on the flux values from the model. The combination of the two discs formed a velocity ratio F_o/F_i of 5, which was determined to be sufficient to create an air buffer to keep the windows clean, but not excessively high as to produce shearing between the fast outer velocity region and the slow inner velocity region. Once the discs were installed into the apparatus, the model was used to compare measured and expected values. In this case, volumetric flow V was found from bellows meter measurements, leaving the fluxes F_i and F_o and pressure drops ΔP_i and ΔP_o as the unknowns solved for in the set of equations. The results are shown in Table 4.2.

Unpressurized Flow (acfm)	Expected Pressure Drop (psi)	Actual Pressure Drop (psi)	Unpressurized Flow (m^3/s)	Actual Pressure Drop (kPa)	Theoretical Pressure Drop (kPa)
23.2	3.0	8.0	0.0110	20.7	55.2

Table 4.2. Flow data from porous metal arrangement in test vessel.

There are a few possible reasons why the expected and actual pressure drop values differed. Since the actual pressure drop was higher than expected, pores could have been plugged from either the machining process or from regular use. When the discs were machined, they were clamped tightly between two aluminum discs to provide lateral stability. The process of doing this could have compromised the porous structure slightly. Also, when the new porous metal sheets were installed, a significant amount of dirt had built up on the old discs. It was evident that the discs were filtering out a substantial amount of dirt from the air stream. To keep the porous metal material clean, a filter was installed upstream at the building air outlet. Another possible reason for the larger-than-expected pressure drop could be that the model did not sufficiently represent the air flow through the porous metal structure. The model assumed that flow path was entirely dictated by path restriction. However, the small chamber between the porous metal and the apparatus inlet may not have been large enough to create a uniform flow upstream of the discs, so it might have been more difficult for air to take the less-resistant outer path.

4.1.2. Flow Measurements

Once the final apparatus was configured, flow measurements were taken in order to determine the maximum injection frequency that kept the optical windows clean. It was discovered early that, despite the increased flow through the apparatus, windows were still fouling at moderate injection frequencies. So a correlation was developed to find the

maximum allowable injection frequency based on the flow in the chamber. Injection frequency was found by dividing the velocity inside the cylinder by the length of the glass laser optical access section. This value represented an estimate of the highest frequency that allowed the contents of one injection to leave the optical section before the start of the next injection. While the momentum of the spray propelled much of the fuel at a rate faster than the chamber air velocity, it is suitable to use the air velocity as an approximation of the speed of the slowest moving fuel.

The flow measurements were taken at two data points. The first data point represented the maximum flow that would not pressurize the chamber, which occurred at an air inlet pressure of 156.5 kPa atmospheric. The second data point was taken with the building compressed air line fully open, and with the gate valve in the exhaust line partially closed to pressurize the chamber to 377 kPa atmospheric. The first data point was chosen for its simplicity. If conclusive testing could be done at atmospheric conditions, money could be saved since components would not need to be rated for elevated pressures. The second point was chosen to best simulate engine conditions. This is discussed in Section 4.3.1. Flow measurements were taken with a bellows meter (Singer AL-800 77s6152589) and a stopwatch, with splits recorded at intervals of 10 scfm (0.0047 m^3/s). The results of the test are shown in Table 4.3. With these results in mind, the decision was made to run tests at 250 rpm (effective). This setting sets the injection frequency to 4 Hz, which is sufficiently below the maximum allowable frequency for either data point.

Vessel Pressure (psig)	Vessel Pressure (kPa)	Flow (acfm)	Flow(m^3/s)	Frequency (Hz)
0	101	23.2	0.0110	12.1
40	377	12.2	0.00576	6.4

Table 4.3. Results of apparatus flow measurements.

4.1.3. Variable Flow

There was concern that the air flow in the apparatus would influence fuel spray geometry, so a test was set up to investigate such effects. In the test, images were captured at five different flow rates. The flow rate was controlled by the building compressed air valve, which varied the line pressure. Each of the five images shown in Figure 4.4 represent the average of 100 background-subtracted images, captured at each flow rate. The pressures listed with each data set were taken at the chamber inlet, which is proportional to flow rate. To compare the overall geometry of the flow, the intensities were scaled automatically, using the medium contrast setting in the Maxim DL screen stretch feature.

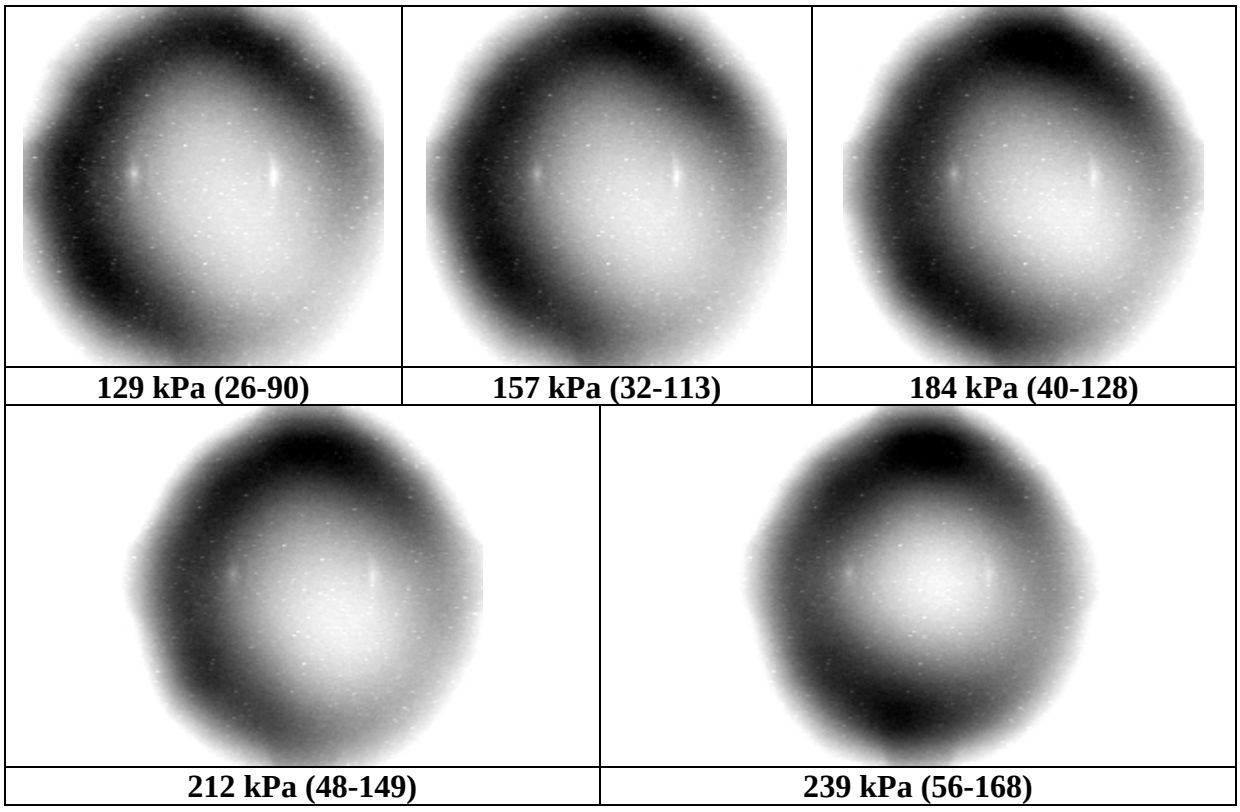

Figure 4.4. Spray images with varying vessel air flows. Pressures are measured at the inlet of the vessel. Pixel ranges are given in parenthesis from the Maxim medium autoscale setting. All pressures are atmospheric.

With the intensities scaled, the images appeared to be relatively similar. Small differences can be seen as flows increased, with the outer diameter of the spray decreasing slightly and the hollow cone becoming more symmetrical. As was previously mentioned, restrictions in the chamber exit caused the vessel to pressurize at inlet pressures above 157 kPa. At full flow, which occurred at the inlet pressure of 239 kPa, the chamber pressure reached 157 kPa. Ambient pressure increases usually have a tendency to collapse sprays, which could explain the decrease in the outer diameter of the spray. However, in other tests when the vessel was pressurized to 377 kPa, spray diameter increased, which would contradict the previous explanation.

The lower and upper boundaries of the pixel intensity range used for the medium contrast setting are given in parenthesis in Figure 4.4. From these values, it is apparent that one effect of increased flow was a rise in pixel levels. This could be because increased flow can increase the amount of fuel that crosses the laser sheet for the same sheet geometry and exposure times.

4.2. Secondary Scattering Effects

As explained in Section 2.3, secondary scattering compromises the accuracy of planar imaging techniques. The following section describes the initial tests performed to assess the severity of multiple scattering in this experiment. The first test measured the amount of laser extinction through the spray, the second test measured the amount of out-of-plane illumination that occurred in the imaging process, and the final test measured the blurring of the image.

4.2.1 Laser Sheet Extinction

This experiment was conducted in order to measure laser sheet extinction and assess the need for bidirectional illumination. Three sets of spray images were taken, one set with only the left-traveling sheet incident upon the spray, one set with just the right-traveling sheet, and one set with both sheets. Each image shown in Figures 4.5 and 4.6 is a background subtracted average of 100 images. Data in Figure 4.5 had a fueling rate of 5.2 mg/cycle, while Figure 4.6 had a fueling rate of 15.6 mg/cycle. To quantify the attenuation, an intensity profile of the spray image was taken. The profile measured 10 pixels high and was oriented horizontally across the center of the image. As the left and right profiles show, significant laser sheet attenuation across the spray occurred. The profile that was illuminated from both sides show that attenuation was minimized using bidirectional illumination techniques. Data taken for the higher fueling rate showed the trend more clearly.

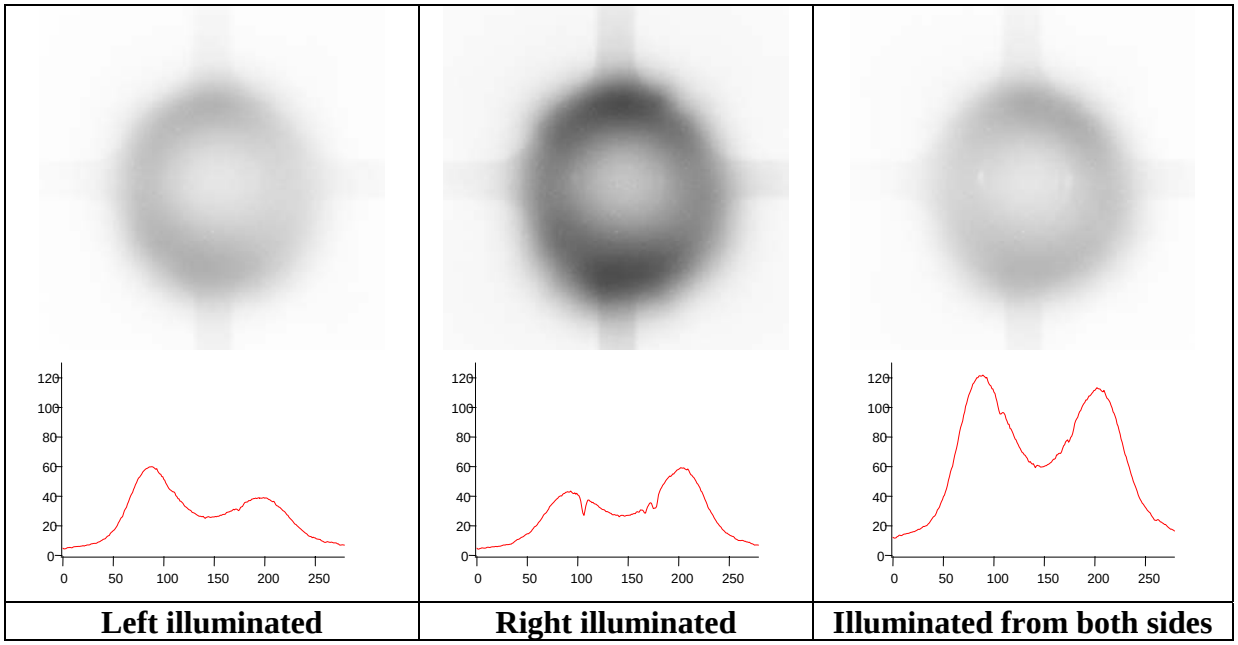

Figure 4.5. Results of laser sheet extinction test. Fueling rate is set at 5.2 mg/cycle.

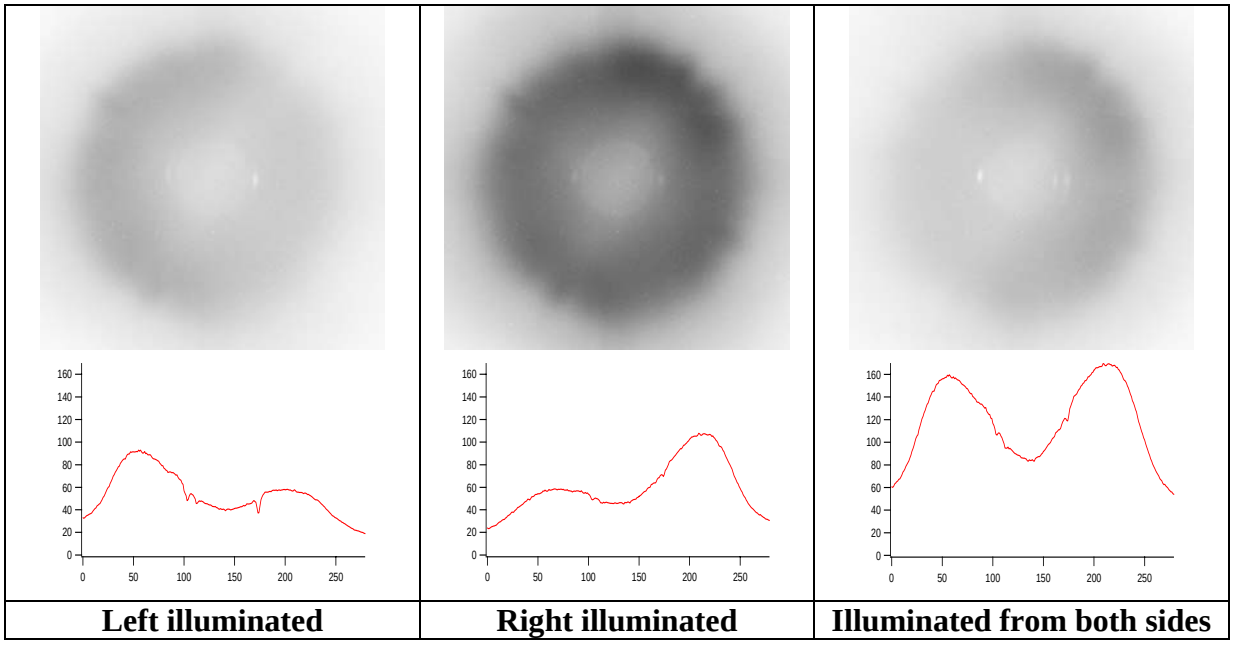

Figure 4.6. Results of laser sheet extinction test. Fueling rate is set at 15.6 mg/cycle.

4.2.2. Out-of-Plane Illumination

To measure the amount of fuel that was illuminated outside of the plane of interest, the following experiment was conducted. The experiment compared an ideal, unscattered laser sheet to a sheet that passed through a fuel spray. The difference between the two beams was then used to measure of out-of-plane illumination. To obtain images of the ideal sheet, the laser sheet passed through a fluorescent dye-filled cuvette placed in the laser optical access window. In both of these tests, the camera was set up directly above the laser optical access window, giving an overhead view of the vertical laser sheet. Figure 4.7 shows the ideal sheet, while Figure 4.8 shows the sheet passing through the fuel spray.

Figure 4.7. Overhead view of ideal laser sheet.

Figure 4.8. Overhead view of laser sheet scattered by fuel spray.

Intensity profiles along a vertical line were taken to quantify the differences between the two situations. Since the laser sheet was not scattered in the liquid filled cuvette, the beam was more concentrated and had a higher pixel count. Because of this, the profile was normalized to match the peak of the attenuated fuel spray sheet. Figure 4.9 compares the profiles of the scattered sheet, the fitted unscattered sheet, and the difference of the two sheets. From the graph, it was evident that out of plane illumination was significant in this experiment.

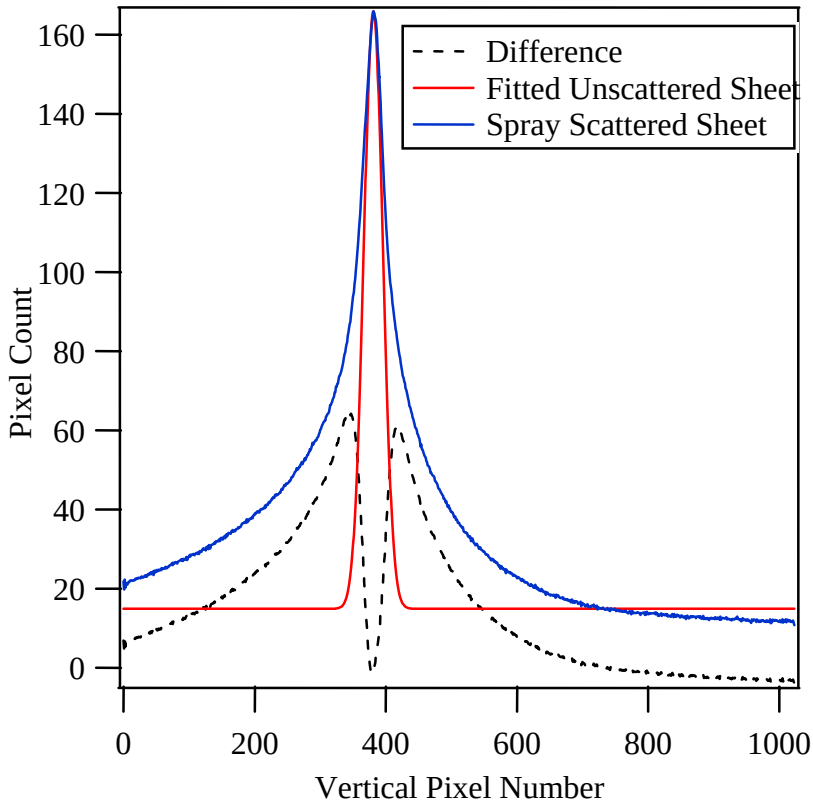

Figure 4.9. A comparison of laser sheet thickness profile passing through a cuvette and a fuel spray. The difference trace shows the amount of scattering in the fuel spray.

4.2.3. Blur Measurements

To measure the amount of blurring caused by secondary scattering, the following test was conducted. Images were taken with the bottom half of each sheet blocked. Three sets of data were captured: one set with the right-traveling sheet fully blocked and the bottom half of the left-traveling sheet blocked, one set with the left-traveling sheet fully blocked and the bottom half of the right-traveling sheet blocked, and one set with bottoms of both sheets blocked. As Figure 4.10 shows, fuel droplets in the bottom half of the spray were illuminated, which confirmed the influence of secondary scattering.

	Laser Sheet Profile	Spray Image	Vertical Line Profiles of Laser Sheet and Spray Image
Left		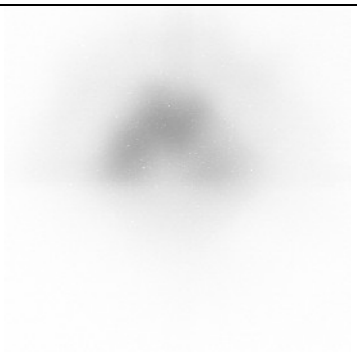	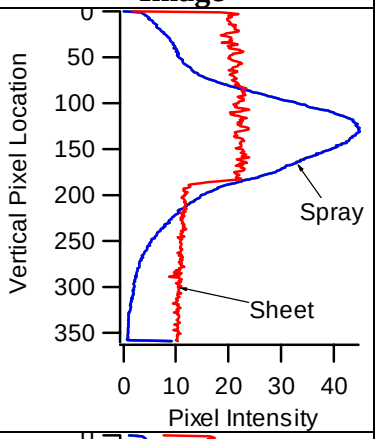
Right		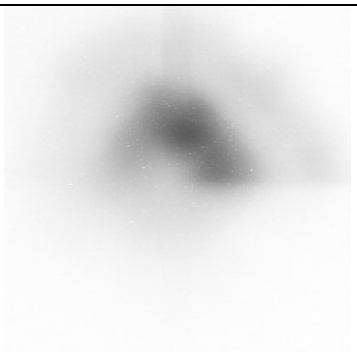	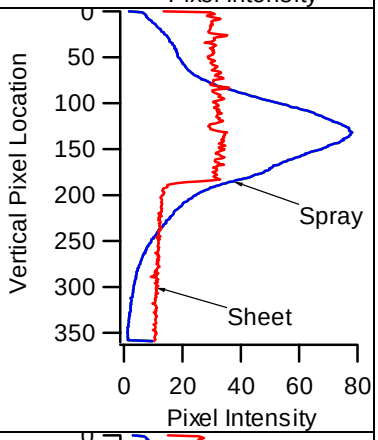
Both		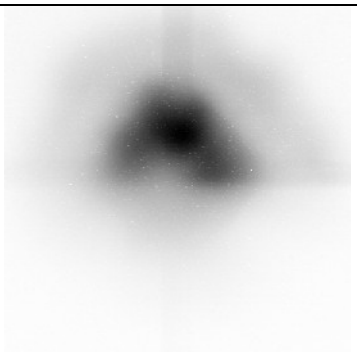	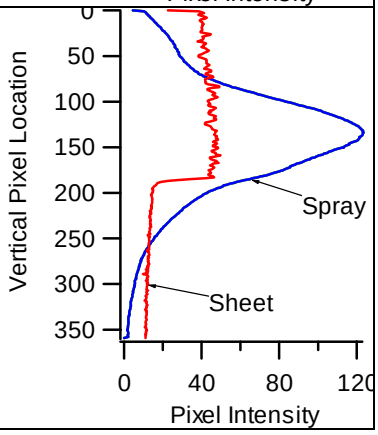

Figure 4.10. Laser sheet and spray images with the bottom half of the laser sheet blocked, showing the amount of scattering that occurred in the imaging plane. The difference between the sheet profile and the spray profiles are shown in the far right column.

4.3. Test condition selection

The process used to set the operating points is described in detail in the following sections.

4.3.1. Idle Data

The first set of operating parameters was extracted from available information about engine operation at idle conditions. The information was taken directly from the research project completed by Brian McGuire in the Engine Research Center at UW [19]. Table 4.4 shows the injector timing data that was the basis for the injector conditions used in this project.

SPEED (rpm):	700
SOA (CA BTDC):	44
EOA (CA BTDC):	28
F-A DELAY (ms):	4
TOT FUEL (mg/cycle):	5.2

Table 4.4. Injector parameters at idle.

In previous tests, it was determined that the injector frequency would be set to 500 rpm in four stroke mode to deter window fouling. Since the idle data was taken at 700 rpm, the parameters using crank angle units were adjusted to leave injection timing unchanged. The crank angle conversion from 700 rpm to 500 rpm for air injector duration is shown in Equation (4.6).

$$16CA@700rpm * \frac{500rpm}{700rpm} = 11.5CA@500rpm \qquad (4.6)$$

The majority of the data collected in this project used the settings shown in Table 4.5. Unfortunately, the file containing the engine operating data did not explicitly state the units

for the fuel-air delay. Because of this, most of the data was erroneously collected using a fuel air delay time of 4 CA (0.952 ms) instead of 4 ms. The consequences of this error are discussed in Section 5.4.

SPEED (rpm):	500
SOA (CAD BTDC):	13.5
EOA (CAD BTDC):	2
F-A DELAY (ms):	0.952
TOT FUEL (mg/cycle):	5.2

Table 4.5. Experimental injector parameters.

Engine operating data was also used to determine the chamber pressure for the pressurized case. When the air injector opened at 44 CAD BTDC, the cylinder pressure was at 377 kPa (40 psig). The pressure rises throughout the injector duration, but if a higher chamber pressure was used, the air velocity in the apparatus would decrease, which would increase window fouling rates. Because of this, the pressure at the start of injection was the pressure chosen for the pressurized case.

4.3.2. Capture Delay Testing.

With the injection timing parameters set, the next logical step was to set up a parametric test to study different spray stages. Two sets of data were compiled: one detailing the spray at atmospheric pressure (Figure 4.11), and one at 377 kPa atmospheric (Figure 4.12). These figures show the average of 50 raw images taken at each time delay, with 100 μs intervals separating each set of data. The range in the atmospheric case was limited by signal strength, whereas in the pressurized case, data collection ceased when the spray geometry appeared to stop changing significantly. From these images, five data points were selected. For atmospheric conditions, data points were selected at 2.5 and 2.7 ms. For the pressurized conditions, data points were selected at 3.1, 3.6, and 4.1 ms. These data points were chosen because they seemed to characterize the spray efficiently.

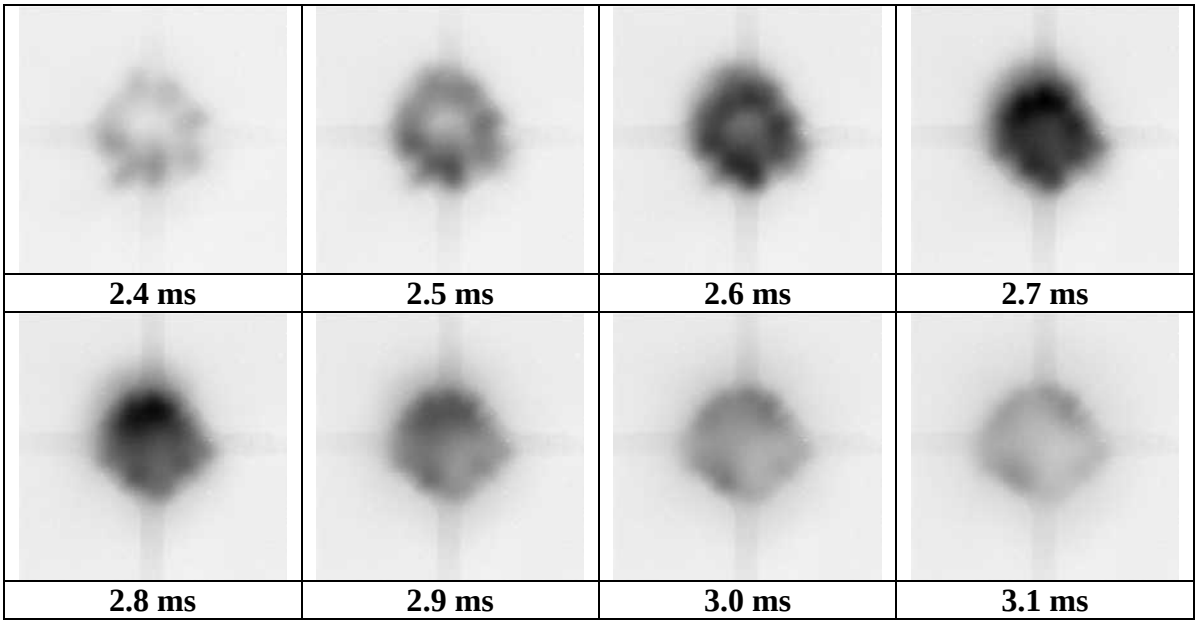

Figure 4.11. Unpressurized spray images of reference injector #5 at different capture delay times.

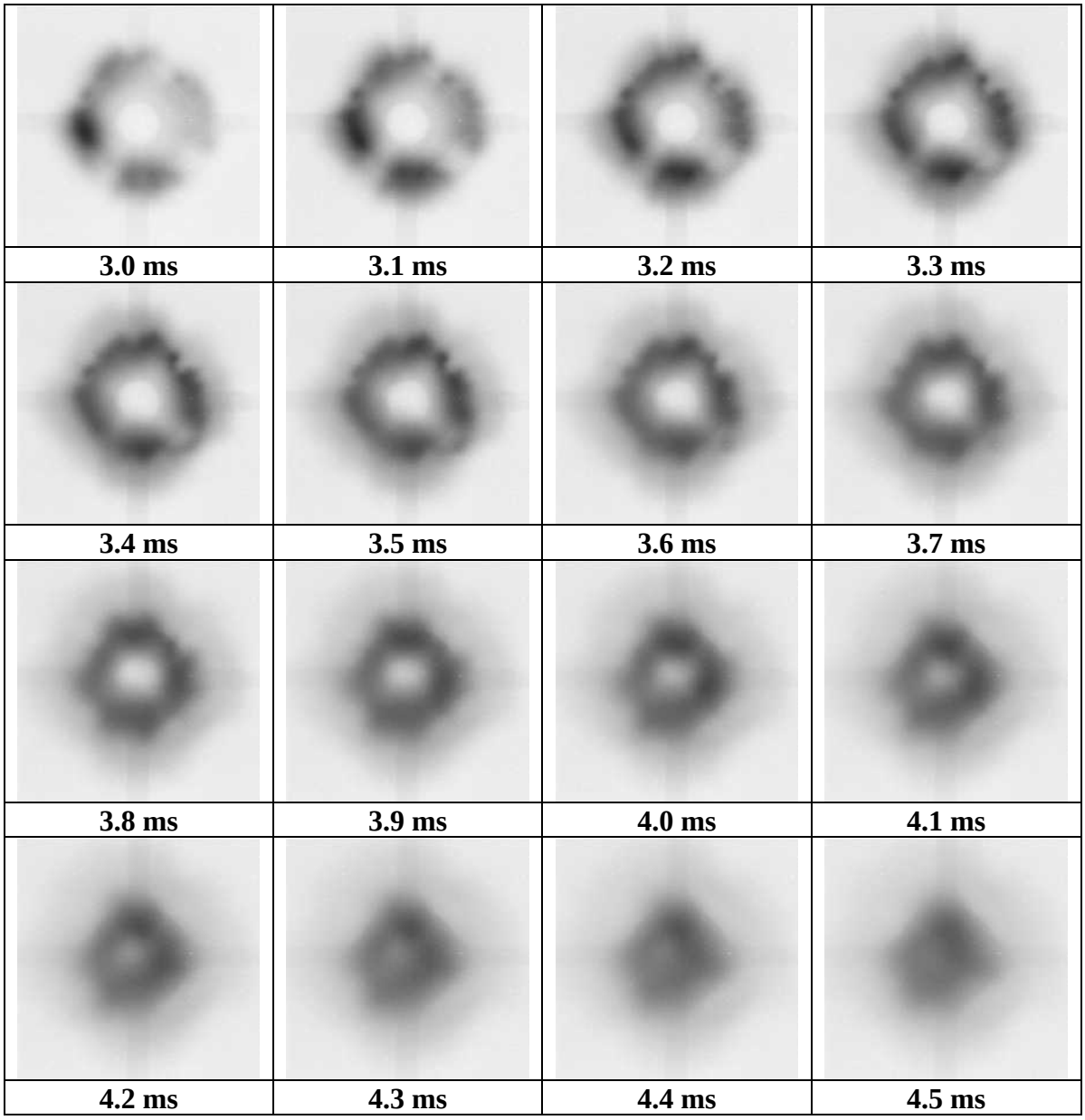

Figure 4.12. Pressurized spray images of reference injector #5 at different capture delay times.

4.3.3. Signal Attenuation Test

With the data points set, a test was conducted to estimate the amount of signal attenuation caused by secondary scattering along the light collection path at the selected points. To test for signal attenuation, a nail was bonded to the horizontal cross hair support

of the porous metal holder. The intersection of the nail tip and the laser sheet created a point of light from the camera's perspective. The unattenuated signal was measured with the injector off and with the vessel air flowing through the chamber, which was pressurized to 377 kPa atmospheric. The attenuated signals were measured with the injector turned on at seven different camera delay times.

Light can be attenuated by the fuel from the spray being imaged, and from the fuel still residing in the vessel from previous sprays. The former was investigated by measuring scattering from the nail at camera delay times from 3.1 ms to 5.6 ms. The latter was measured by taking images just before injection, leaving the residual fuel in the vessel as the only cause of signal attenuation. For each of the seven data points, data was taken with the injector off to get the unattenuated signal, and the injector on to get the attenuated signal. The average of 100 raw images at each point was compared. The mean intensity of the pixels inside the ROI of the nail point was used to measure the level of signal attenuation. Figure 4.13 shows the averaged image for the 3.1 ms data point, with the nail tip region in the black box.

The two signals for each point are shown in Table 4.6, along with the ratio of the attenuated to the unattenuated signal. The table is sorted by this ratio in descending order. A high ratio corresponds to a low amount of signal attenuation. The results of the table show the general trend of higher attenuation as the camera delay is increased. So, to minimize the effect of attenuation, it was desirable to collect data in the earlier stages of the spray. While the order of the four points with the lowest attenuation levels was not expected, those values were in close proximity of one another, and could be within the error range. It should be

noted that the data point at 0 ms was taken twice to check the repeatability of the measurement.

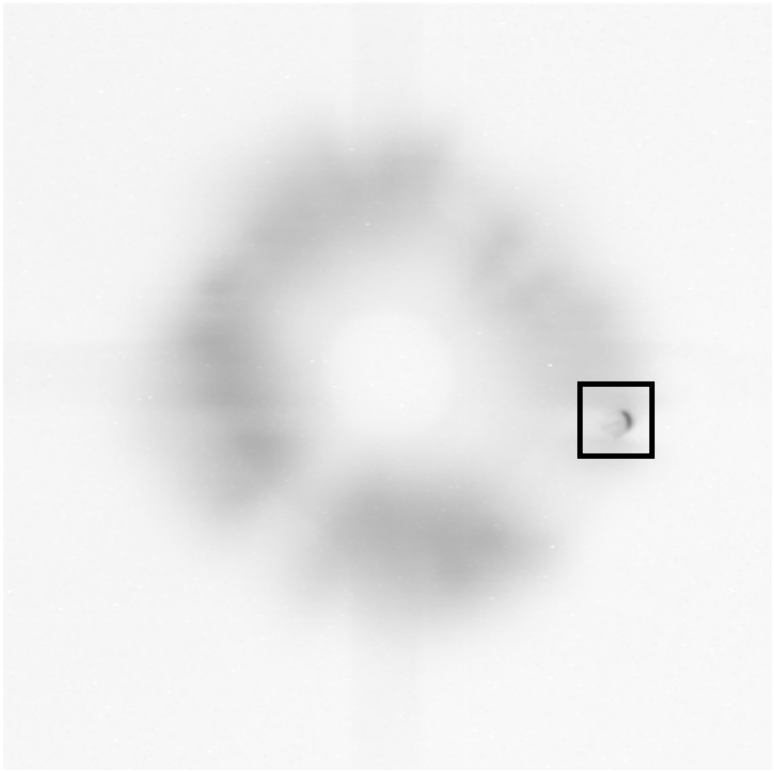

Figure 4.13. Averaged image of attenuation test at a 3.1 ms delay. Nail location is in the center of the black box.

Camera delay (ms from SOA)	Mean (no fuel case)	Mean (fueled case)	Ratio
3.6	17606.92	17021.54	0.966753
3.1	19440.63	18763.3	0.965159
0 before	18647.72	16169.78	0.867118
0 after	18180.17	15366.83	0.845252
4.1	19162.68	13882.11	0.724435
4.6	19258.8	12276.68	0.637458
5.1	19970.29	11157.25	0.558692
5.6	19323.18	10328.36	0.534506

Table 4.6. Results of signal attenuation test.

4.3.4. Flat Field Correction

It should be noted that none of the cross sectional spray images shown in this thesis have been flat field corrected. Flat field correction techniques are used to correct for non-uniform laser sheet intensities. When the laser beam leaves the laser, it has cross section that is approximately Gaussian in shape. Imperfections in the optics cause deviation from this distribution, so when the beam is formed into a sheet, it looks like the image in Figure 4.14. The sheet profile was obtained by capturing images of the sheet passing through a dye filled cuvette. Variations in the sheet intensity translate to variations in spray image intensity, and because Mie scattering correlates fuel density with pixel intensity, uneven illumination needs to be accounted for. To correct for uneven illumination, parts of the image that are in areas of low laser power are amplified, and parts that have high laser intensity are attenuated. When flat field correction was applied to spray images used for this research, the image quality was reduced, as Figure 4.15 shows. Because the laser light was scattered by the fuel droplets in the imaging plane, the sheet profile captured before data collection was not an accurate indication of the actual spray illumination. That was the reason for not using flat field correction for the images in this project.

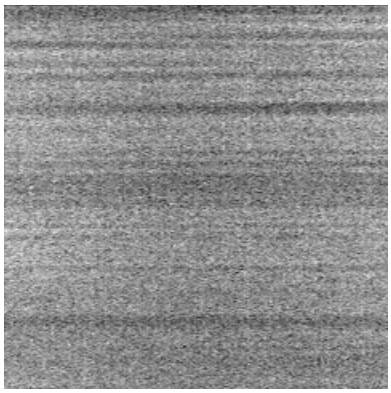

Figure 4.14. Laser sheet profile, captured by passing the sheet through a dye-filled cuvette.

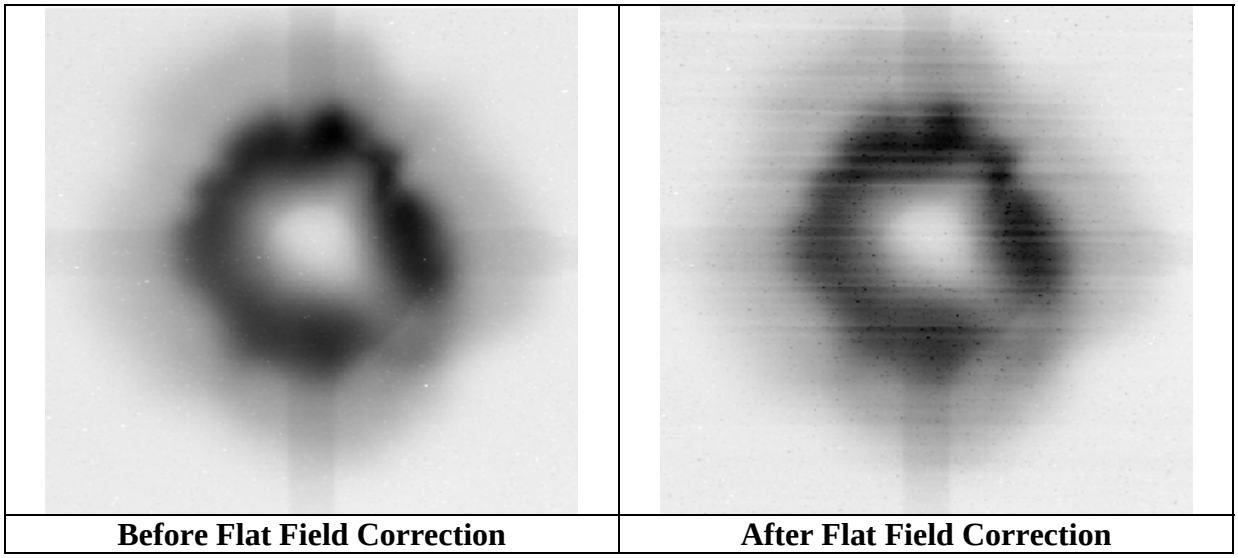

Before Flat Field Correction	After Flat Field Correction

Figure 4.15. A demonstration of the negative effects of flat field correction.

4.3.5. Strobe Profile Test

To verify the results of the signal attenuation test, a strobe profile test was conducted to observe the amount of fuel between the laser sheet and the camera position to be used for testing. In this test a strobe light was used to back illuminate the entire spray. A camera was positioned on the side of the spray, where it took profile images of the spray. Images were taken at nine different points, spaced 500 μs apart from 3.1 ms to 7.1 ms, covering the full range of the spray period. The images are shown in Figure 4.16, with the injector firing from right to left. The black vertical lines shown in the pictures represent where the laser sheet normally passed through the spray.

For the actual injector testing, the camera position was downstream of the spray, or to the left of the images shown. Therefore any fuel spray that was located on the left side of the black vertical line was spray that could contribute to the blurring or attenuation of signals from the imaging plane. As is shown in these pictures, longer camera delays allow more

spray to move to the left of the imagine plane, causing more secondary scattering. This is in agreement with the trends shown in the signal attenuation test. These two tests show that taking data at earlier stages of injection should minimize the adverse effects of secondary scattering.

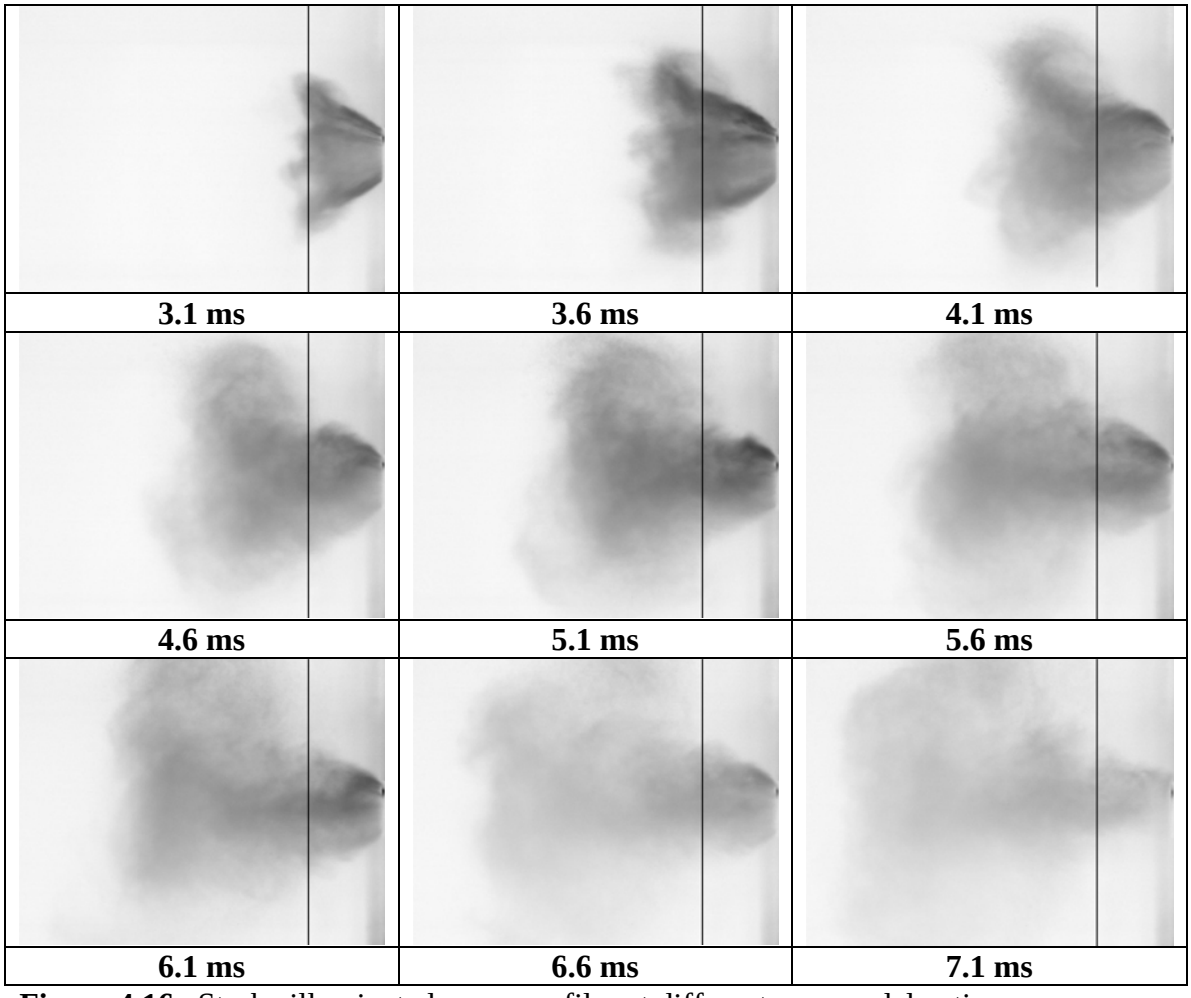

Figure 4.16. Strobe illuminated spray profiles at different camera delay times.

5.0. Results

This chapter details the results of injector testing. The testing procedures are described first, followed by a visual and statistical presentation of the data. The section concludes with a discussion of the effect that the fuel-air delay had on the results.

5.1. Overview of Testing and Image Processing

5.1.1. Testing Procedure

Mercury Marine supplied 21 injectors to be analyzed in the test apparatus. 6 of these injectors were labeled as "good" injectors, which have been used by Mercury as reference injectors for engine troubleshooting. These injectors have been named R1, R2 … R6 for analysis. Of the remaining 15 injectors, numbered from 1 to 15, two were identified by Mercury to be the worst performing injectors, producing the most misfires of the batch in engine tests. The worst injector (#6) logged 10 misfires and the second worst (#1) logged 3. For each day of testing, the injector tested at the start of the day was also tested at the end of the day, which ensured that test conditions did not vary significantly through the day. This also provided a measure of the consistency of the test results.

5.1.2. Image Capture Technique

Each injector was tested using the following procedure. An air injector was installed between the injector housing in the apparatus and the fuel rail. To limit variability, both optical windows were cleaned before each test. To measure the laser sheet profile for flat field calculations, 100 images were obtained with the laser sheet passing through a dye filled cuvette, which was placed in the optical section of the vessel. After the cuvette was

removed, the vessel position was adjusted to create a distance of 12.1 mm between the laser sheet and the injector tip, corresponding to the axial distance between the air injector and the spark plug in the production engine. Using the method described in Section 4.1.2, data at five different image capture delay times and at two different vessel pressures were obtained. Data at ambient vessel pressure were taken using image capture delay times of 2.5 and 2.7 ms. The pressurized case (377 kPa absolute) used image capture delay times of 3.1, 3.6, and 4.1 ms. At each data point, 50 "before" background images were obtained, followed by 100 spray images and 50 "after" background images. Background images were captured with the laser pulsed and the injectors turned off. After the injector data were collected, the cuvette was reinstalled, and 100 more laser profile images were obtained. These laser profile images were obtained to measure the effect of window fouling on the laser profile. As explained in Section 4.3.4, none of the flat field images ultimately were used for image processing.

5.1.3 Image Processing Method

A brief overview of the image processing method is detailed in the following section. A more detailed explanation is included in Appendix E. Initial processing produced 100 background-subtracted images at the 5 conditions obtained for each injector. Because the camera had a tendency to move a pixel or two from one injector test to the next, it was necessary to center each set of images, so that the pixel locations of each injector matched. The centering process is also described in Appendix E. Once the 100 images were centered, they were analyzed using the pattern factor function in Insight.

The Insight pattern factor function allowed a spray image to be divided into a specified number of wedges or rings, as shown in Figure 5.1. The sections created by the pattern factor function were used to statistically analyze the symmetry of a spray. This was

done using the mean pattern factor (MPF) or the area pattern factor (APF). The MPF provides an estimate of spray asymmetry based on the average pixel value within a sector; the APF is a function of the number of pixels that exceed a user-defined threshold level and is, as the name suggests, related to the area covered by the spray in the individual sectors. The formulas for the MPF and APF are listed below,

$$MPF = \frac{Max - Min}{Mean} \qquad (5.1)$$

$$APF = \frac{Max\# - Min\#}{Mean\#} \qquad (5.2)$$

where *Max* is equal to the highest sector-average pixel value, *Min* is equal to the lowest sector-average pixel value, and *Mean* is the mean of all the pixel values in the sectors. In the APF formula, *Max#*, *Min#*, and *Mean#* refer to the maximum, minimum and mean values of the number of covered pixels observed in each of the N sectors. Appendix E works out an APF and a MPF problem for clarity.

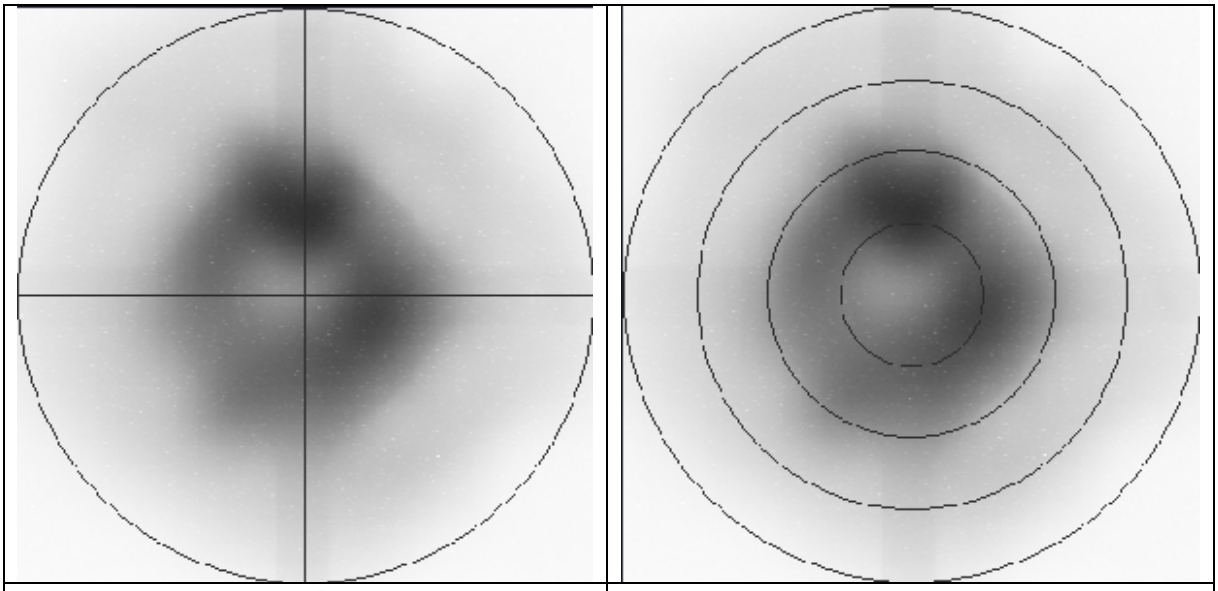

Figure 5.1. Visual representation of Insight pattern factor analysis tool.

The background threshold is user selectable, and determines the minimum pixel level that is included in either of the pattern factor calculations. If the background threshold were set to 0, every pixel within the image sectors would be included. However, it is desirable to set the background threshold to a higher level to reduce the influence of noise in the calculations.

Once the APF and MPF for each image were obtained, the mean and standard deviation for each data set was calculated. The mean values of APF and MPF for each injector were then compared. The uncertainty in the mean values was obtained using the following equation:

$$U = \frac{1.96\sigma}{\sqrt{n}} \qquad (5.3)$$

where U is the uncertainty in the mean, σ is the standard deviation of the pattern factors, and n is the number of images in the set. This equation corresponds to a 95% confidence interval for a normal distribution.

The pattern factor calculations provided a measure of symmetry, so a symmetrical spray would yield low values, and an asymmetrical spray would yield high values.

5.2. Visual Analysis of Injector Data

The first step after data analysis was to visually inspect the results. If injector performance could be determined through visual inspection of the spray images, injectors could be characterized quickly and easily. The following section compares some averaged images as well as some consecutive individual images to assess the feasibility of judging injector performance by visual inspection.

5.2.1. Comparison of an Injector Subset

Figure 5.2 compares the average of the background-subtracted images of 5 injectors at the five test points in this experiment. These five injectors were selected from the group of 21 based on the APF data, which is presented in Section 5.3.1. Figure 5.2 has been sorted in ascending order by the average APF at a capture delay of 4.1 ms. The most symmetrical injector, according to the average APF, is at the top (injector R5), and the least symmetrical injector is at the bottom (#6). These images have been scaled to the same values, with darker regions corresponding to higher intensity levels.

It is evident from Figure 5.2 that images captured from injectors 13, 4, and 1 were not significantly different from each other. Because intensity can vary depending on conditions, the higher intensity seen in the images for injector #1 was not significant. The major differences seen in these data sets were in injector R5 and injector #6. Injector R5 showed a much more developed hollow cone structure in the pressurized cases than the other injectors, and produced a larger overall spray diameter. Injector #6 was easily the worst performing injector in the test, producing very poor atomization and severely asymmetrical spray images. The spray patterns at 3.1 ms are most likely linked to the four-hole structure inside the air-

assist injector, shown in Figure 5.3. Appendix F contains the remaining data for the blind injectors.

	Atmospheric Pressure		377 kPa		
	2.5 ms	**2.7 ms**	**3.1 ms**	**3.6 ms**	**4.1 ms**
R5	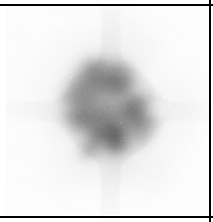	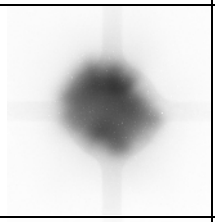	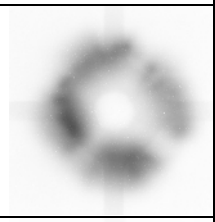	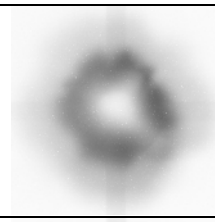	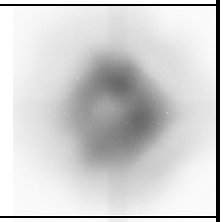
#13	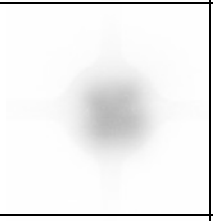	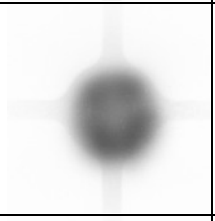	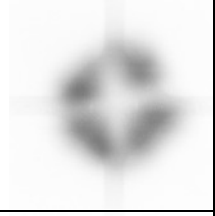	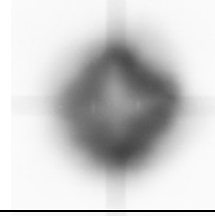	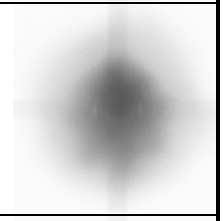
#4	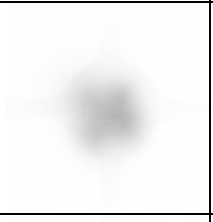	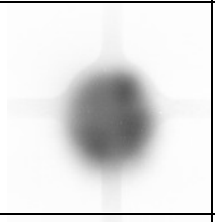	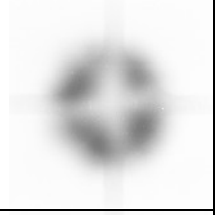	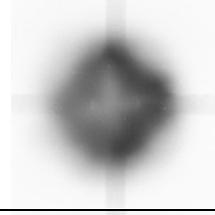	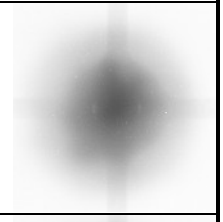
#1	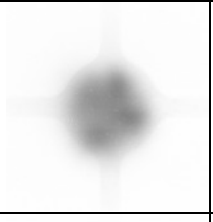	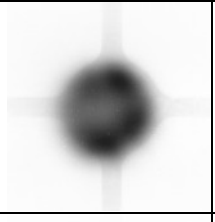	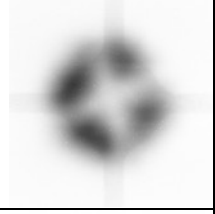	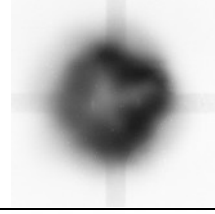	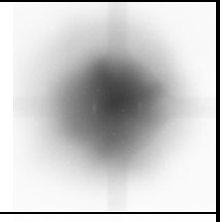
#6	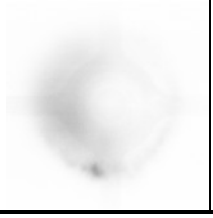	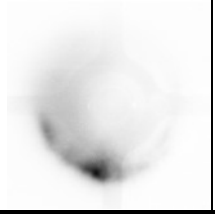			

Figure 5.2. Averaged image comparison of a representative set of fuel injectors.

Figure 5.3. Inner structure of air-assisted injector. Two of the four holes are visible.

5.2.2. Comparison of Reference Injectors

Figure 5.4 shows the data from the six reference injectors to highlight the characteristics of a good injector. These injectors are placed in Figure 5.4 in ascending order by the average APF at a capture delay of 4.1 ms. When analyzing these images, it was apparent that they all produced a well defined hollow cone structure. However, there still was some variability from injector to injector, despite their status as reference injectors. Some injectors appeared to be more symmetrical than others at 4.1 ms. For instance injector R4 appeared to be very symmetrical, while injector R3 appeared to have higher intensities on the right side of the spray.

The differences between the reference injectors seen in Figure 5.4 are on the order of the differences between the blind injectors in Figure 5.2. Visual inspection did allow identification of the worst injector (#6), but did not provide sufficient discrimination of the other injectors.

	Atmospheric Pressure		377 kPa		
	2.5 ms	**2.7 ms**	**3.1 ms**	**3.6 ms**	**4.1 ms**
R5	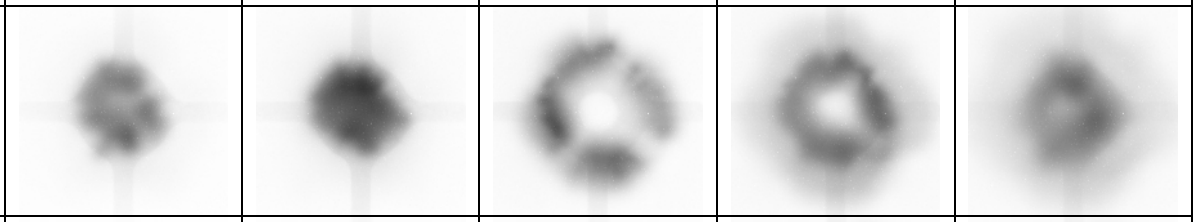				
R1	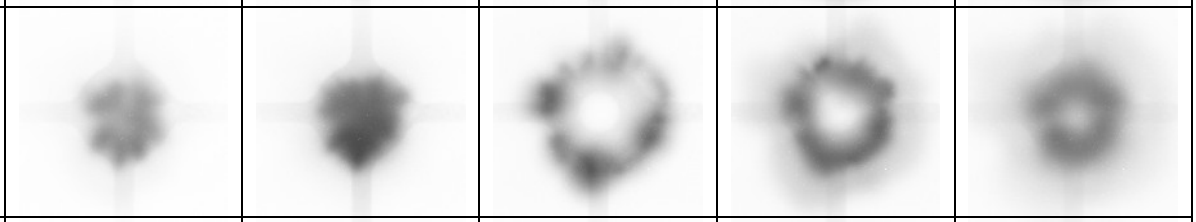				
R4	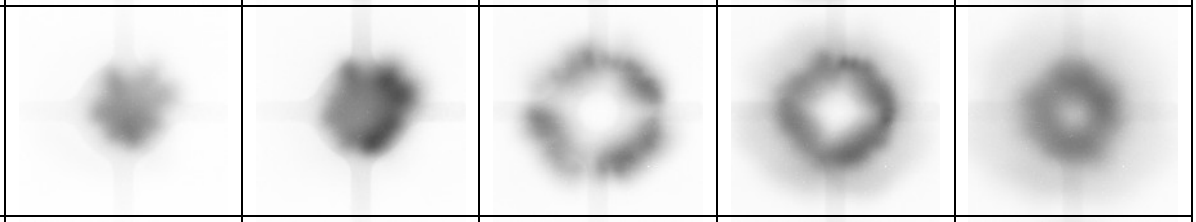				
R6	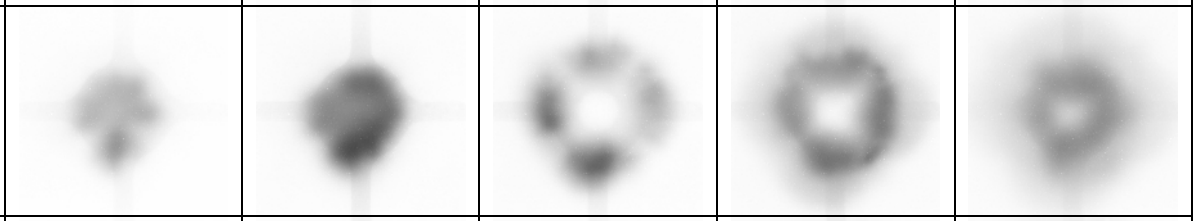				
R2	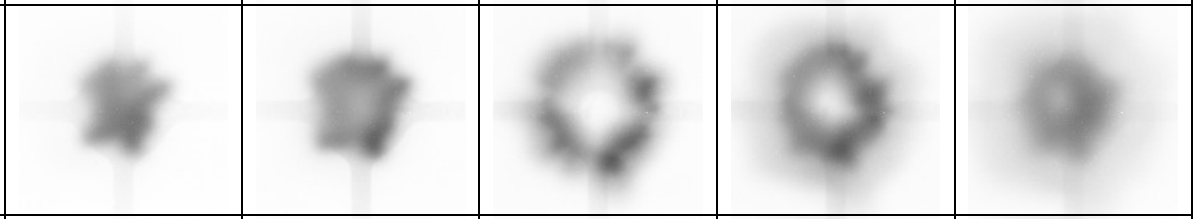				
R3	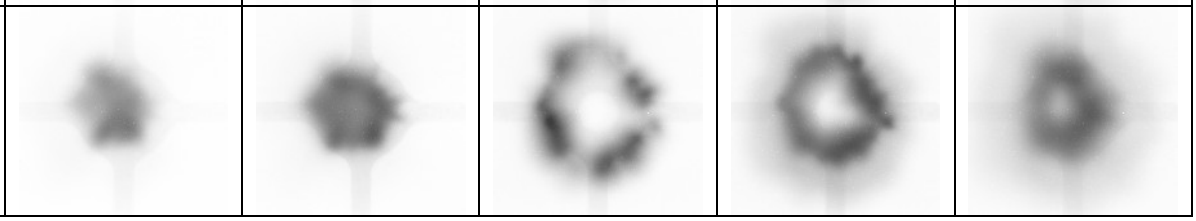				

Figure 5.4. Comparison of the averaged images of the 6 reference injectors.

5.2.3. Shot-to-Shot Variability

A crucial parameter of injector performance is consistency. To observe the shot-to-shot variability of a good and bad injector, figures were created containing 10 consecutive images captured from each injector. Figure 5.5 displays images from injector R5, Figure 5.6 shows images from injector #1, and Figure 5.7 shows injector #6 images. The images in all three figures were taken at a capture delay time of 4.1 ms and a vessel pressure of 377 kPa absolute. All three sets of images display noticeable variation, so it was pretty difficult to compare their overall variability through visual inspection.

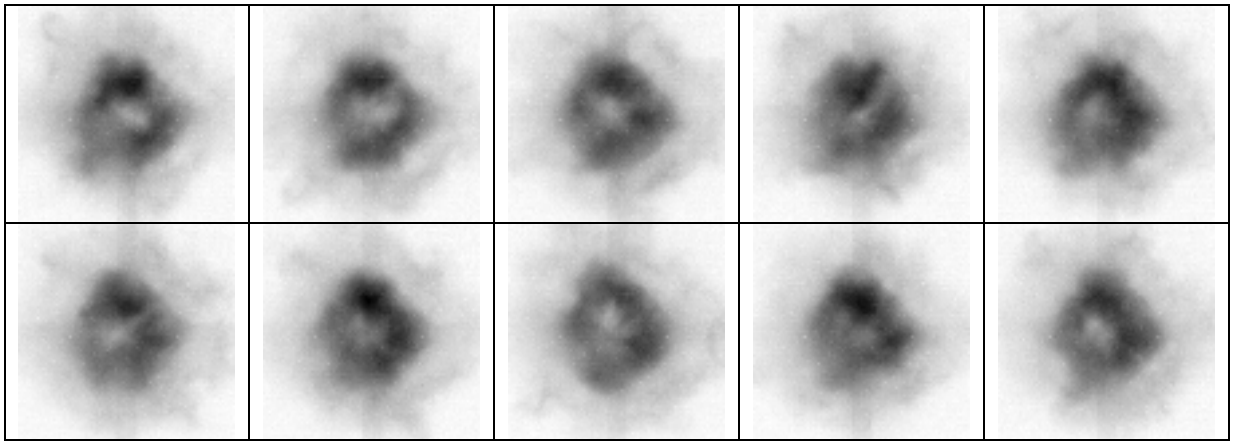

Figure 5.5. Shot-to-shot variability of injector R5 at 4.1 ms capture delay.

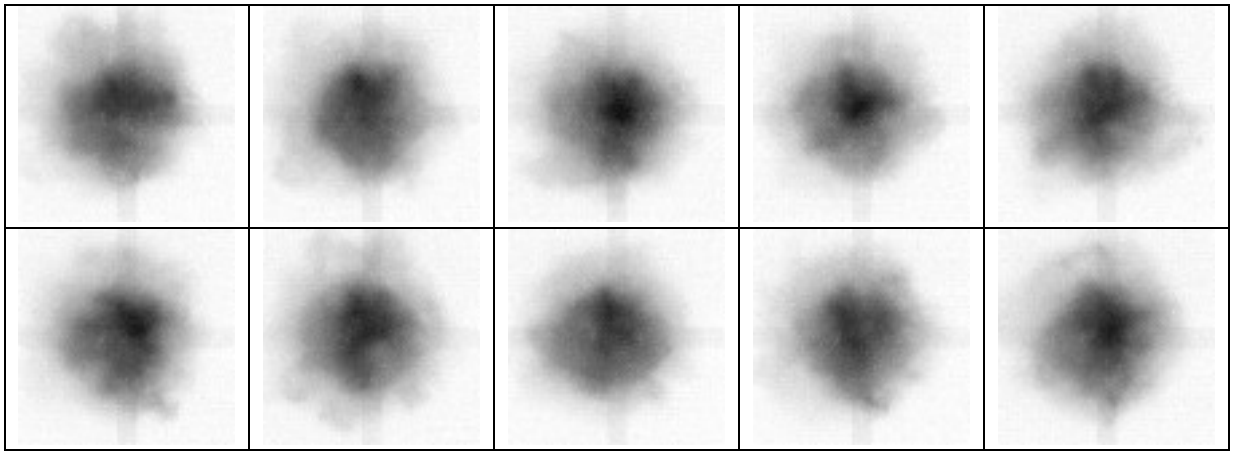

Figure 5.6. Shot-to-shot variability of injector #1 at 4.1 ms capture delay.

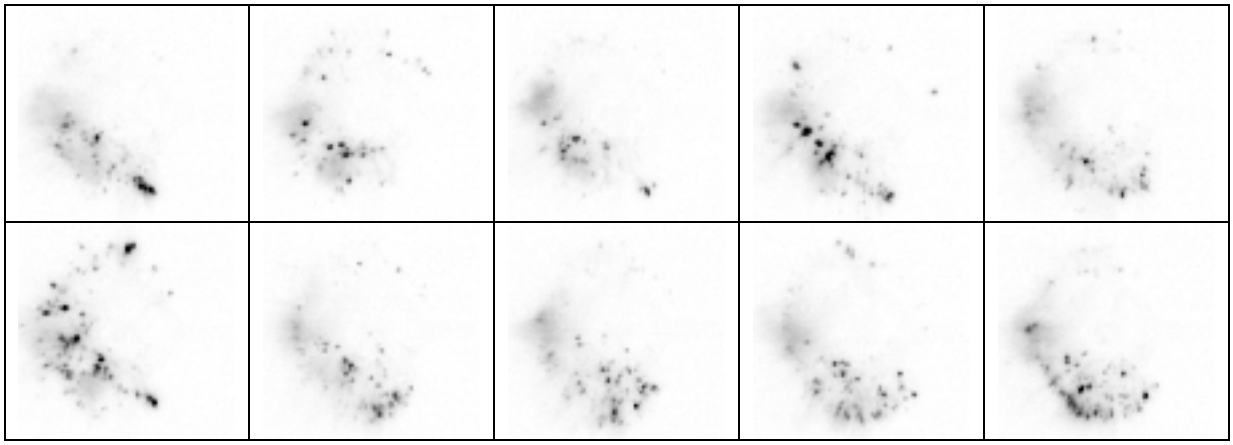

Figure 5.7. Shot-to-shot variability of injector #6 at 4.1 ms capture delay.

To further evaluate shot-to-shot variability, images of the standard deviation of each pixel from 100 background-subtracted, centered images for each injector at a capture delay time of 4.1 ms and at 377 kPa absolute pressure were investigated. A subset of the injector standard deviation images are shown in Figure 5.8. Based on the maximum and average pixel values for these images, and from visual inspection, injector #6 was the only injector that showed major differences from the group. The maximum pixel value for the injectors ranged from 2200 to 3800 counts, with the 4 runs for injector R5 ranging from 2800 to 3800 counts. Injector #6 was not included in that range; it had a max pixel count of 16,500. The average pixel value ranged from 780 to 1040 pixel counts, with the injector R5 ranging from 850 to 1030. Injector #6 was an outlier, with an average pixel count of 1900. The port and starboard spark plugs are located where the lines meet the circle in the image. These points were added to the images in order to show the deviation near the spark plug locations.

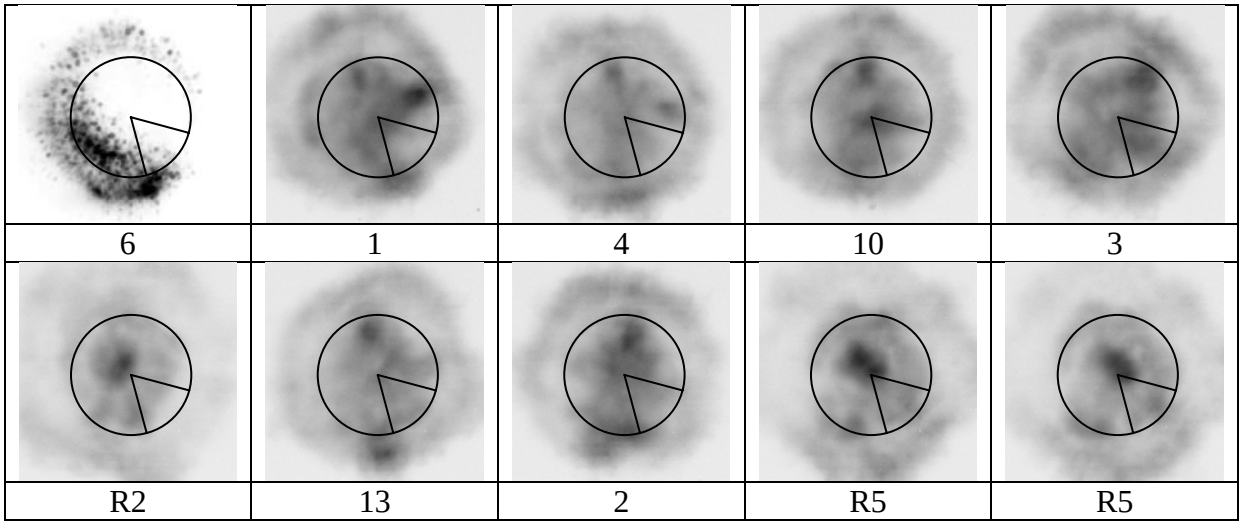

Figure 5.8. Images of the standard deviation of each pixel for 10 injector runs. The standard deviation was calculated using 100 background-subtracted, centered images taken at a capture delay time of 4.1 ms and a pressure of 377 kPa absolute.

5.3. Statistical Analysis

Since visual inspection of the data did not sufficiently characterize the differences between injectors, a statistical analysis was conducted to more objectively assess injector performance. The data were analyzed using the pattern factor function in the Insight 3G image processing software. The following section presents the pattern factor results, and discusses some issues involved with using this analysis method.

5.3.1. Pattern Factor Results

To compare the symmetry of the fuel spray images from each injector, the pattern factor results were compiled for each injector at a specified capture delay time. Because the software could divide the images into wedges or rings, and calculate both mean and area pattern factor data, 4 different sets of data could be analyzed for a given set of injectors. The goal was to find a combination of parameters that would group the good injectors in one range, the bad injectors in another range, and the blind injectors in a region between the two extremes. After testing the 4 combinations, it was evident that dividing the injector images into wedges and comparing the APFs was the only method that produced the desired separation between the good and bad injectors. Appendix G contains MPF graphs and Appendix H contains graphs using rings instead of wedges.

Figure 5.9 shows the average of the individual APF values for the 100 images taken for each injector, along with the uncertainty in this mean value as described in Section 5.1.3. The graphs were obtained using 12 wedge sections, with the background threshold set to a level of 1500 pixels, which corresponded to an average of 5% of the max pixel count in the images. Twelve wedges were used because that setting allowed the two spark plug locations to be centered in their own individual section. Figure 5.10 illustrates this rationale.

The vertical position of the injectors on the graphs in Figure 5.9 was modified to prevent overlap in congested areas, making the graph easier to read. As is shown in Figure 5.9, the data showing the best separation was at 4.1 ms, which was closely followed by the data collected 3.6 ms (both points were taken with chamber pressures at 377 kPa absolute). At these data points, most of the reference injectors resided on the left side of the graph, meaning they had low APF values and good symmetry. Injectors R2 and R3 were the exception to this trend, having APFs near the data set mean.

This could be mean that the method did not sufficiently group the reference injectors together, or it could be interpreted as the dividing line between good and bad injectors. Assuming the latter assumption was true, it appeared that injector #13, #8, and #2 were good, injector #11, #10, #14, and #4 were bad, and the rest were on the borderline.

The graphs also show that the data taken at atmospheric pressure (Part d and e in Figure 5.9) did not produce the desired separation between the reference injectors and the known bad injectors. However, as is discussed in Section 5.4, increasing the fuel-air delay time could produce better results.

It should be noted that the values for injector #6 were outliers and were listed as annotations in the graphs to allow better axis scaling. Also, there are multiple instances of the same injector in each graph. This is because injector #3 and #15 were tested twice to verify the consistency of test conditions and injector R5 was tested 4 times – twice with the numbered injectors and twice with the reference injectors. For the case of 4.1 ms and 377 kPa, the repeatability of the tests was very good, especially for R5 and #3. Repeatability worsened as capture delay time decreased, especially in the unpressurized cases.

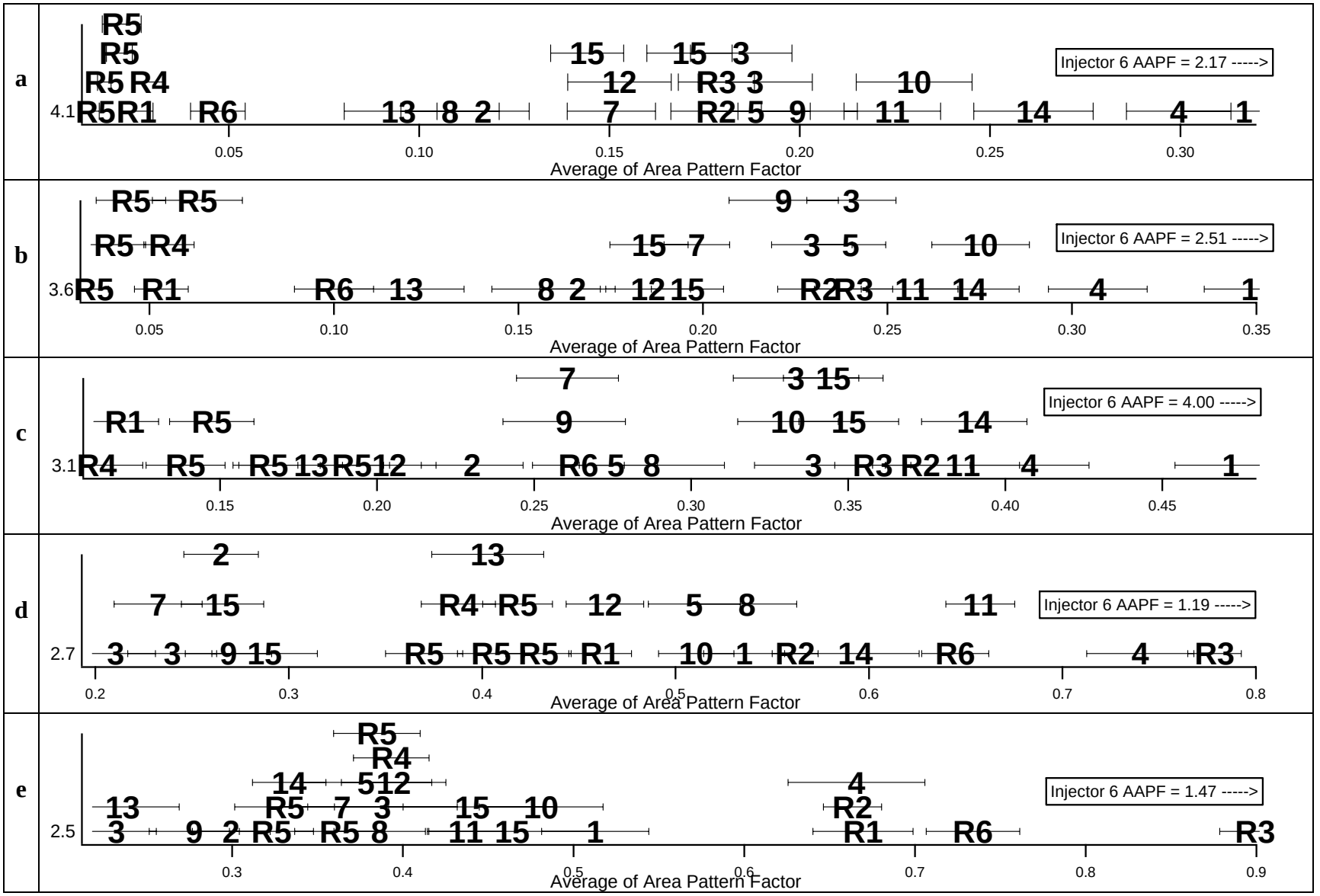

Figure 5.9. Pattern factor results at the five different capture delay times and two different pressures: a) 4.1 ms, 377 kPa; b) 3.6 ms, 377 kPa; c) 3.1 ms, 377 kPa; d) 2.7 ms, 101.4 kPa; e) 2.5 ms, 101.4 kPa. All pressures are absolute. 12 wedges, 1500 BT

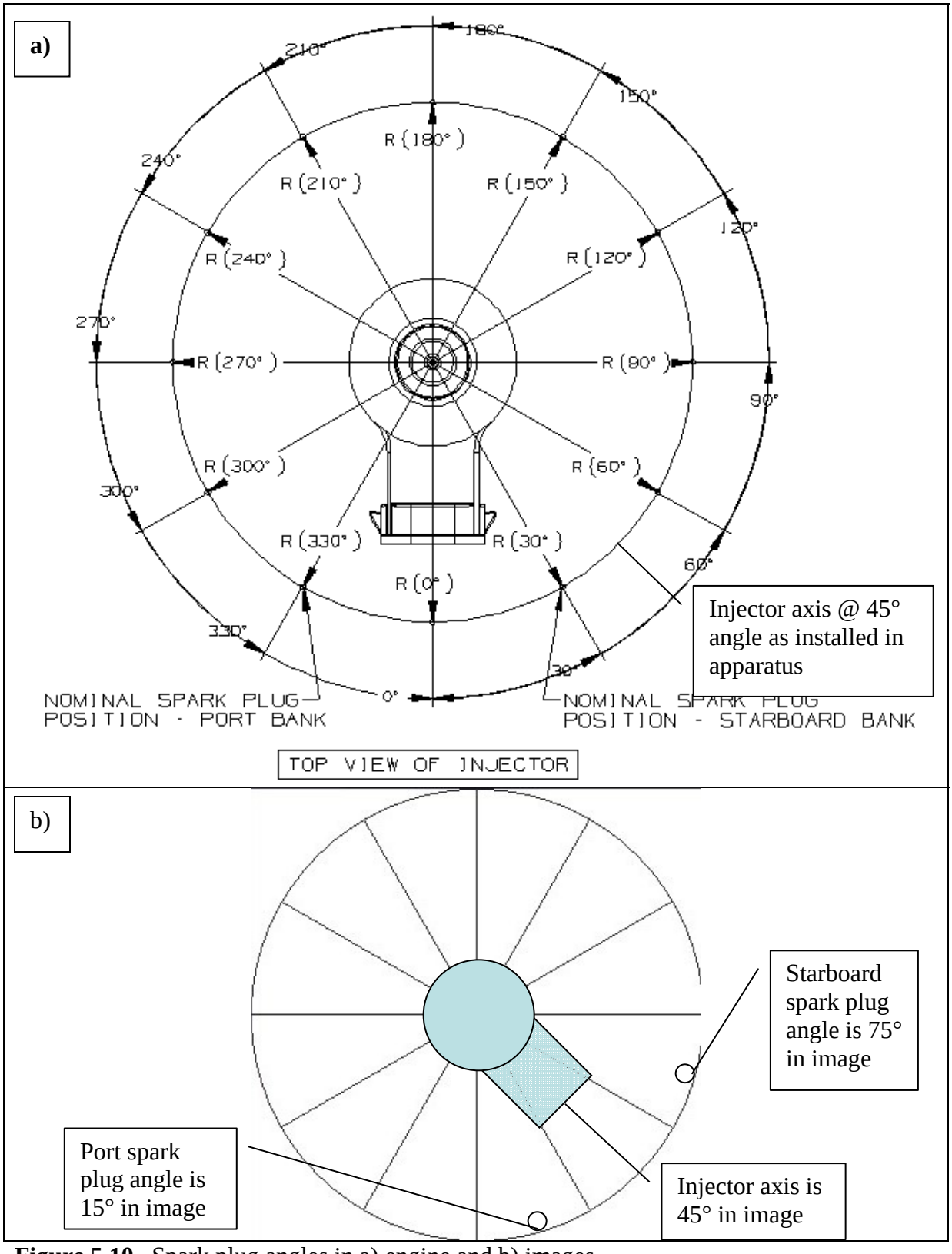

Figure 5.10. Spark plug angles in a) engine and b) images.

5.3.2. Pattern Factor Analysis Issues

While the APF results at 4.1 ms and 377 kPa absolute were encouraging, it is important to note that the method was sensitive to parameter changes. Table 5.1 shows the impact that parameter changes had on the APF values of the injectors at the capture delay time of 4.1 ms. The parameters that were altered in the figure were the background threshold (BT), the method for finding the APF, and the number of wedges used. Column A set the BT to 1500 pixels, used 12 wedges, found the APF of each individual image and then used the average of the 100 APFs. Column B used the same BT and wedge number as Column A, but found the APF of the averaged image of each injector. Column C used the same BT as Columns A and B, and found the APF of the averaged image of each injector, but used 10 wedges instead of 12. Column D was exactly the same as Column B, but set the BT to 2000 pixels.

Column A & B produced slightly different results because the APF of the averaged image is not equal to the average of 100 individual APF values. This occurred because the APF calculation does not take into account which sector the max and min APF values occur. So two images could be quite asymmetric, yielding high individual APFs, but the average of the two images could be more symmetric if the max sector in the first image were the min sector in the second image. However, considerably more time and effort is required to find the APF of each individual image, so if speed is more important than accuracy, taking the APF of the averaged image yields similar results with much less time. It should be noted that using this faster method does not allow the standard deviation of the APF to be calculated, which is important for the uncertainty analysis.

Small changes in the parameters caused some changes in the APF values for many injectors. As the boldface values in Table 5.1 show, there were many injectors that experienced changes in APF values that exceeded the range of uncertainty. In Columns B and C, most of the changes occurred in the injectors with smaller APF values. So, taking the pattern factor of an averaged image rather than taking the average of individual pattern factors caused an increase in APF value. In Column D, 15 out of the 19 injector runs experienced a significant decrease in APF values. Since increasing the background threshold reduces the number of pixels that are used in the APF calculation, the denominator (*Mean#*) in Equation (5.2) decreased. For APF values to decrease, the difference between the *Max#* and the *Min#*, had to decrease more than the *Mean#*. The assumption made was that the major effect of the increase in the background threshold was a decrease in the maximum number of pixels covered by the spray (*Max#*).

The order of injectors, when ranked by APF, also was slightly affected by changes in the parameters as shown in Table 5.2. The general trends were the same throughout the tests; injectors that started in one region of the table stayed in that region despite parameter changes. However, there was an abundance of small movements by the injectors positioned in the middle of the table. For example, injectors 5 & 7 moved to a different location with each parameter change. Because of this shuffling, a definitive injector ranking was not attempted.

# of Wedges Method of APF Calculation	Column A 12 Average of 100 APFs	Column B 12 APF of Averaged Image		Column C 10 APF of Averaged Image		Column D 12 APF of Averaged Image		Column E 12 Average of 100 APFs
Background Threshold	**1500**	**1500**		**1500**		2000		**1500**
Injector #	**AAPF**	**AAPF**	**A-B**	**AAPF**	**A-C**	**AAPF**	**A-D**	**Uncertainty +/-**
Ref 5	0.015	0.012	**0.003**	0.013	**0.010**	0.014	0.001	0.0010
Ref 5	0.017	0.012	**0.005**	0.020	**0.004**	0.020	**-0.003**	0.0018
13	0.095	0.052	**0.043**	0.005	**0.075**	0.066	**0.029**	0.0034
8	0.108	0.081	**0.027**	0.076	**0.032**	0.103	0.005	0.0051
2	0.117	0.101	**0.016**	0.087	**0.030**	0.124	**-0.007**	0.0043
15	0.144	0.146	-0.002	0.126	**0.028**	0.154	**-0.010**	0.0038
7	0.151	0.149	0.002	0.141	**0.025**	0.221	**-0.008**	0.0072
12	0.153	0.149	0.004	0.116	0.013	0.158	**-0.042**	0.0143
15	0.171	0.154	**0.017**	0.140	**0.030**	0.195	**-0.039**	0.0129
3	0.185	0.176	0.009	0.185	0.000	0.258	**-0.027**	0.0121
3	0.188	0.180	0.008	0.189	-0.001	0.264	**-0.033**	0.0096
5	0.188	0.195	-0.003	0.190	-0.002	0.210	**-0.070**	0.0116
9	0.199	0.191	0.004	0.192	0.007	0.212	**-0.065**	0.0136
11	0.224	0.220	0.004	0.242	**-0.012**	0.304	**-0.046**	0.0112
10	0.230	0.225	0.005	0.236	-0.012	0.324	**-0.074**	0.0119
14	0.261	0.249	**0.012**	0.276	**-0.015**	0.270	**-0.063**	0.0100
4	0.300	0.302	-0.001	0.305	-0.005	0.336	**-0.036**	0.0133
1	0.317	0.301	0.015	0.321	-0.004	0.403	**-0.086**	0.0150
6	2.170	2.046	**0.124**	2.046	**0.124**	2.138	**0.032**	0.0143

Table 5.1. The effect of parameter change on (APF) values. The parameters changed were the method for finding the APF, the background threshold settings, and the number of wedges used. Data were collected at 4.1 ms capture delay and 377 kPa absolute pressure. **Bold typeface** in the **headings** highlights parameter changes. **Bold typeface** in the **table** is used when the change in APF value exceeded uncertainty limits.

12 wedges	12 wedges	10 wedges	12 wedges
Using 100 Images	**Using Averaged Image**	**Using Averaged Image**	**Using Averaged Image**
1500 Bkg Threshold	1500 Bkg Threshold	1500 Bkg Threshold	2000 Bkg Threshold
Injector #	**Injector #**	**Injector #**	**Injector #**
Ref 5	Ref 5	13	Ref 5
Ref 5	Ref 5	Ref 5	Ref 5
13	13	Ref 5	13
8	8	8	8
2	2	2	2
15	15	12	15
7	12	15	15
12	7	15	12
15	15	7	5
3	3	3	9
3	3	3	7
5	9	5	3
9	5	9	3
11	11	10	14
10	10	11	11
14	14	14	10
4	1	4	4
1	4	1	1
6	6	6	6

Table 5.2. The effect of parameter change on injector order. Injectors in ascending order based on average APF values.

5.4. Fuel Air Delay Settings

As previously mentioned in Section 4.3.1, all of the data presented to this point was erroneously collected with the fuel air delay (FAD) set to 0.952 ms (4 CAD @ 700 rpm) instead of 4 ms. To gauge the effects of this, a limited number of tests were conducted.

In the first test, a representative set of injectors was chosen based on their APF values at a capture delay of 4.1 ms. The list included an injector with a low APF value (R5), the two reference injectors with higher APF values (R2 and R3), the injector with the second highest APF value (#1), two of the blind injectors with lower APF values (#13 and #8), and two of the blind injectors with higher APF values (#4 and #14). These injectors were tested at both FADs (0.952 ms and 4 ms), at a capture delay of 4.1 ms, and a vessel pressure of 377 kPa absolute to test for any changes in APF values.

Figure 5.11 shows the effects of the FAD change. The x axis of the graph is the APF value for the 0.952 ms FAD, and the y axis is the APF value for 4 ms FAD. The line was added to the graph to measure the relative change in APF. The closer an injector was to the line, the less the injector APF changed with the increased FAD. The results show two injector runs were relatively unaffected by the change in FAD (R3 and R5). The injectors most affected by the change were #1, #4, and #14. This was noteworthy because #1 has been identified by Mercury as a bad injector, and #4 and #14 had the third and fourth highest APF values in the original tests at 4.1 ms, 377 kPa, and 0.952 ms FAD. All three of these injectors had lower APF values than injectors R2 and R3 at 4 ms FAD. Based on these results, the separation between the good and bad injectors has been eliminated with the increased FAD.

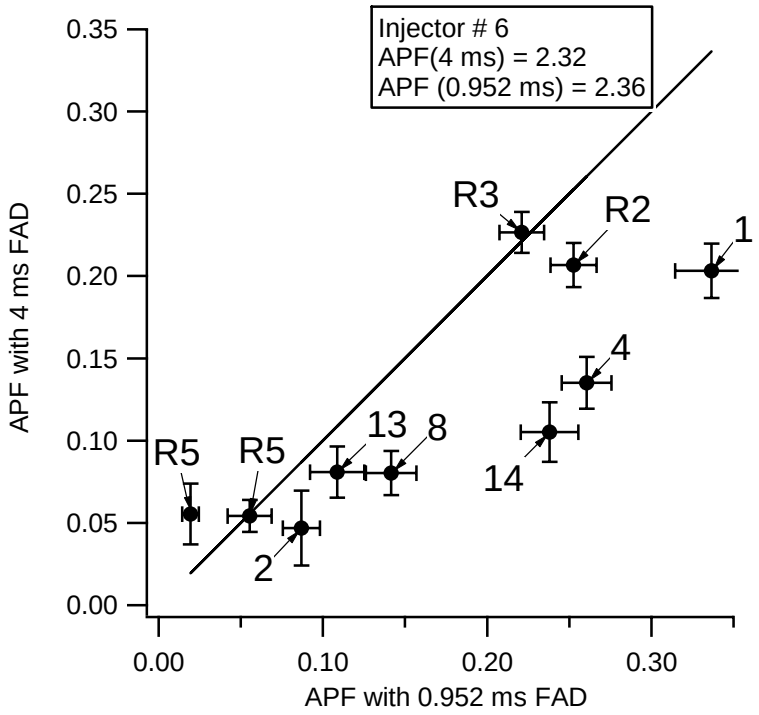

Figure 5.11. A comparison of APF values with different FAD. Y axis FAD = 4 ms. X axis FAD = 0.952 ms. Data were collected at 4.1 ms and 377 kPa absolute pressure.

It was hypothesized that increased fuel-air delay times would yield faster mixing of the spray, which could advance the injection phasing. To test this theory, injector R5 was tested throughout its injection duration at FADs of 0.952 ms and 4 ms. Figures 5.12 and 5.13 present the results of this test. From these images it was apparent that the hypothesis was correct. It appeared that the whole injection event was advanced about 400 μs. The other major difference caused by the increased FAD was the improved hollow cone structure observed at the unpressurized data points, shown in Figure 5.12.

To observe the differences between a bad and a good injector at a FAD of 4 ms, injector #1 was tested as well. Figure 5.14 and 5.15 compare the images of injector #1 and R5 using a FAD of 4 ms. The graphs show that strong differences still exist despite the

change in fuel air delay. Injector #6 was also tested with a FAD of 4 ms, but showed little-to-no improvement in its performance.

These results show that testing at data points with smaller capture delay times could show similar trends to the results found with the short fuel air delay. The improved hollow cone structure displayed by injector R5 at ambient pressure also suggests that meaningful data could be acquired without requiring vessel pressurization.

	Capture Delay Times (ms)					
FAD	2.1	2.2	2.3	2.4	2.5	2.6
4 ms	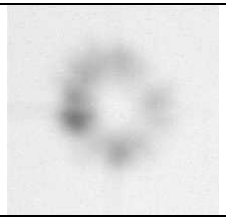	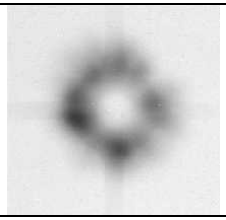	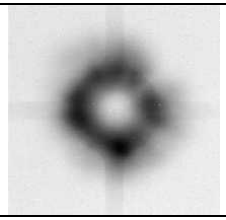	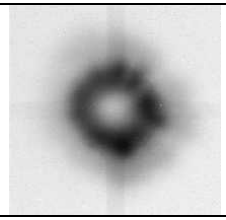	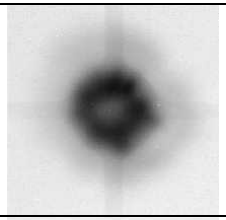	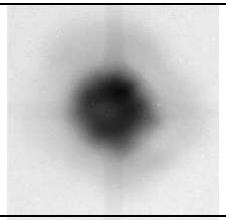
0.952 ms					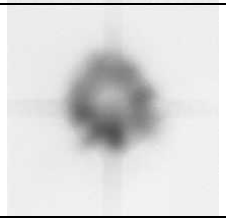	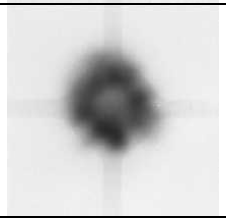

	Capture Delay Times (ms)				
FAD	2.7	2.8	2.9	3.0	3.1
4 ms	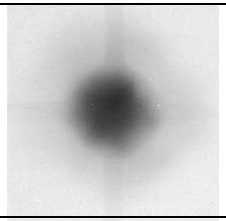	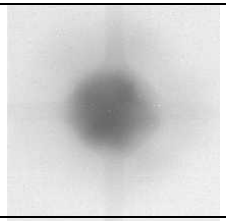			
0.952 ms	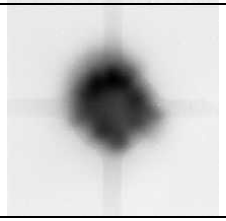	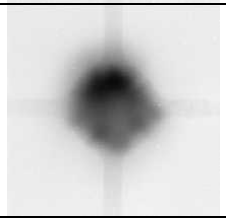	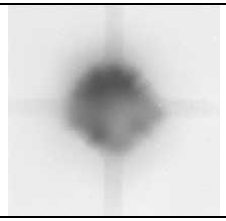	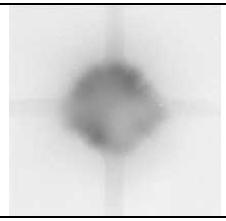	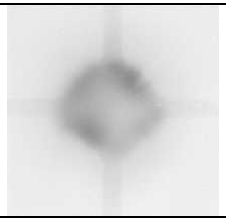

Figure 5.12. Impact of FAD on spray phasing. Images of injector R5 at different capture delay times at atmospheric pressure with FAD of 0.952 ms and 4 ms.

	Capture Delay Times (ms)									
FAD	2.6	2.7	2.8	2.9	3.0	3.1	3.2	3.3	3.4	3.5
4 ms	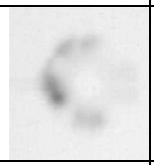	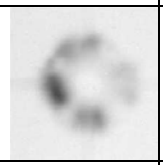	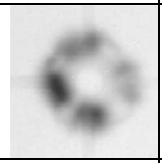	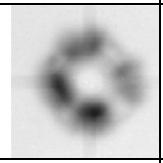	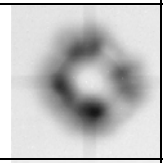	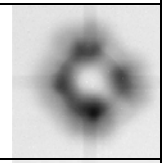	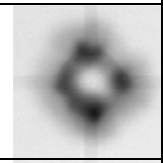	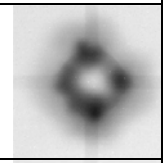	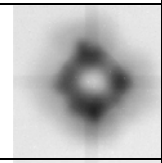	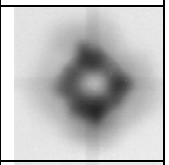
0.952 ms					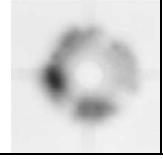	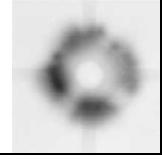	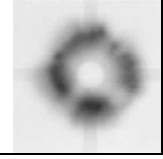	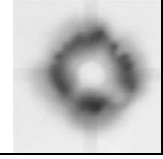	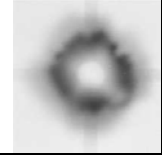	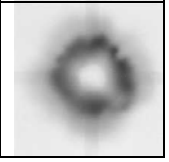

	Capture Delay Times (ms)									
FAD	3.6	3.7	3.8	3.9	4.0	4.1	4.2	4.3	4.4	4.5
4 ms	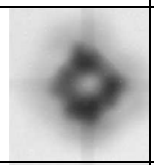	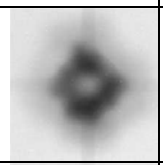	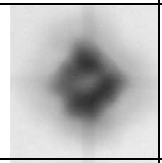	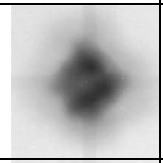	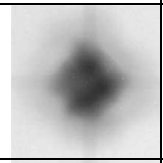	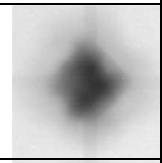	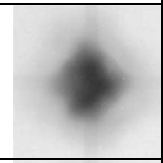	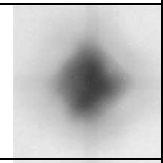	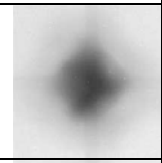	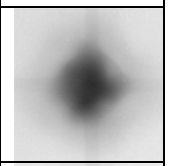
0.952 ms	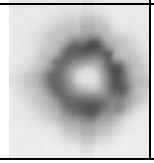	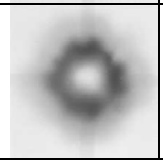	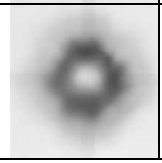	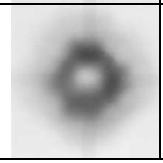	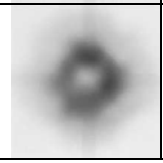	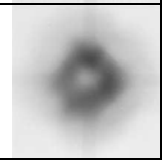	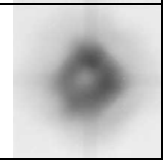	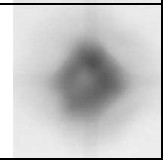	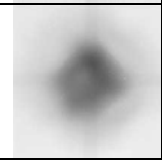	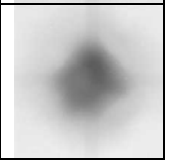

Figure 5.13. Impact of FAD on spray phasing. Images of injector R5 at different capture delay times at 377 kPa absolute with FAD of 0.952 ms and 4 ms.

	Capture Delay Times (ms)			
Injector	2.1	2.2	2.3	2.4
R5	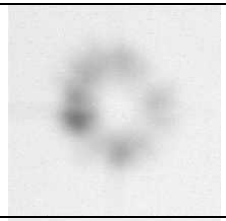	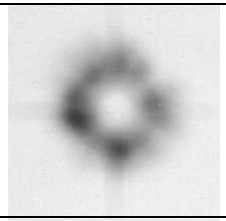	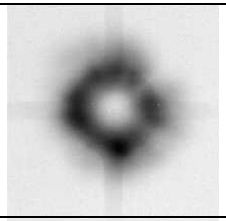	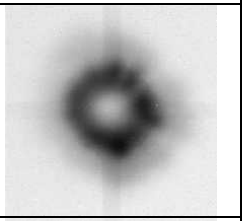
1	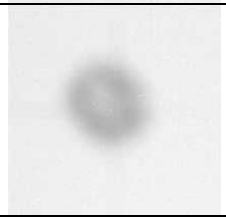	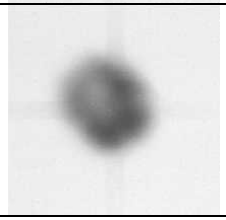	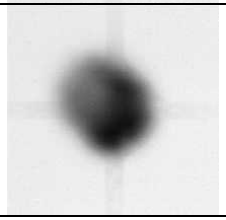	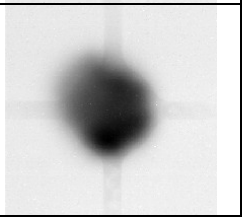

	Capture Delay Times (ms)			
Injector	2.5	2.6	2.7	2.8
R5	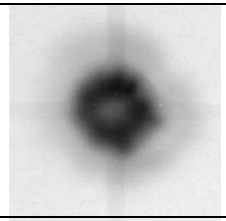	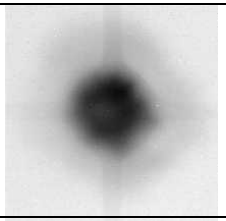	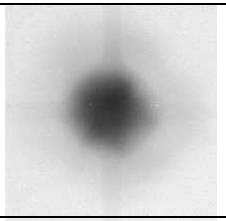	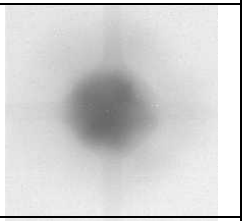
1	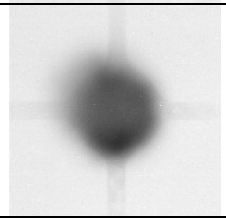	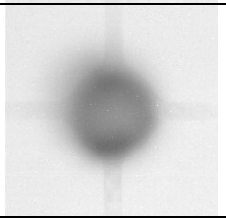	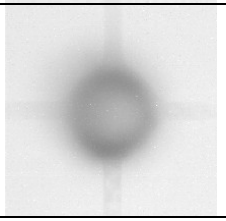	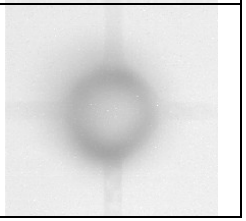

Figure 5.14. Comparison of a good injector (R5) to a bad injector (#1) with a FAD of 4 ms and varying capture delay times at atmospheric pressure.

	Capture Delay Times (ms)									
Inj.	2.6	2.7	2.8	2.9	3.0	3.1	3.2	3.3	3.4	3.5
R5				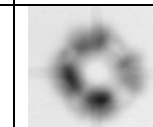	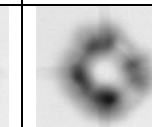	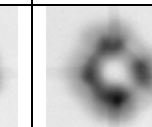	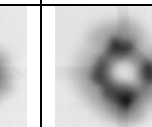	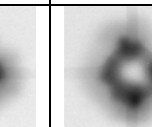	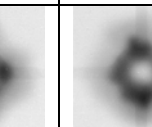	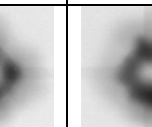
1				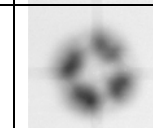	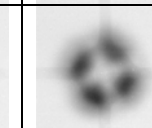	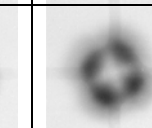	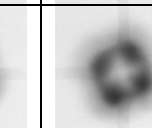	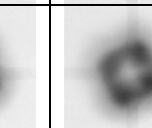	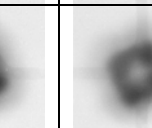	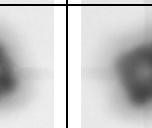

	Capture Delay Times (ms)									
Inj.	3.6	3.7	3.8	3.9	4.0	4.1	4.2	4.3	4.4	4.5
R5	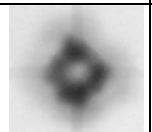	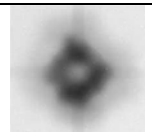	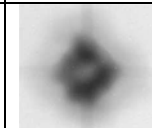	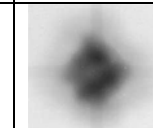	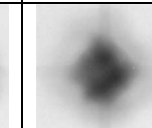	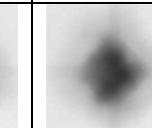	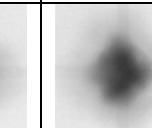	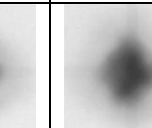	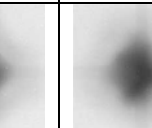	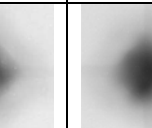
1	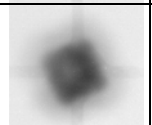	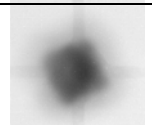	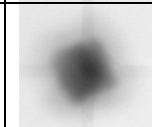	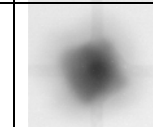	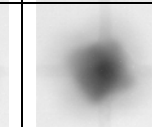	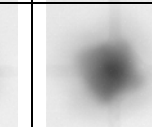	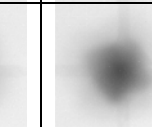	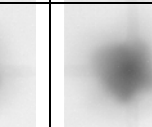	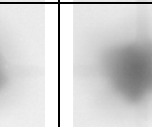	

Figure 5.15. Comparison of a good injector (R5) to a bad injector (#1) with a FAD of 4 ms and varying capture delay times at 377 kPa absolute pressure.

6.0. Conclusions and Recommendations

6.1. Conclusions

This project was conducted to determine if more modern optical methods could more accurately predict an injector's engine performance. A bank of 21 injectors was tested using, conventional Mie scattering techniques. Before testing, Mercury disclosed the identity of six good injectors and two bad injectors. A testing apparatus was constructed, which allowed optical access for spray illumination and visualization at pressures up to 650 kPa. The injectors were tested by taking images of a thin cross section of a fuel spray, illuminated with counter-propagating in-plane laser sheets. Data were collected at five different capture delay times with two different vessel pressures. Preliminary tests showed the presence of secondary scattering, but besides using counter-propagating laser sheets to correct for laser sheet extinction, no attempts were made to correct for its effects.

After the images were background-subtracted, the average image and an image showing the standard deviation of each pixel value were computed for each injector at the five test conditions. Visual analysis of these images was only capable of identifying the reference injectors and the worst injector (#6).

Statistical analysis using Insight 3G software produced better results. Using a pattern factor tool, which measured spray symmetry, a combination of inputs grouped the most of the reference injectors together in one range, the bad injectors in another range and the blind injectors in between the two ranges.

Dividing the images into 12 wedge sections and calculating the area pattern factor at a capture delay time of 4.1 ms, a vessel pressure of 377 kPa, and a FAD of 0.952 ms created

desirable separation between the good and bad injectors. A possible explanation for the separation occurring at a capture delay of 4.1 ms is that it was early enough to limit the amount of secondary scattering, but late enough to allow the spray to develop. Good results were also found using the same parameters, but with a capture delay time of 3.6 ms. Of the blind injectors, #2, #8, and #13 were good, and #4, #10, and #14 were bad. The APF values of the remaining injectors were near the data set mean.

The pattern factor calculations were sensitive to changes in the background threshold settings, the method of finding the average APF, and the number of sections used to divide the image. Because of this sensitivity, the ranking of the injectors with APFs near the data set mean could not be determined.

Unpressurized data using a FAD of 0.952 ms did not produce desired results. However, based on the images of injector R5, using a FAD of 4 ms could produce better results.

The major data set was taken with a FAD of 0.952 ms, instead of 4 ms. When data were taken with a capture delay of 4.1 ms and a FAD of 4 ms, the separation between the good injectors and the bad injectors was reduced. However, pictures of the injection timing at 4 ms suggest that testing at earlier capture delay times could yield better separation.

In conclusion, the research conducted in this project was capable of identifying very good and very bad injectors, but was unable to differentiate between the moderate performing injectors. Additional research could provide better results, but the non-linear nature of evaporation, turbulent mixing and combustion suggest that small changes in injector performance could either be amplified or dampened, which *a priori* testing would not be able to predict.

6.2. Recommendations

Much could be done to build upon the research conducted in this project. The first recommendation would be to run a representative (or full) set of injector tests with the current setup at a FAD of 4 ms. Tests would consist of three data points: two at atmospheric pressure, using capture delay times of 2.3 and 2.5 ms and one at 377 kPa absolute pressure, using capture delay times of 3.6 or 3.7 ms.

To gauge the success of the project results, the injector engine test results should be compared to their APF values. If the values do not match the engine test findings, it would be beneficial to see if other combinations of pattern factor parameters were more accurate in predicting injector performance. If the general method used in this project shows the potential to improve upon current testing procedures, there are commercial products available that use similar methods to test injectors [20]. A more costly but more useful way of researching injector performance would be to create an optical engine for testing. This would not only aide in injector testing, but could also be useful in future injector development for emissions reduction or performance improvements.

It would also be beneficial to look into the methodology that allowed injector #6 to pass initial inspection, and what caused it to malfunction.

There are many improvements that could be made to the current optical setup. Assuming the major components would remain unchanged, it would be beneficial to install cylindrical and spherical lenses with longer focal lengths. The cylindrical focal length was very small, which caused the laser sheet to expand rapidly. Since the spherical lens was placed about 50 cm away from the cylindrical lens, a large amount of laser light was lost between the two lenses. If the focal length of the spherical lens was larger, the optics used to

orient the sheet in the vessel would not need to be in such close proximity to the vessel itself. This would help prevent the mirrors from being bumped when changing injectors or cleaning the windows.

If possible, the setup could be greatly simplified if the Bragg cell was removed. The argon ion laser required a lot of power, and the many sheet forming optics wasted a lot of light energy. If the camera proved to have a sufficiently fast frame rate, the Bragg cell the beam stops could be removed, which would increase the intensity of light that illuminates the spray.

The test apparatus itself could also be improved. Adjustments could be made to increase flow, specifically by installing a less restrictive exhaust line. Measuring the velocities in the cylinder would also be useful in determining the velocity profile created by the porous metal assembly.

Any changes that would allow faster injector characterization would also be beneficial. Processing the data in Insight was quite time consuming and required a lot of user input. If programs could be created that allowed data to be processed with little to no user input, data could be processed overnight. In testing, about half of the time required to test each injector was spent cleaning windows, and aligning the vessel. If the windows stayed clean and the vessel did not have to be moved to change injectors, testing time could be greatly reduced. Increasing vessel flows and the focal length of the spherical lens could solve these problems. Testing time could also be reduced if a test was run to find the minimum amount of shots required to characterize an injector.

These recommendations could increase the accuracy and efficiency of injector characterization.

References

[1] Ghandhi, J.B., 1995, *Fuel distribution measurements in a direct injection stratified charge engine*, Ph.D. Thesis, Department of Mechanical and Aerospace Engineering, Princeton University.

[2] Jermy, M.C. and Greenhalgh, D.A., 2000, "Planar Dropsizing by elastic annd fluorescence scattering in sprays too dense for phase Doppler measurement," *Applied Physics B*, v.71, pp703-710.

[3] Talley, D.G., Thamban, A.T.S., McDonell, V.G., and Samuelsen, G.S., 1996, "Laser sheet visualization of spray structure," *Progress in Astronautics and Aeronautics*, v.171, pp113-141.

[4] Le Gal, P., Farrugia, N., and Greenhalgh, D.A., 1999, "Laser sheet dropsizing of dense sprays," *Optics and Laser Technology*, v.31, pp75-83.

[5] Sankar, S.V., Maher, K.E., Robart, D.M., and Bachalo, W.D., 1999, "Rapid characterization of fuel atomizers using an optical patternator," *Journal of Engineering for Gas Turbines and Power*, v.121, pp409-414.

[6] Koh, H., Jeon, J., Kim, D., Yoon, Y., and Koo, J., 2003, "Analysis of signal attenuation for quantification of a planar imaging technique," *Measurement Science and Technology*, v.14, pp1829-1838.

[7] Brown, C.T., McDonell, V.G., and Talley, D.G., 2002, "Accounting for laser extinction, signal attenuation, and secondary emission while performing optical patternation in a single plane," *15th Annual Conference on Liquid Atomization and Spray Systems*, pp195-199.

[8] http://www.dantecdynamics.com/PDA/Princip/Index.html

[9] Hoffman, J.A., 1998, *Mass related properties of transient sprays*, Ph.D. Thesis, Department of Mechanical Engineering, University of Wisconsin-Madison.

[10] Wang, G., Deljouravesh, R., Sellens, R.W., Oleson, M.J., and Bardon, M.F., 1997, "An optical spray pattern analyzer," *10th Annual Conference on Liquid Atomization and Spray Systems*, pp261-265.

[11] Park, S., Cho, H., Yoon, I., and Min, K., 2002, "Measurement of droplet size distribution of gasoline direct injection spray by droplet generator and planar image technique," *Measurement Science and Technology*, v.13, pp859-864.

[12] Sick, V., and Stojkovic, B., 2001, "Attenuation effects on imaging diagnostics of hollow-cone sprays," *Applied Optics*, v.40, pp2435-2442.

[13] Jermy, M.C., and Allen, A., 2002, "Simulating the effects of multiple scattering on images of dense sprays and particle fields," *Applied Optics*, v.41, pp4188-4196.

[14] Iverson, R.J., 2004, *The effects of intake charge stratification on HCCI combustion,* M.S. Thesis, Department of Mechanical Engineering, University of Wisconsin-Madison.

[15] http://www.technicalglass.com/tech.htm

[16] http://www.mottcorp.com/resource/pdf/RS_Perm_all.pdf

[17] http://www.mottcorp.com/resource/pdf/RS_Air_Perm.pdf

[18] http://www.mottcorp.com/resource/pdf/porous.pdf

[19] McGuire, B.A., 2000, *Combustion and emissions potential in a direct injection 2-stroke engine*, M.S. Thesis, Department of Mechanical Engineering, University of Wisconsin-Madison.

[20] http://www.enurga.com/pdfiles/OP600.pdf

Appendix A - List of Equipment

Component	Manufacturer	Model Number	Serial Number
Laser Head	Lexel	95	
Laser Source	Lexel	295	1864 P.S.
Bragg Cell Driver	Intraaction	ME 38R	2676
Bragg Cell	Intraaction	AOM 405	5569
Power Meter	Newport	815	2531
Pulse Generator	Quantum Composers	9310 (front) 9314T (back)	9314T-004-206
Camera	Pixelink	A-741	7410247
Camera Lens	JML	71881	
Fuel Power Supply	Astron	RS-20A	9406524
Fuel Injector	Siemens	37-855356	
Fuel Conditioner	Nelson	Koalescer	
ECU	Motorola	PCM 0312M	
ECU Power Supply	Astron	RS-20A	200110847
Com Box	Mototron		

Table 1. List of Equipment

Appendix B - Engineering Drawings of Vessel Components

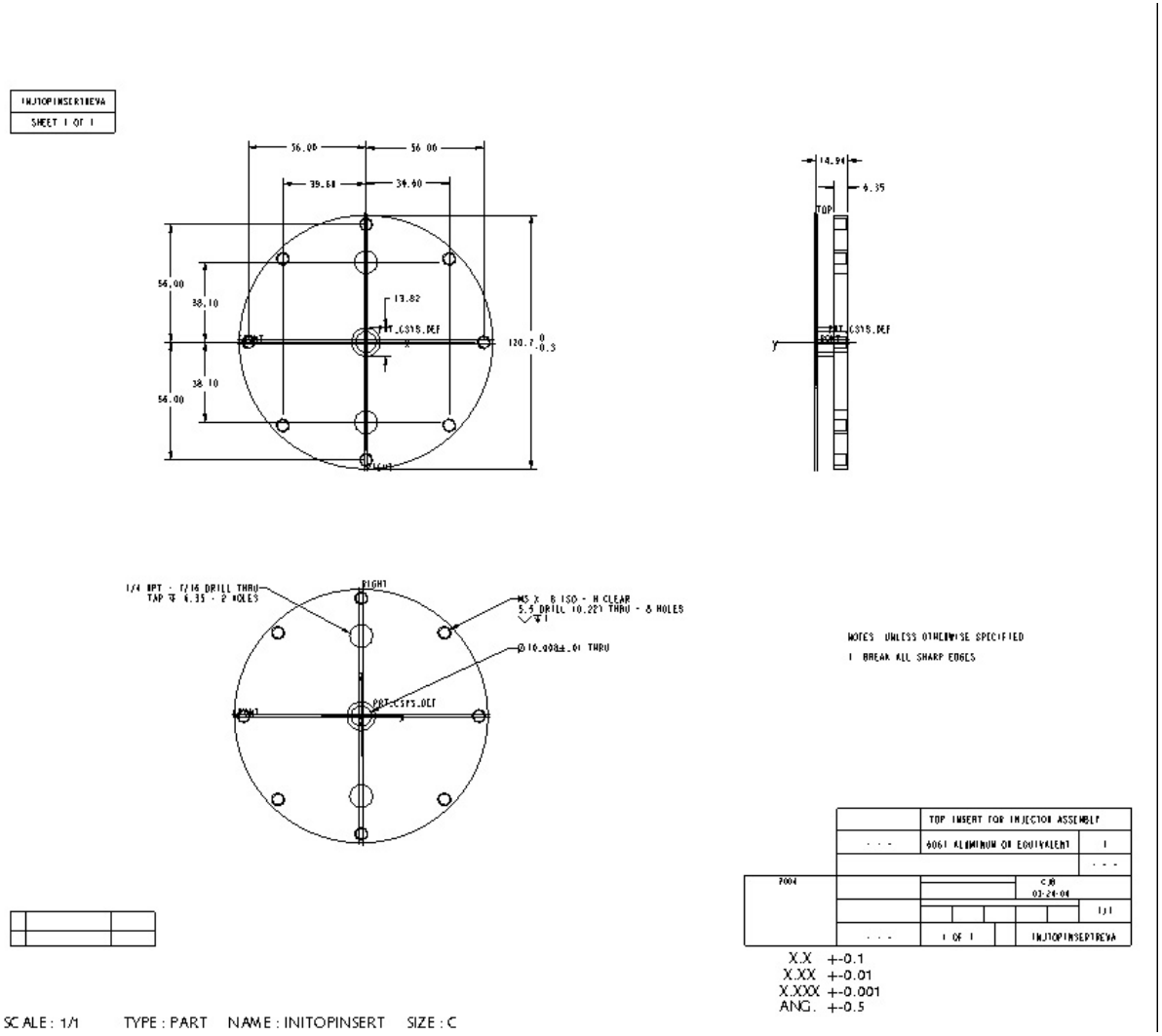

Figure 1. Engineering drawing of injector holder.

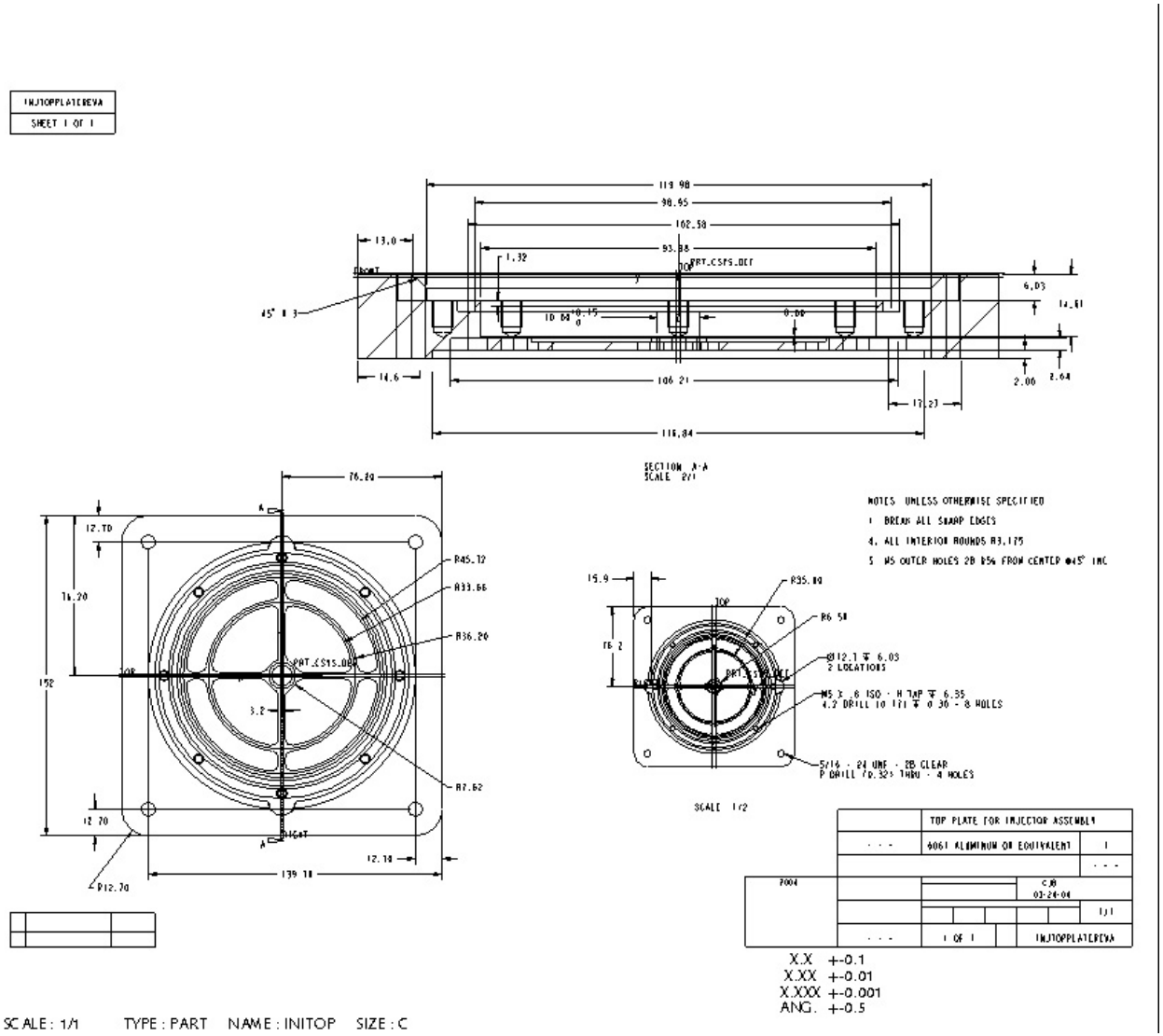

Figure 2. Engineering drawing of porous metal holder.

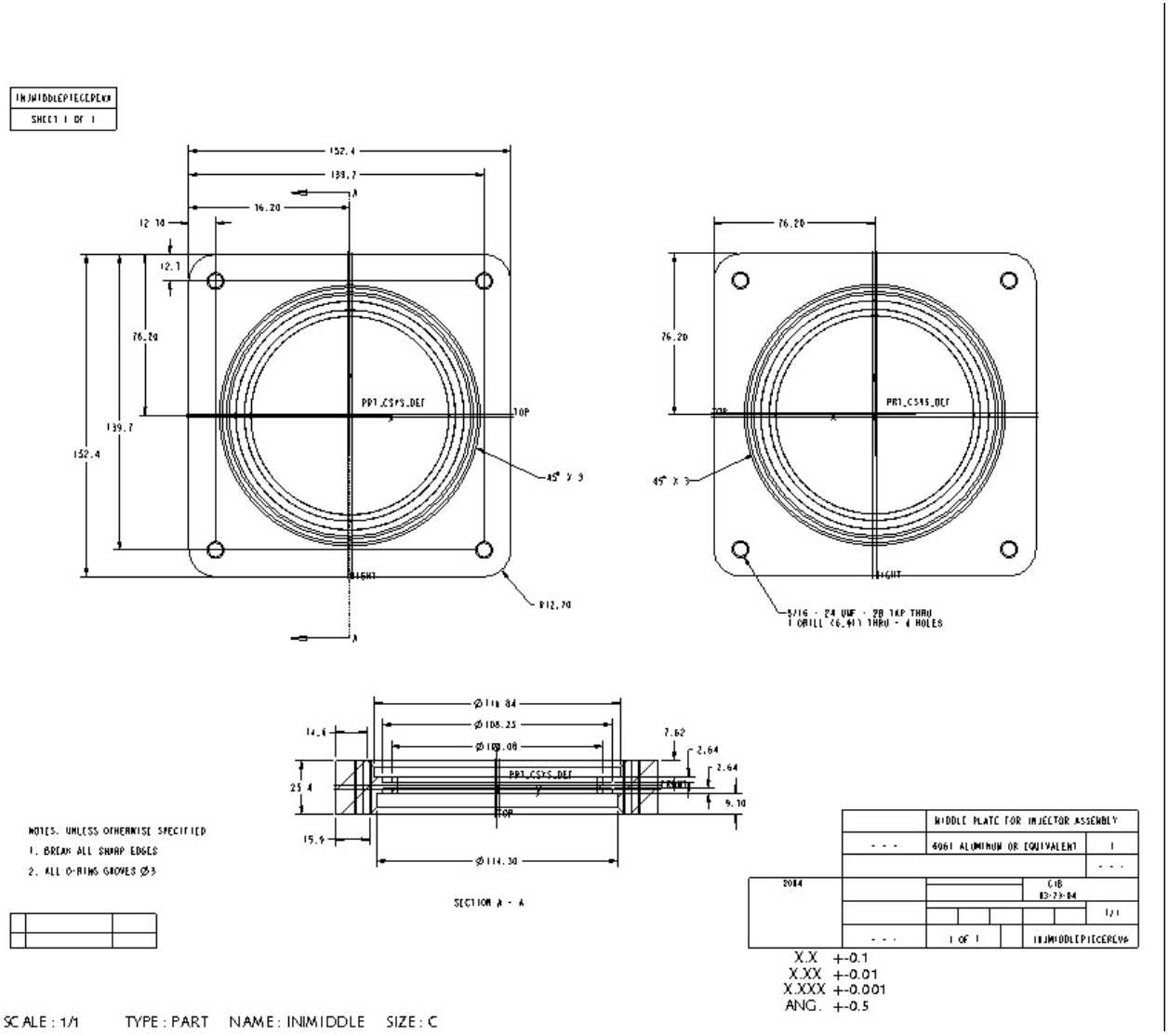

Figure 3. Engineering drawing of the middle plate that houses the metal tube and Pyrex cylinder.

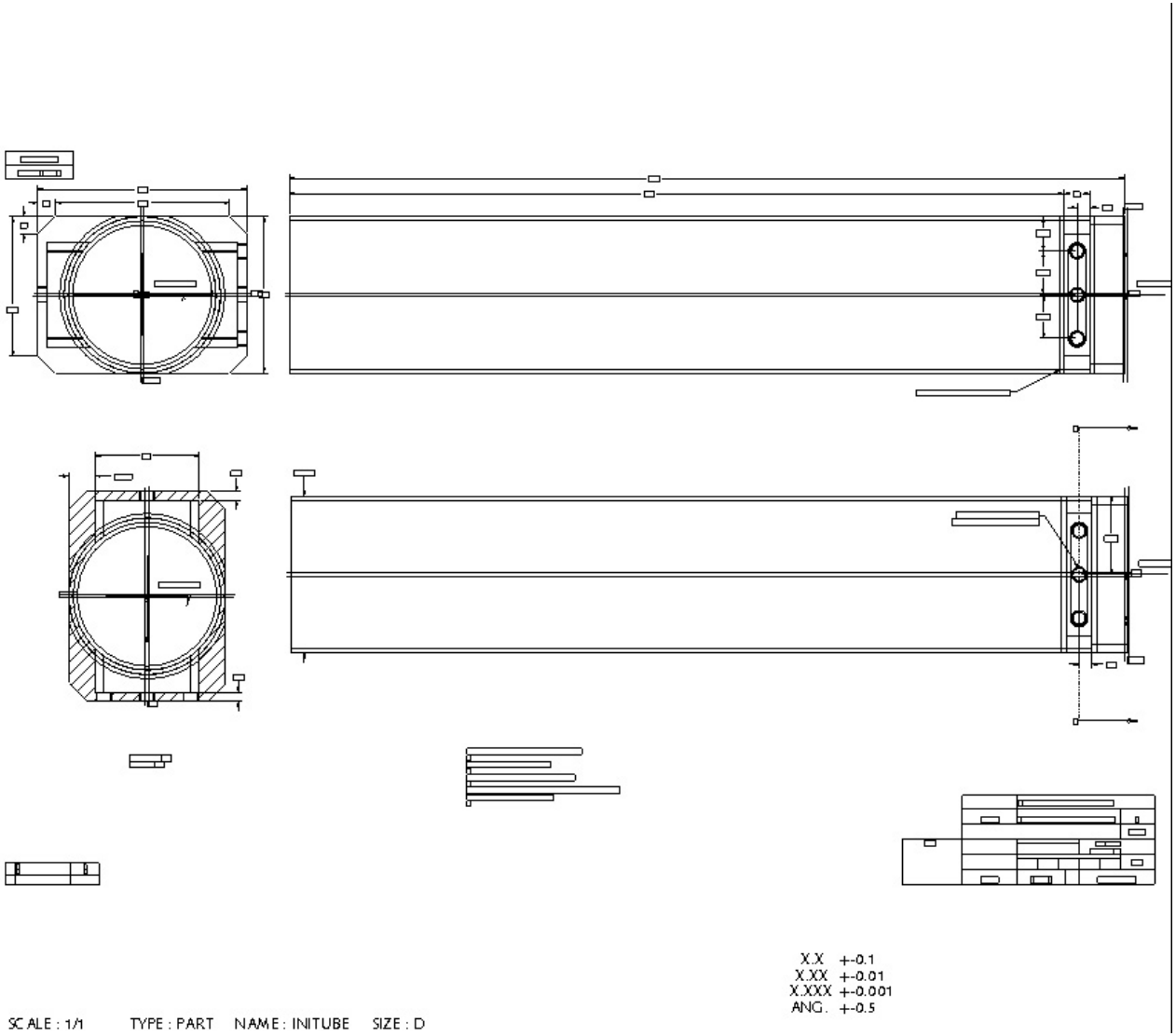

Figure 4. Engineering drawing of metal tube.

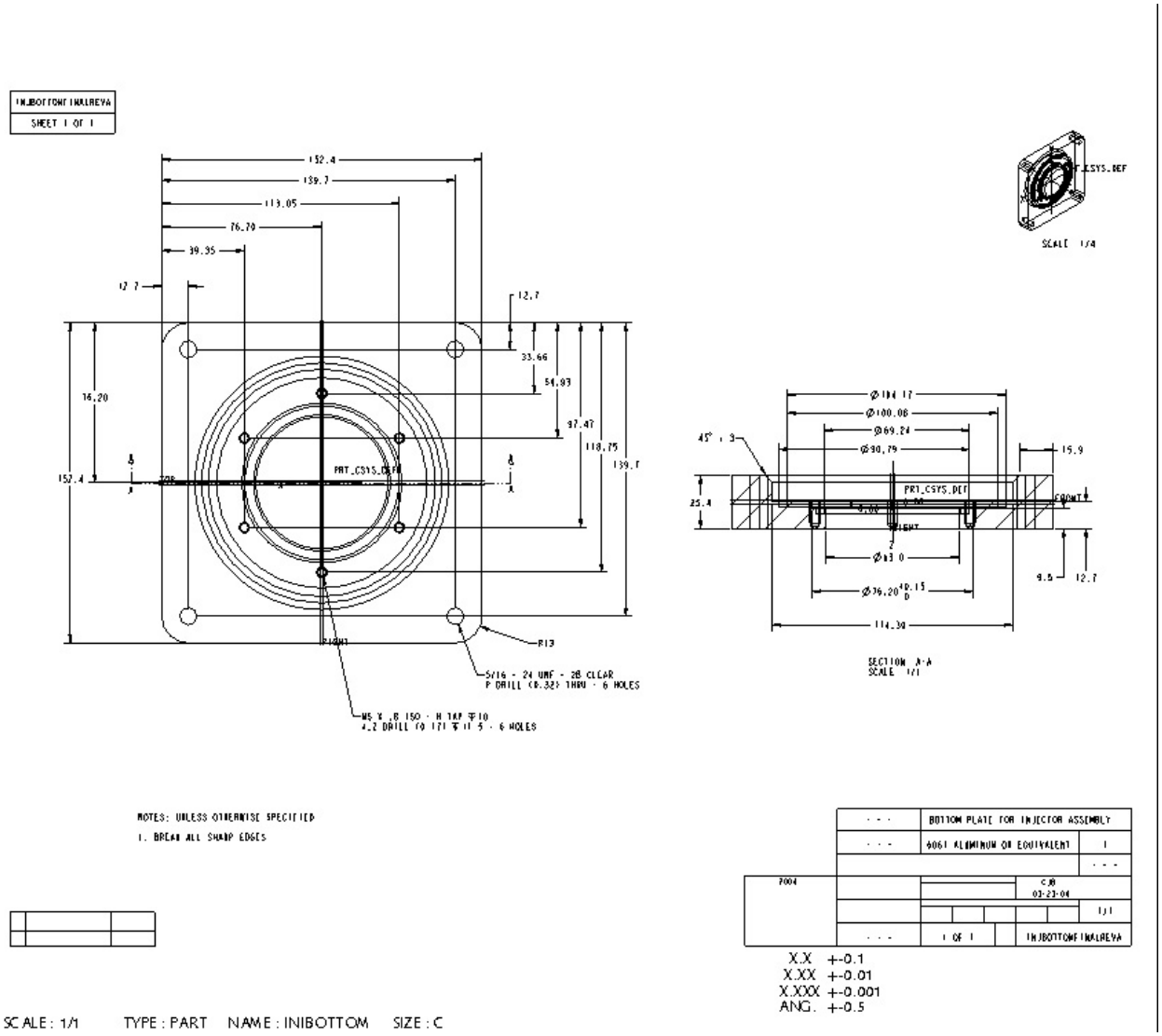

Figure 5. Camera window holder. Also houses the metal cylinder.

Appendix C - Camera Setting Optimization

Images were taken at different gain settings and brightness levels with the cap on the camera to quantify noise levels. Image histograms were then analyzed, and the brightness level that limited noise values as much as possible without clipping the signal was chosen for each gain value. Figure 6 shows the histograms of the optimized gain and brightness combinations.

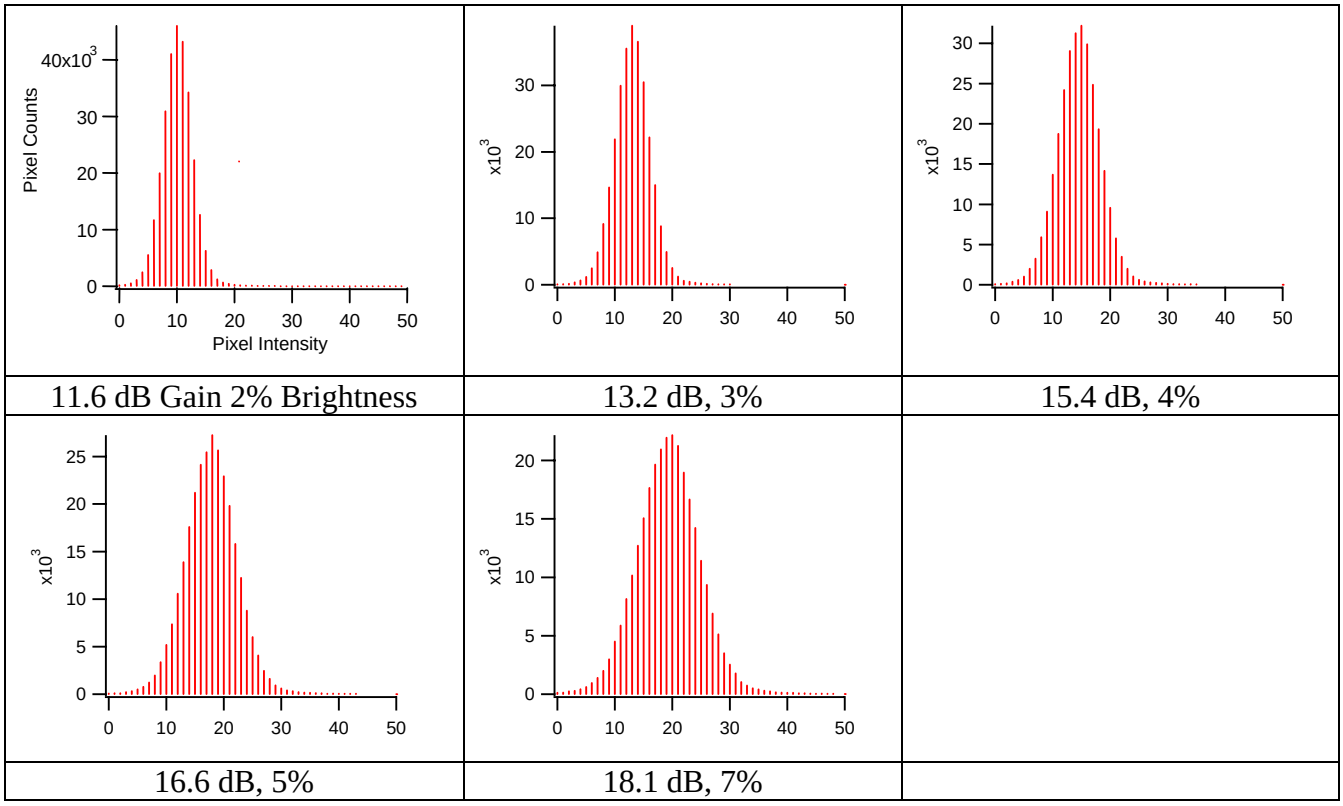

Figure 6. Histograms for the brightness and gain combinations that do not clip noise.

Appendix D - Fuel Rail Pressure Data

Upon taking some initial data, the shot-to-shot variability exhibited by the injectors raised concern that some undesirable pressure waves could be present in the fuel system. To explore this, a Kistler Piezotron 211B3 dynamic pressure transducer was installed in the fuel rail to measure pressure fluctuations during operation. The transducer was installed on both the air and fuel side of the rail. It measures only fluctuations from the static pressure, which was around 680 kPa (absolute) on the air side, and around 780 kPa (absolute) on the fuel side. This is why the graphs center on zero instead of the previously measured static pressures.

Five graphs are displayed here to characterize the pressure fluctuations in the rail. Figure 7 is a collection of 10 pressure traces from the fuel side of the rail, with the time scale set to focus on a single injection. This graph shows that there was not much variability from one pressure trace to another.

The last four figures (8-11) show a single trace that represents an average of 32 individual pressure traces. Figure 8 focuses on a single injection on the fuel side; Figure 9 shows multiple injections on the fuel side; Figure 10 contains a single injection on the air side; and Figure 11 has a trace that includes multiple injections on the air side.

The multiple injection graphs are meant to show that the pressure is stable before each injection. From these graphs, it was determined that there are no standing pressure wave issues with the fuel rail. The single injection pressure trace on the fuel side does have a sizeable pressure fluctuation during the injection period, but the pulse did not seem particularly abnormal since a pressure drop is expected when the injector opens.

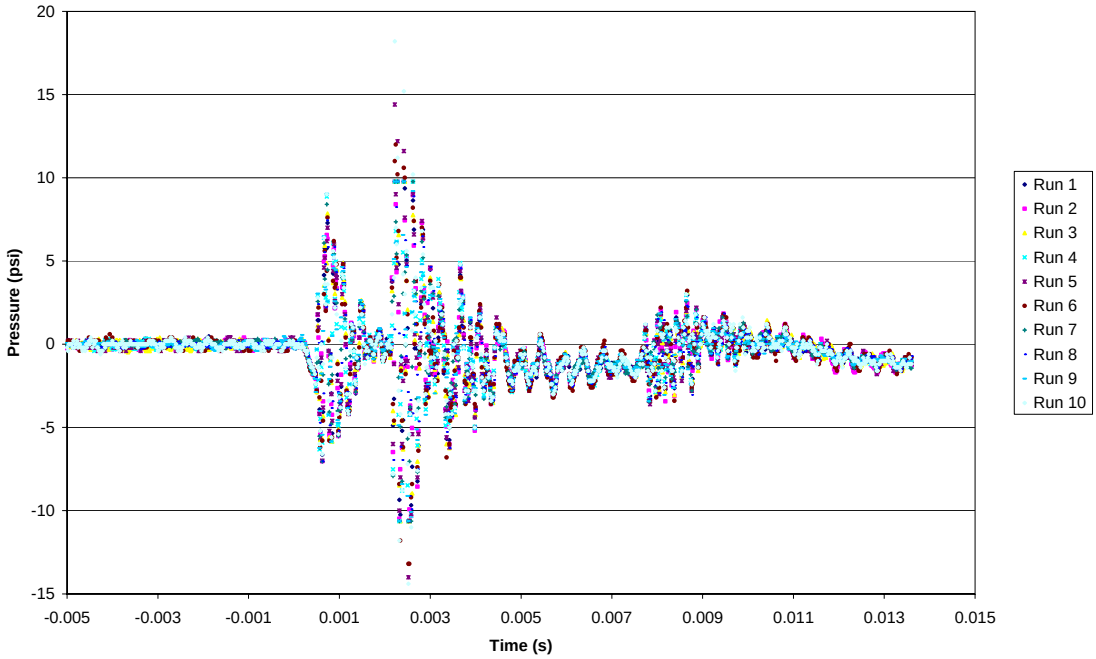

Figure 7. Fuel Side Pressure Comparisons (Single Injection)

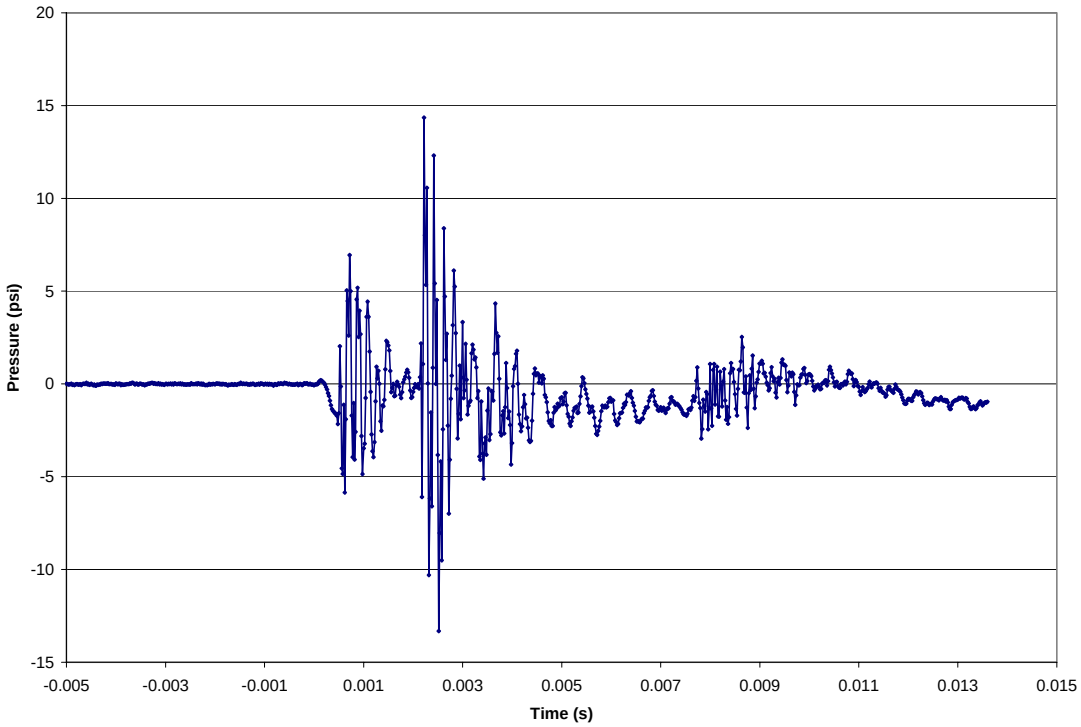

Figure 8. Average of 32 Fuel Pressure Traces (Single Injection)

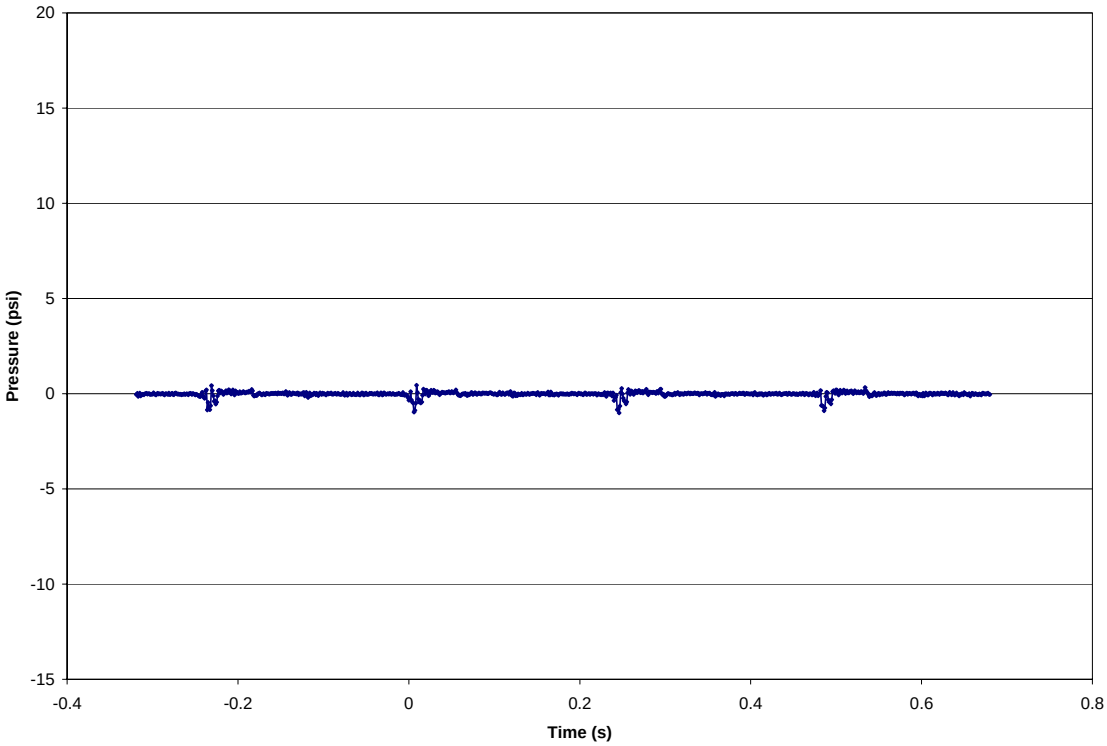

Figure 9. Average of 32 Fuel Pressure Traces (Multiple Injections)

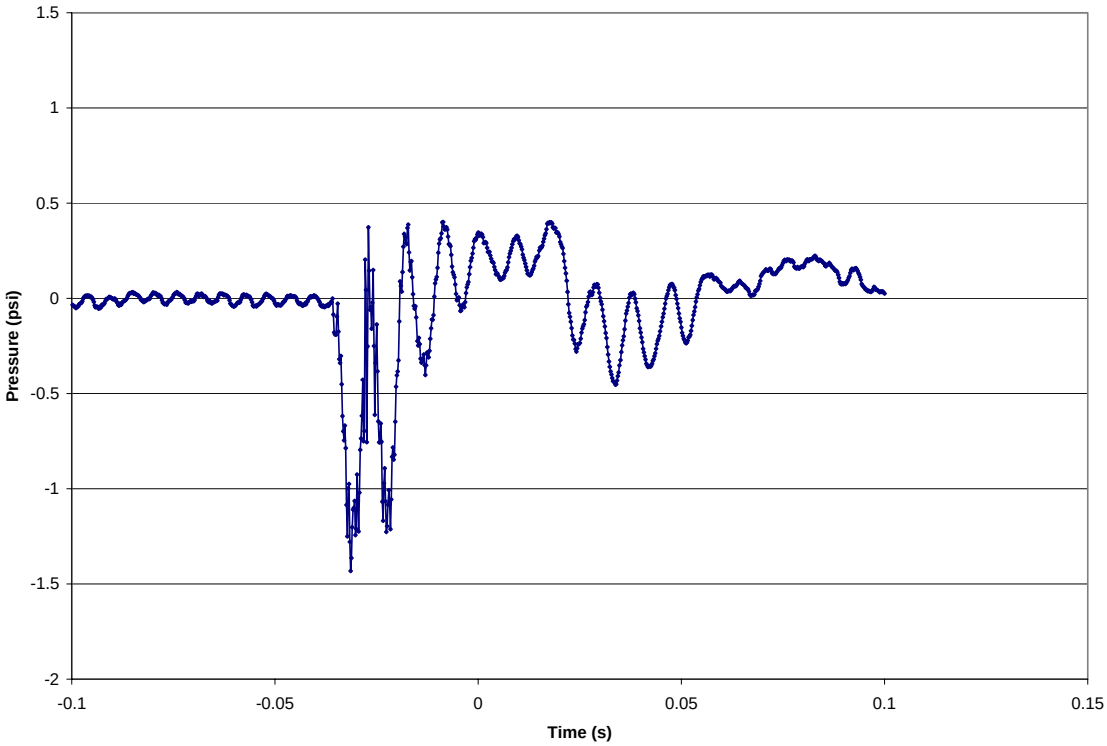

Figure 10. Average of 32 Air Pressure Traces (Single Injection)

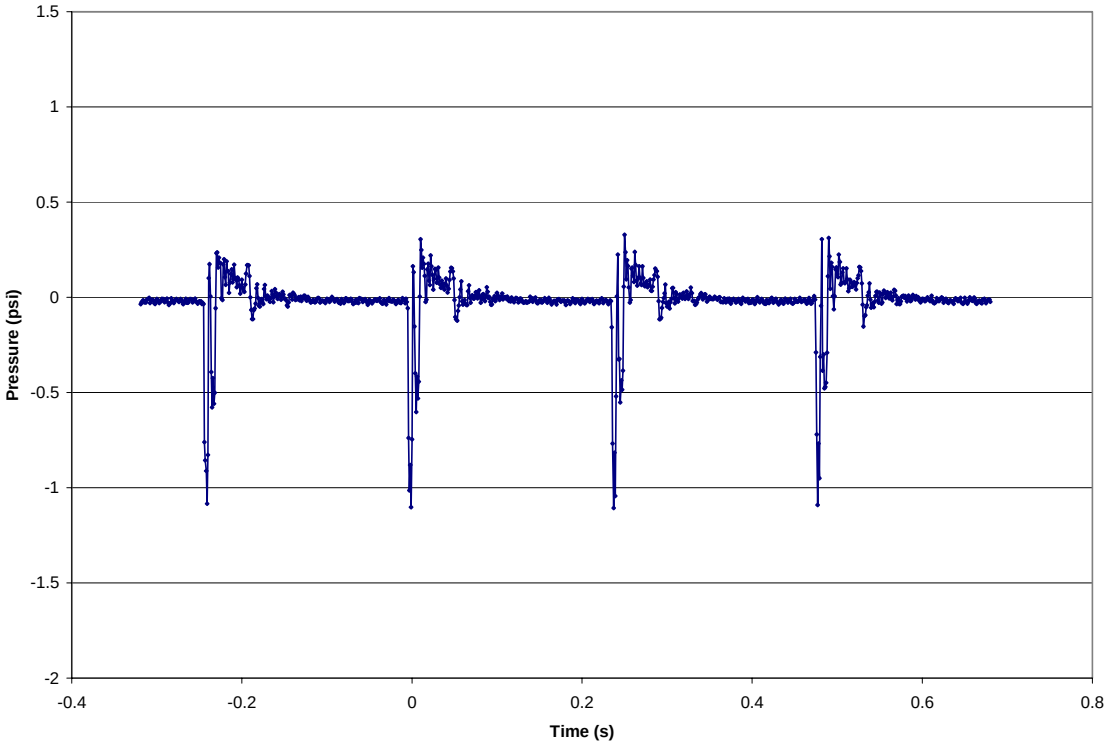

Figure 11. Average of 32 Air Pressure Traces (Multiple Injections)

Appendix E - Image Processing Procedure

The process for capturing images is listed in section 5.1.2.

Image Processing Steps:

(1) Select an empty folder to use for image analysis, using the Insight Setup function in the Tools section on the toolbar.

(2) Create an experiment and a run in Insight 3G.

(3) Change file names for input into Insight 3G, as described in Section 3.3.5, and move them to the raw images folder in the desired run. This format is only necessary for the data files. The background files only need a suffix change (*.tif needs to be changed to *.plif.tif).

(4) Create a single averaged background image from 100 total “before and after” background shots, using the Average Intensity Image Processor in the Setup Images tab of the PLIF/Spray conditioning menu.

(5) Create a condition using the Condition Setup tab. Select the Background Subtraction Image Processor from the Image Conditioner dialog box. Select the averaged background image using the Image Conditioner Settings tab, and save the configuration.

(6) Subtract the average background image from each raw data image by applying the condition created in step 5.

(7) Average the data images in the same manner that the background images were averaged in step 4.

(8) Find the center of the image by applying the 4 wedge divider in the Horizontal Pattern Factor tool and changing the x and y offsets until the “cross hairs of the pattern factor align with the slightly visible cross sections in the background of the images.

(9) Create a region of interest in the ROI menu that creates a box whose sides align tangentially with the horizontal pattern factor circle. Subtract the size of the ROI from the desired cropped image size (325, for this project). Divide this difference by two and add it to the offsets found in step 8. These values will be the top and left bounds used for cropping.

(10) Use a program (Matlab, Microsoft Photo Editor, Maxim DL) to crop the images using the bounds found in step 9. If a quick analysis is to be done, crop the averaged images of each injector. If a more thorough analysis is desired, crop all

of the background subtracted images (100 for each data point, 5 data points per injector).

(11) Analyze the cropped images using the Horizontal Pattern Factor tool in the PLIF/Spray menu, making sure to apply the proper background threshold.

- Any pixel below the background threshold is omitted from the area and mean pattern factor calculations. Setting a good background threshold emphasizes the calculation of "spray pixels", rather than noise.
- A sample of the pattern factor data for 100 images is contained in Figure 12.

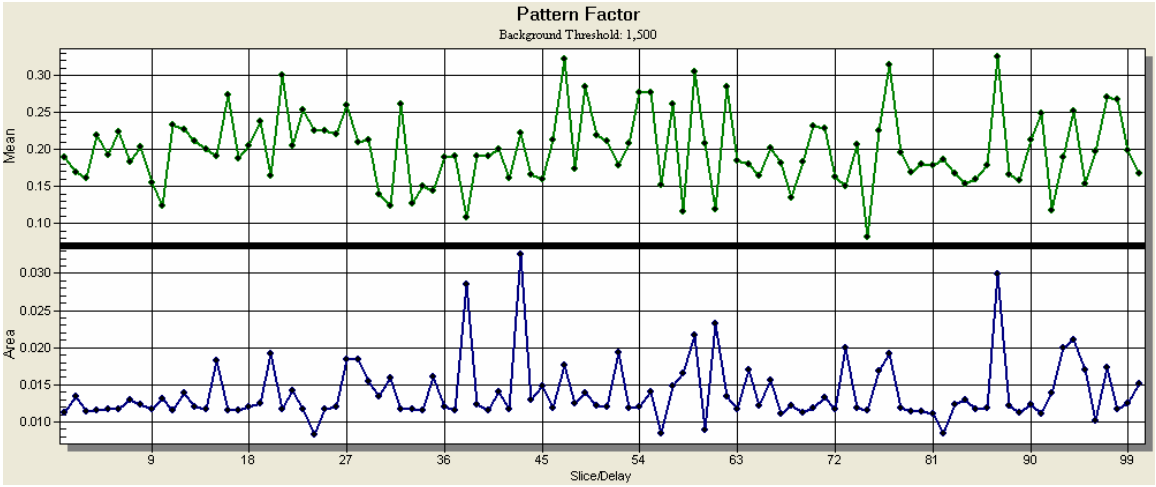

Figure 12. View of the mean and area pattern factor data of 100 images.

(12) Export pattern factor data to a spreadsheet.

(13) Compute mean and standard deviation of APF and MPF data for all injector runs.

(14) Compare mean APF and MPF values grouped by capture delay times. Section 5.3.1 shows a number of ways to graph these values.

(15) Use Equation (5.3) to calculate the uncertainty of each injector.

Pattern Factor Example Problems

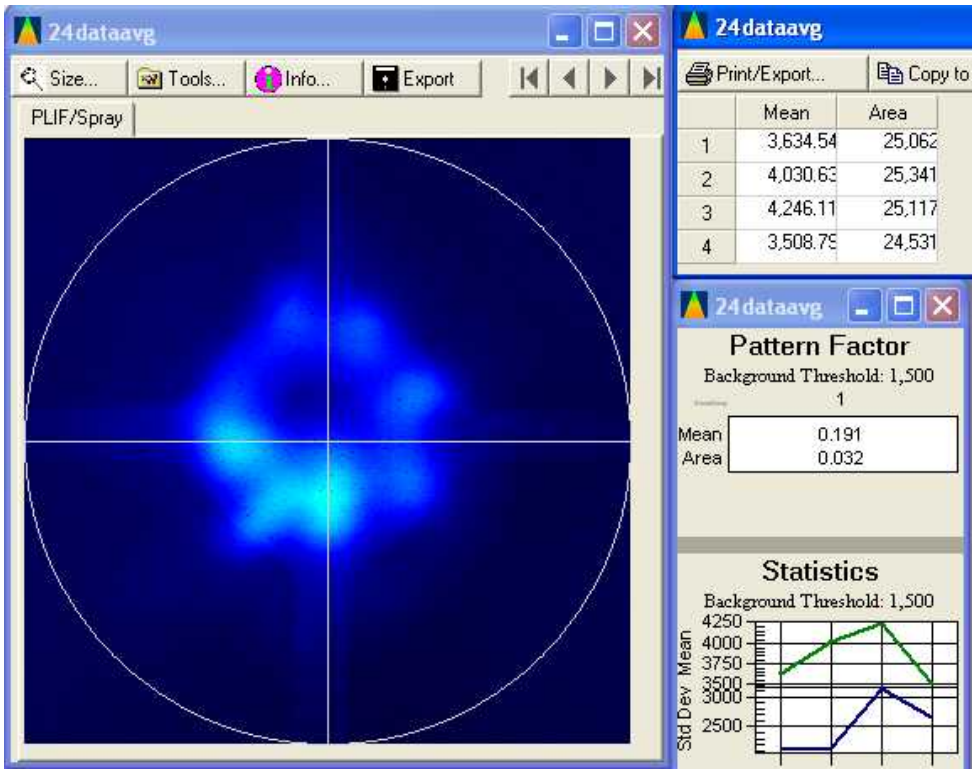

Figure 13. Analysis image accompanied by APF and MPF data.

Area Pattern Factor Calculation:

$$APF = \frac{Max\# - Min\#}{Mean\#}$$

$Max\# = 25{,}341$

$Min\# = 24{,}531$

$$Mean\# = \frac{25{,}062 + 25{,}341 + 25{,}117 + 24{,}531}{4} = 25{,}012.75$$

$$APF = \frac{25{,}341 - 24{,}531}{25{,}012.75} = .032$$

Mean Pattern Factor Calculation

$$MPF = \frac{Max - Min}{Mean}$$

$Max = 4{,}246.11$

$Min = 3{,}508.79$

$$Mean = \frac{3634.54 + 4030.63 + 3508.79 + 4246.11}{4} = 3855.02$$

$$MPF = \frac{4246.11 - 3508.79}{3855.02} = .191$$

Appendix F - Averaged Pictures of Injectors

	Atmospheric Pressure		377 kPa		
	2.5 ms	**2.7 ms**	**3.1 ms**	**3.6 ms**	**4.1 ms**
8	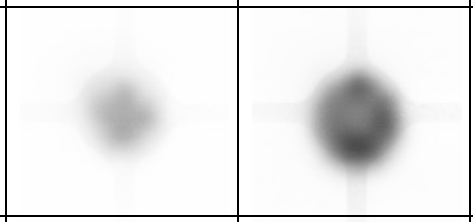				
2	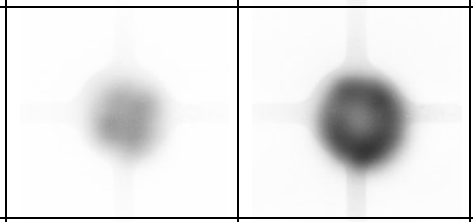				
15	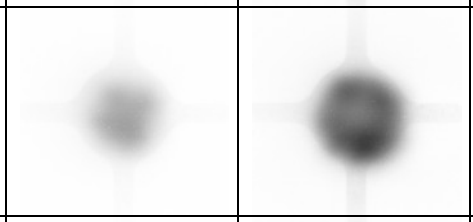				
7	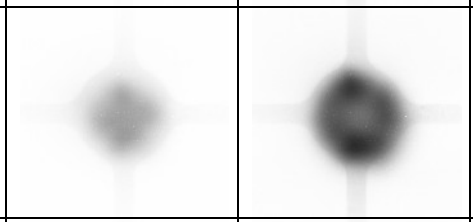				
12	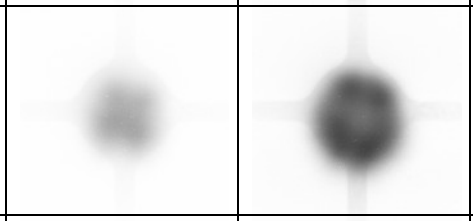				
15r	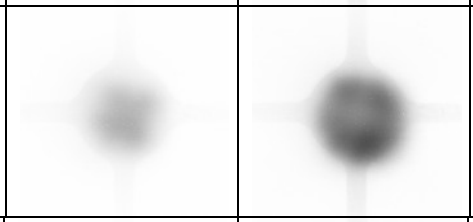				
3	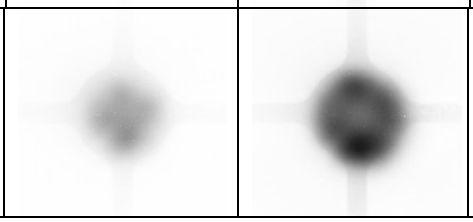				

	Atmospheric Pressure		377 kPa		
	2.5 ms	**2.7 ms**	**3.1 ms**	**3.6 ms**	**4.1 ms**
3r	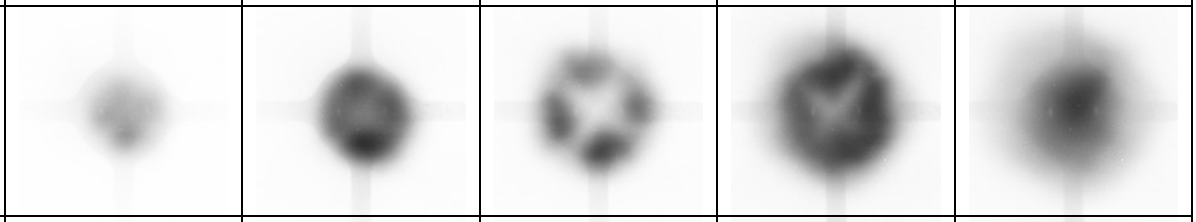				
5	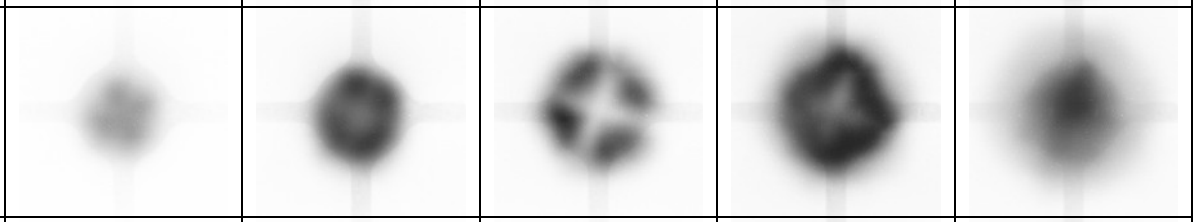				
9	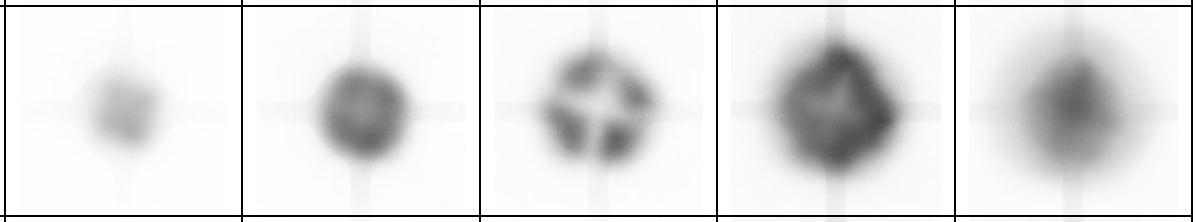				
11	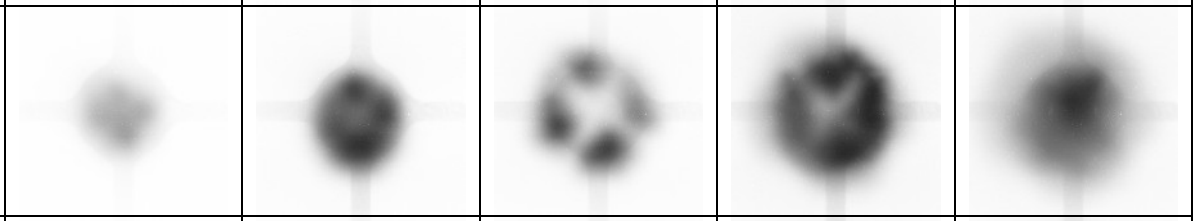				
10	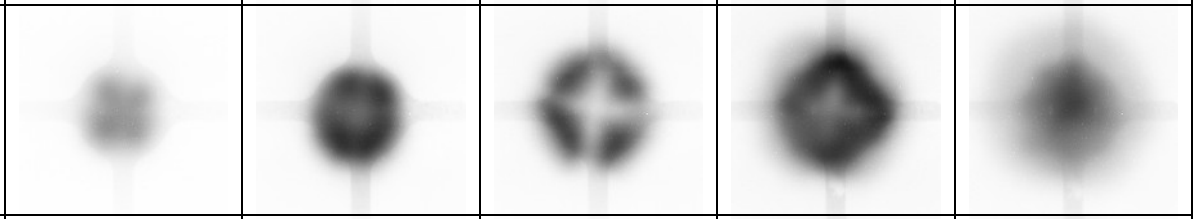				
14	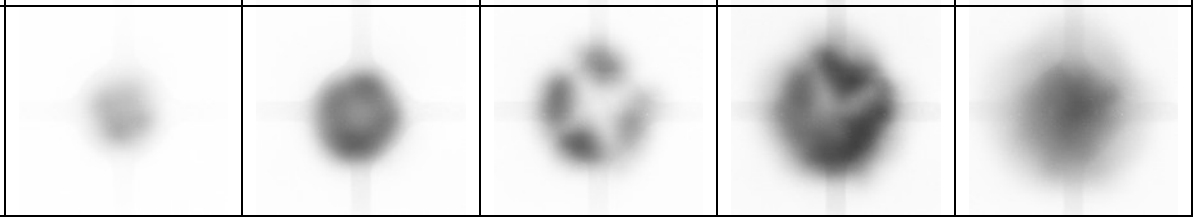				

Figure 14. Averaged image comparison of the remaining fuel injectors.

Appendix G - Results of Mean Pattern Factor Analysis

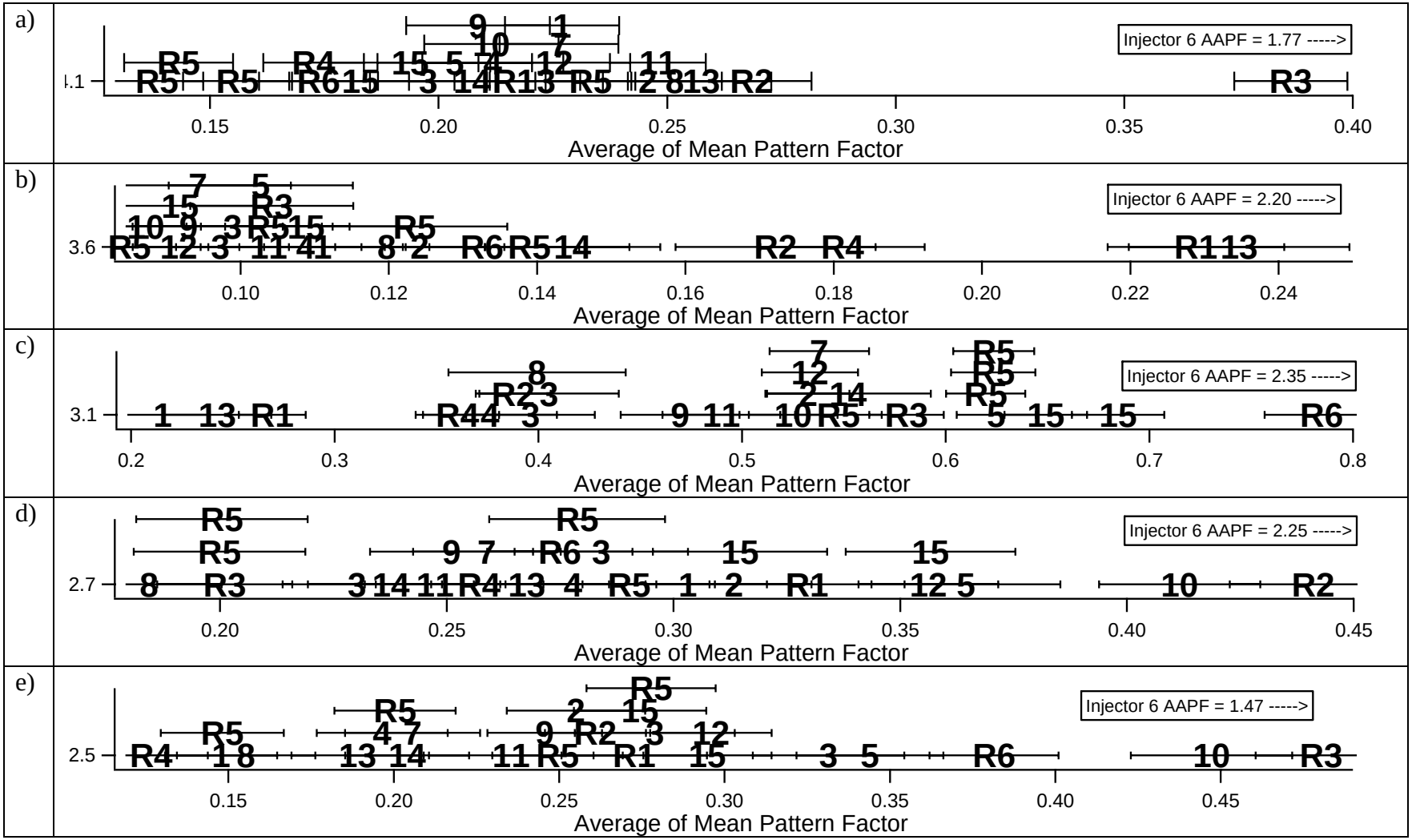

Figure 15. Mean pattern factor results at the five different capture delay times and two different pressures: a) 4.1 ms, 377 kPa; b) 3.6 ms, 377 kPa; c) 3.1 ms, 377 kPa; d) 2.7 ms, 101.4 kPa; e) 2.5 ms, 101.4 kPa. All pressures are absolute. 12 wedges, 1500 BT

Appendix H - Data Compiled using 10 Rings (Not 12 Wedges)

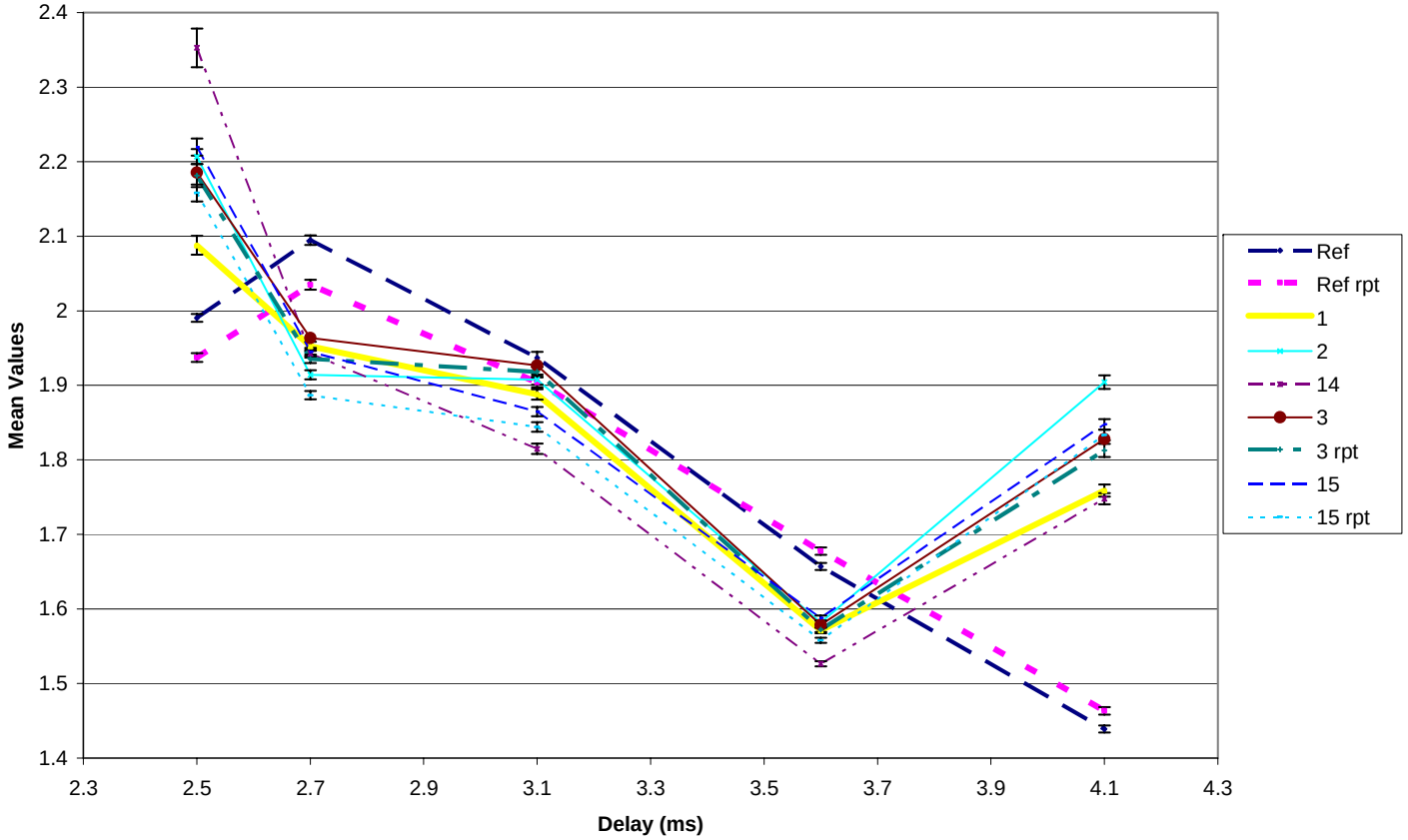

Figure 16. MPF data using 10 rings and BT of 1500. The bad injector (#1) was in the middle, which was undesirable.

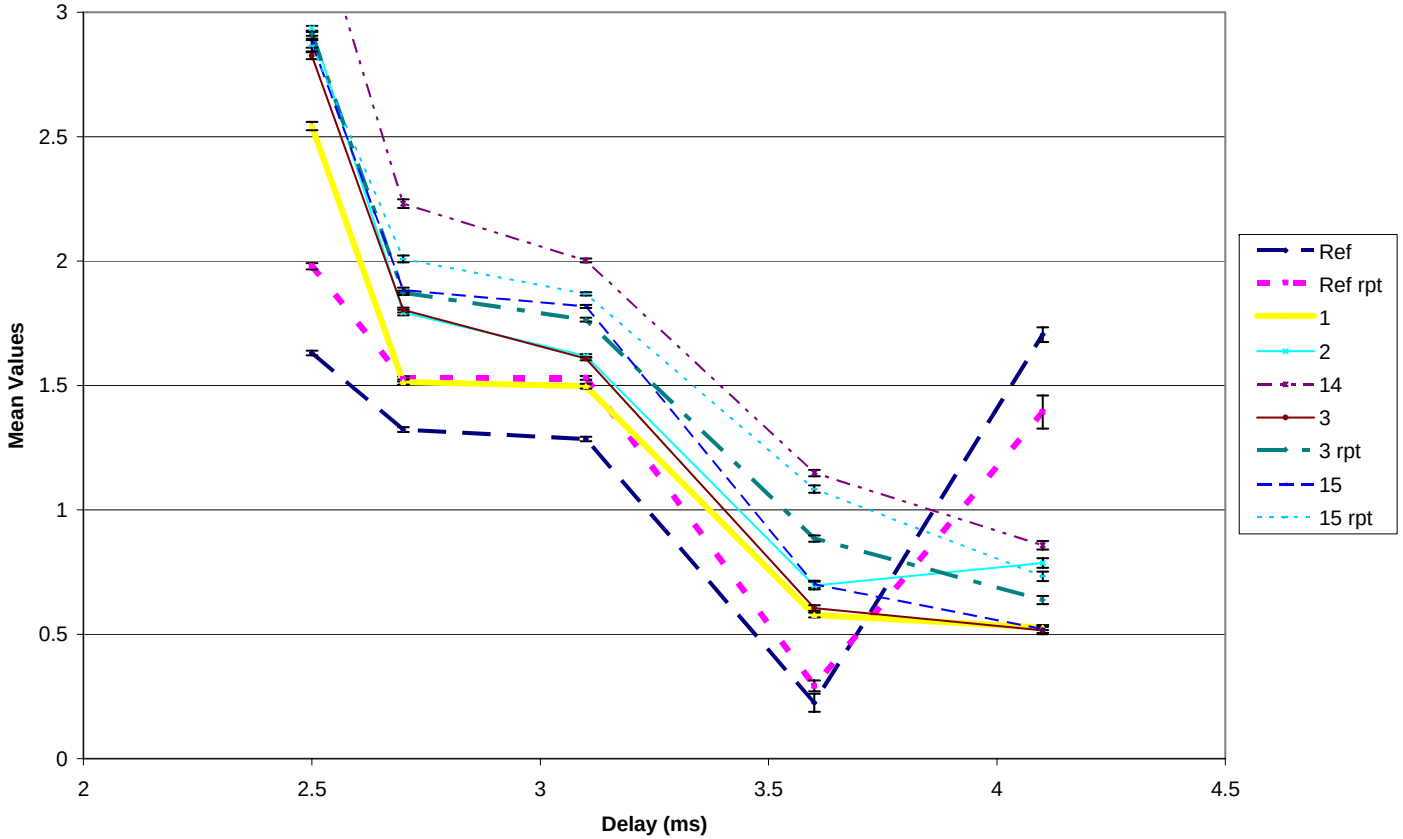

Figure 17. APF data using 10 rings and BT of 1500. Separation between the good injectors (REF & REF rpt) and bad injector (#1) only occurred at 4.1 ms. However, at this point the bad injector was better than the good ones. (Low APF)